Master of Science Thesis

Experimental Analysis of Near and Transitional Wind Turbine Wake Using Stereo Particle Image Velocimetry

C.Krishnaswami

September 30, 2013

Faculty of Aerospace Engineering · Delft University of Technology

Experimental Analysis of Near and Transitional Wind Turbine Wake Using Stereo Particle Image Velocimetry

Master of Science Thesis

For obtaining the degree of Master of Science in Aerospace Engineering at Delft University of Technology

C.Krishnaswami

September 30, 2013

Faculty of Aerospace Engineering · Delft University of Technology

Delft University Of Technology
Department Of
Wind Energy

The undersigned hereby certify that they have read and recommend to the Faculty of Aerospace Engineering for acceptance a thesis entitled **"Experimental Analysis of Near and Transitional Wind Turbine Wake Using Stereo Particle Image Velocimetry"** by **C.Krishnaswami** in partial fulfillment of the requirements for the degree of **Master of Science**.

Dated: September 30, 2013

Head of department:

Prof. dr. G.J.W. van Bussel

Supervisor:

Dr.ir. C.J. Simão Ferreira

Reader:

Dr. ir. Daniele Ragni

Reader:

Dr.ir. Gerrit E. Elsinga

Reader:

Dr. Marios Kotsonis

Reader:

ir. Lorenzo Lignarolo

Abstract

For a wind turbine, the flow downstream of the turbines (wake) is influenced by the power extraction process. This causes a momentum deficit behind the rotor, resulting in lower velocities in the wake than the free-stream velocity. Wind turbines in a wind farm are likely to operate in the wakes of upstream turbines. This drops the power production of these wind turbines. Better control strategies could help in reducing these wake losses. The first step towards achieving this goal is understanding the physics of wake re-energization.

The wake of an horizontal axis wind turbine (HAWT) is investigated using Stereo Particle Image Velocimetry (SPIV) in the open jet wind tunnel facility (OJF). The wind turbine used in the experiment is a 2-bladed wind turbine having the profile of Eppler E387 airfoil, with a design tip speed ratio of 6. Using SPIV, a three component velocity field is obtained for two different tip speed ratios (TSR). The wake is captured upto 5 diameters downstream with a focus on the shear layer. Both phase-locked and uncorrelated sampled data are obtained during the experiment.

The results from the experiment show that the tip vortices interact and leapfrogging phenomenon occurs. After the leapfrogging the tip vortices breakdown rapidly. The downstream location at which the leapfrogging takes place is dependent on the tip speed ratio. The distribution of the stream-wise axial velocity increases immediately after the point of maximum leapfrogging, implying the point of wake re-energization. The reason for tip vortex leapfrogging may be attributed to the difference in the manufacturing of the two blades. A 6% difference in the circulation is observed between the tip vortices released by the two blades. The circulation calculated along the span of the blades shows a good match with the data obtained from blade element method simulations. Preliminary results showing the loads on two different blade sections are also calculated.

Acknowledgements

I would like to express my sincere gratitude to my supervisor Dr. Carlos Ferreira who constantly encouraged and supported me throughout the project. Special thanks my daily supervisors Lorenzo Lignarolo and Dr. Daniele Ragni who guided me and always took time to answer my questions and doubts patiently.

Thanks to my office mates Mark Schelbergen, Lento Manickathan, Rob Mulders and Chenguang He (Oliver) for all their inputs and also the lighter moments which we has shared during the past year. I would also like to thank my friends Yasser Meddiakar, Venkatesh Seshan, Muralidhar Reddy, Sathis Kumar for their constant motivation. I would like to specially thank my cousin Venkat Iyer, for all his support and encouragement he gave me over the years. I would also take this opportunity to thank my brother Adithya for all his support, encouragement and motivation.

Finally, I would like to record my heartfelt gratitude my parents, grandparents, all my teachers and family members for all their blessings, and unconditional support I have received from them over the years, without which this would not have been possible.

Delft, The Netherlands C.Krishnaswami
September 30, 2013

Contents

List of Figures

List of Tables

Nomenclature

Latin Symbols

c	Blade chord	[m]
C_L	Coefficient of lift	[-]
C_p	Coefficient of power	[-]
C_T	Coefficient of thrust	[-]
f	Frequency of blade rotation	[Hz]
p_∞	Static pressure	[Pa]
p_{dyn}	Dynamic pressure	[Pa]
p_{tot}	Total pressure	Pa]
R	Specific gas constant	[J/(kg.K)]
r	Blade radius	[m]
T	Temperature	[K]
t	Vortex age	[s]
U_∞	Free-stream velocity	[m/s]
u,v,w	Velocity vectors in x,y and z directions respectively	[m/s]

Greek Symbols

α	Angle of attack	[degrees]
Γ	Circulation	$[m^2/s]$
Λ	Tip Speed Ratio	[-]
ν	Kinematic viscosity	$[m^2/s]$

Ω	Angular velocity	[rad/s]
ω	Vorticity vector	[1/s]
ρ	Density	[kg/m^3]

Abbreviations

AoA	Angle of Attack
BEM	Blade Element Method
CFD	Computational Fluid Dynamics
FOV	Field of View
HAWT	Horizontal Axis Wind Turbine
OJF	Open Jet Facility
PIV	Particle Image Velocimetry
SPIV	Stereo Particle Image Velocimetry
TI	Turbulence Intensity
TSR	Tip Speed Ratio

Chapter 1

Introduction

Wind energy is one of the cleanest forms of energy and doesn't contribute to green house emissions, which causes global warming. It is also one of the least expensive forms of renewable energy, making it an attractive option [20]. Wind turbines are used to convert the wind energy into other useful forms of energy. Groups of these wind turbines are called wind farms.

For a wind turbine, the flow downstream of the turbines (wake) is influenced by the power extraction process. This causes a momentum deficit behind the rotor, resulting in lower velocities in the wake than the free-stream velocity. In case of wind farms other wind turbines present in this part of the flow (with lower velocities) are affected. It is known that the power output for a wind turbine is proportional to the cube of the inlet velocity. Therefore, a drop in power output from these downstream wind turbines can be observed. Hence it is important to devise better control strategies, which help in reducing these losses. The first step towards achieving this goal is to understand the physics of wake re-energization. The wake loss phenomenon in a wind farm is illustrated in the figure 1.1.

1.1 Project overview

The wake of a horizontal axis wind turbine (HAWT) is a complex three-dimensional turbulent flow. Its physics has been studied in depth with experiments, field measurements and modelled with numerical analysis [46]. Large inaccuracy in the prediction of loads and energy yields of a wind turbine in a wind farms are encountered in the current numerical codes. This is largely due to the poor modelling of the wake [7] , still based on the actuator disc assumption, which does not allow for a correct prediction of the kinetic energy transport and turbulence creation in the flow of a turbine's wake, as shown by Schepers [40]. These factors are of paramount importance, because turbulent mixing governs the re-energising process of the wake, which in turn plays a major role in determining the wake losses.

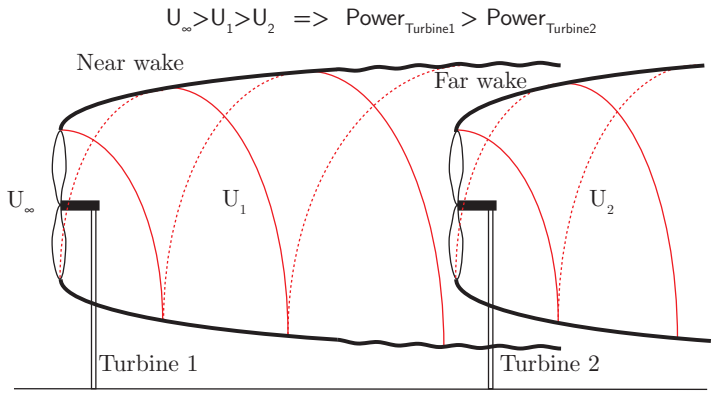

Figure 1.1: Wake loss in a wind farm

Two different types of models are used for predicting power losses due to wind turbine wakes [6]. The first type are wind farm models which use a wake model, that has been simplified in order to predict the power losses in a short span of time. The results obtained are of average quality with an under prediction of the wake losses [4]. The second type are CFD models which solves basic flow equations to produce results, these are computationally expensive with an over prediction of the wake losses [4]. Hence there is a gap between the reality in wind farms and the models. Therefore a better understanding of modelling power losses is required in order to have better wind farm and wind turbine design and control strategies.

Spacing of wind turbines in a wind farm plays a crucial role in determining power losses. By intuition the larger the spacing, the lower is the loss due to wakes because the wakes tend to recover downstream by drawing momentum from the surrounding free stream flow. But literature review [6] [14][44] shows that spacing alone is not a criteria for reducing the wake losses, but a fundamental understanding of wake breakdown is required. Quantifying the impact of spacing on wake losses are hindered by several barriers like lack of data availability and complexity of wake interactions[5].

Lower turbulence levels in offshore wind farms due to lower boundary layer roughness causes the wake effects to propagate over larger distances downstream than in case of an onshore wind farm. Therefore it is important to understand the role of not only the atmospheric turbulence but also the turbulence generated in the wake of a wind turbine.

This project attempts to address these requirements by collecting data, which can not only be used for a better understanding of wind farm aerodynamics but also used for improving and validating CFD models.

1.1.1 Aim of the investigation

Literature study performed on experiments on a wind turbine's wake shows only a small number of experiments focussing on wake re-energization and mixing in the wake. Moreover, nearly all of these experiments consider wake mixing along with atmospheric turbulence mixing. The first step of this investigation relates to separation of these two mixing

processes and study wake mixing alone. An experimental approach was adopted for this process using PIV, which is a high resolution technique capable of capturing the detailed behaviour of turbulence in the wake even upto the smaller scales.

The aim of this project is as such to study the re-energising process only due to the self-induced flow in a low turbulence wind tunnel, namely to analyse how the turbulence generated by the turbine itself and by the breakdown and instability of the wake vortex structure promote mixing. This is proposed to be studied by an experiment on a 60 cm diameter wind turbine using stereo particle image velocimetry (SPIV) on its wake is to be performed in the open jet wind tunnel (OJF) at Delft University of Technology.

The presence of periodic structures in the flow caused by the rotation of the blade, the transfer of kinetic energy from the mean flow field to the inner part of the wake is studied via a triple decomposition of the flow with mean, periodic and turbulent velocity contributions [38]. In order to obtain the terms for triple decomposition, two different types of data are obtained during the experiment namely, phase locked data and unconditionally sampled data. Phase-locked sampling of the data consists of capturing PIV data only at a specific azimuthal position of the blade. The unconditional sampling relates to random capturing of data with respect to the azimuthal position of the blade for an ensemble. This is done in order to analyse the mixing process by separating the contribution of the random fluctuations and the periodic fluctuations to mixing. The data obtained not only consists of three component velocities but also the Reynolds stresses.

The results obtained from the experiments seek to have a better understanding of the physics, specifically wake re-energization and mixing.

1.2 Outline

Chapter 2 covers a basic overview of concepts related to wind turbine aerodynamics specially the wake, followed by the basics of stereo particle image velocimetry which is the experimental method used. Chapter 4 consists information regarding the wind turbine model and its blade characteristics. The 5th chapter details the experimental setup and the post processing procedure of experimental data. The results from the experiment are presented in chapter 6. The uncertainties from the experiment are explained in chapter 7 followed by the conclusion in the final chapter.

Chapter 2

Horizontal axis wind turbine aerodynamics

A wind turbine extracts energy from the wind, thereby causing the energy potential in the flow behind the turbine to drop. For the flow to recover this energy, it undergoes re-energization through mixing. In order to understand the mechanism of mixing in the wake it is imperative to understand the basics involved with the wake of a horizontal axis wind turbine and the various methods used to model the wake along with it shortcomings. Figure 2.1 shows the schematic of the wind turbine wake and the mixing which mainly happens at two different levels.

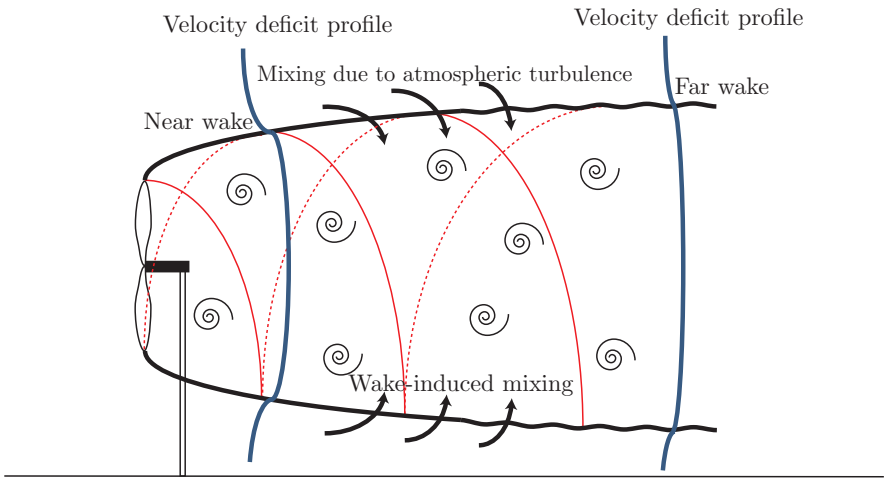

Figure 2.1: Schematic of wind turbine wake

Wake of a wind turbine can be split into two regions namely near wake and far wake [46]. The following sections cover the various near and far wake models followed by the general characteristics of the wake.

2.1 Near Wake Models

The near wake is the region right behind the wind turbine. Though there is no exact demarcation for both near and far wake, it is empirically taken as up to 1-2 rotor diameters [46]. This region is characterized by tip vortices, separation from nacelle, 3-D effects, blade aerodynamics, etc,. [39]. This region is dependent on the design of the rotor i.e., blade loading and turbine performance. Another definition given by Crespo et al. [13] considers the near wake to the distance downstream up to which the shear layer thickness reaches the wake axis.

2.1.1 Actuator Disc Theory

The actuator disc theory is a theoretical model which is used in modelling the near wake behind a rotor. This is done by defining the actuator as a surface, normal to the flow direction, on which uniform distribution of blade forces acts upon the incoming flow [43].

From figure 2.2 it can be seen that the presence of an actuator disc causes the air approaching the turbine to gradually slow down behind it. At the same time as it passes through the rotor disc, a drop in static pressure behind the turbine can be observed. This region of air behind the turbine which has a lower velocity and lower static pressure is the wake of the actuator.

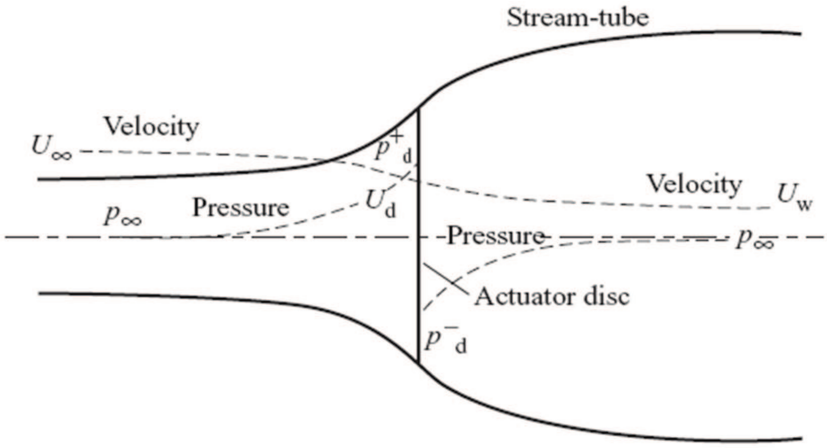

Figure 2.2: Stream tube of an actuator disk [10]

The actuator disc applies a force field on the flow [21]. This induces a velocity variation which is superimposed on the free-stream velocity. This can be related to the velocity of air at the plane of actuator disc as shown in equation 2.1. Where a is the axial induction factor.

$$U_d = U_\infty(1 - a) \tag{2.1}$$

Also by applying a force balance across the actuator, relationship between the various

velocities can be obtained as shown in equation 2.2.

$$U_w = U_\infty(1 - 2a) \tag{2.2}$$

From the equation 2.2 we can see that as the induction factor starts to increase from 0, the wind speed behind the rotor also starts to decrease. If the value of the induction factor is more than 0.5 the velocity behind the rotor becomes zero or even lesser, which is not physically possible. In these conditions the momentum theory described is no longer valid and an empirical modifications have to be made [10]. Equation 2.3 can be obtained by combining 2.1 and 2.2.

$$U_d = \frac{U_w + U_\infty}{2} \tag{2.3}$$

Combining equation 2.2 and 2.1, equation 2.3 is obtained, which shows that the velocity at the rotor plane is equal to the average of the upstream or free stream velocity and the velocity in the wake downstream.

2.1.2 Blade Element Theory

This theory is used to model the lift and drag forces on wind turbine rotors. These forces are responsible for the rate of change of axial and angular momentum of all the air which passes through the area swept by the blade [10].

According to this theory the blade is divided into several smaller elements and the forces on each of these blade elements can be calculated by means of two-dimensional airfoil characteristics i.e., using the data of C_l and C_d variation with angle of attack, the forces on the blade can be calculated for given values of induction factor.

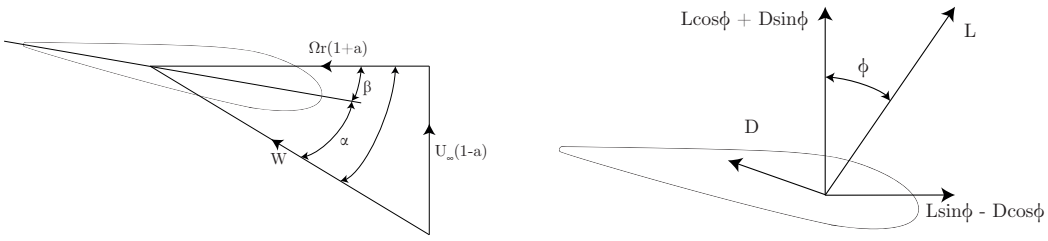

(a) Velocities on a blade element

(b) Forces on a blade element

Figure 2.3: Velocities and forces on a blade element

From figure 2.3(a) the resultant relative velocity at the blade is given by

$$W = \sqrt{U_\infty^2(1-a)^2 + \Omega^2 r^2(1+a')^2} \tag{2.4}$$

The lift force on a blade element of unit span wise length, having a chord c, perpendicular to the direction of W is given by

$$\delta L = \frac{1}{2}\rho W^2 c C_L \tag{2.5}$$

Similarly the drag force parallel to W for unit span wise length is given by

$$\delta D = \frac{1}{2}\rho W^2 c C_D r \tag{2.6}$$

The model is quite simple and easy to implement. The disadvantage of this theory is that it does not incorporate higher order effects like 3-D flow, unsteady effects, yaw. Though corrections like Prandtl tip correction, Glauert's correction can be applied in rectify these shortcomings [10].

2.2 Far wake models

The region beyond the near wake where the aerodynamic properties of the rotor like, tip vortices and root vortex are not visible is considered as the far wake[46]. This is the region of prime importance in case of design of wind farms. In the far wake the two main mechanisms determining the flow conditions are convection and turbulent diffusion [26].

Far wake models can be divided into kinematic wake models and field models. Kinematic models are based on self-similar velocity deficit profiles obtained from experimental and theoretical work on co-flowing jets while the field models are CFD models which work on the principle of calculating the flow magnitude at every point of the flow field [46].

2.2.1 Jensen model

This is the simplest of all the kinematic models which assumes a linearly expanding wake, with a velocity deficit in the wake that is directly proportional only to the distance downstream of the rotor [7]. Though in reality the velocity profile varies radially across the wake at a downstream position. The relationships for the wake diameter and velocity in the wake are given by the equations 2.7 and 2.8 respectively.

$$D_w = D(1 + 2ks) \tag{2.7}$$

$$U_w = U_\infty \left[1 - \frac{1 - \sqrt{1 - C_T}}{(1 + 2ks)^2}\right] \tag{2.8}$$

Here k is the wake decay constant and s is downstream distance in terms of rotor diameters.

2.2.2 Larsen model

Larsen model is based on the Prandtl turbulent boundary layer equation. It has a closed-form solution for the width of the wake and the mean velocity profile in both axial and radial directions. The wind shear is neglected and it is also assumed that the flow is incompressible and stationary. Larsen obtained solutions for the first-order and second-order wake models [28]. The second order approximate solution of the rotor wake radius of the wake is given by the equation 2.9.

$$R_w(x) = \left(\frac{35}{2\pi}\right)^{\frac{1}{5}} (3c_1^2)^{\frac{1}{5}} (C_T A(x + x_0))^{\frac{1}{3}} \tag{2.9}$$

In the above equation x is the axial distance. A is the rotor area and C_T is the thrust coefficient. c_1 is a constant which is related to the Prandtl mixing length and the applied co-ordinate system x_0.

The velocity profile obtained in the wake is not only dependent on the downstream distance like the Jensen model but also on the turbulent intensity in the wake.

2.2.3 Frandsen model

This is a model was developed specifically for wind farm calculations. This model assumes a hat-shaped wind speed profile in the wake similar to the Jensen model, but the interaction between the wakes are modelled in a detailed manner. The model assumes the wake to start expanding abruptly just after the rotor. The wake diameter at any downstream position is given by the equation 2.10

$$D_w(x) = D(\beta^{\frac{k}{2}} + \alpha s)^{\frac{1}{k}} \tag{2.10}$$

where s=x/D, D being the rotor diameter. k being the expansion ratio and α being the wake decay constant.

The wake expansion parameter β is given by equation 2.11

$$\beta = \frac{1 + \sqrt{1 - C_T}}{2\sqrt{1 - C_T}} = \left(\frac{D_{eff}}{D}\right)^2 \tag{2.11}$$

Three different wake regimes are recognized by the models, the first being wake flow without interaction between neighbouring wakes while the second considers this interaction. The final regime considers the expansion of the wake in vertical direction alone [37].

2.2.4 Field models

Field models calculate the complete flow field in a wind farm by solving the Reynolds Averaged Navier Stokes equations (RANS) with a turbulence model for closure [27]. Solving these equations for wind farms are computationally expensive, hence several numerical techniques are applied in order to reduce the computation time.

2.3 Wind turbine wake

A HAWT is comparable to rotating wing. Hence a vortex system similar to a linearly translating wing exists in this system as well. The vortex sheet for the HAWT is directed in a helical path downstream behind the rotor. Figure 2.4 shows a typical helical wake.

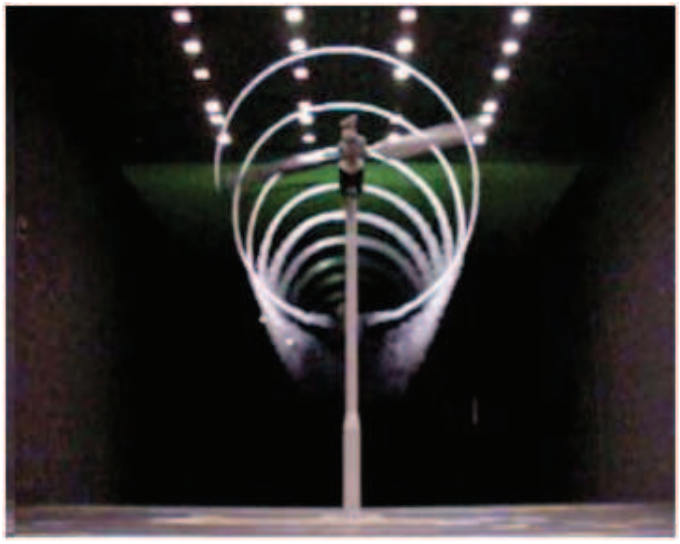

Figure 2.4: Wake visualization for a wind turbine [42]

The wake travels in a helical path with a rotation in the opposite direction to that of the rotation of the wind turbine. The air which passes through the rotor plane exerts a torque on the wind turbine blade. Hence a reaction torque is exerted in the opposite direction of rotation which causes the wake to rotate in an opposite direction to that of the wind turbine blade. This wake expands uniformly in all direction downstream.

2.3.1 Tip and Root vortex

The point where the blade ends, a strong vortex is generated owing to the high gradients in circulation (proof shown in 2.3.3). Practically, it is not possible to extend the blade up to the axis of rotation. Hence an abrupt jump in circulation can be observed at this point leading to generation of root vortex. The root vortex is mainly responsible for inducing a tangential velocity in the wake [10]. Similarly, a tip vortex is created at the other extreme (tip) of the blade [46].

2.3.2 Vortex flow

For understanding the wake physics it is necessary to study the vortex flow. Any region within a fluid where the flow is spins about an imaginary axis. which may be straight or curved is known as a vortex. Vortex flow can be classified into two limiting cases namely rotational and irrotational flow.

Rotational flow

Consider a series of concentric circular streamlines, for a rotational flow the fluid elements that move along the streamline deform and also rotate. Rotational flow has a tangential velocity that increases along with an increase in the radius of the streamline [3]. This relation for tangential velocity is given by the equation 2.12, where r is the distance from the centre and ω is the angular velocity.

$$V_\theta = \omega r \tag{2.12}$$

Irrotational flow

In an irrotational flow the the fluid elements move and deform along a streamline but does not rotate. An irrotational flow satisfies the condition as shown in equation 2.13. The vortex released from the blade of the wind turbine is considered as irrotational except at the centre [46]. The total mechanical energy of the fluid elements remains same in the entire flow field and the tangential velocity is inversely proportional to the radius of curvature [3]. Consider the streamlines for an irrotational vortex flow as shown in figure 2.5.

$$\frac{\partial v}{\partial x} - \frac{\partial u}{\partial y} = 0 \tag{2.13}$$

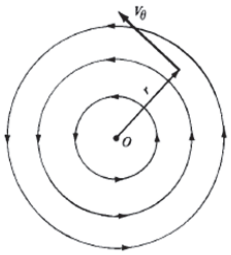

Figure 2.5: Vortex flow [3]

The conditions a flow must have in order to considered as a vortex flow are shown in equations 2.14 and 2.15.

$$V_r = 0 \tag{2.14}$$

$$V_\theta = \frac{C}{r} \tag{2.15}$$

In the above equations V_r is the radial velocity, V_θ is the tangential velocity and C is a constant.

Consider a closed integral C along a flow field moving with a velocity V as shown in figure 2.6. The circulation (Γ) for this flow field is defined by the following equation.

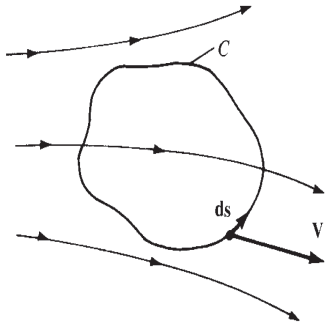

Figure 2.6: Closed integral in a flow field [3]

$$\Gamma = \oint (V).dS \tag{2.16}$$

Using the Stokes theorem the equation can also be written as shown in equation

$$\Gamma = \int \int (\nabla \times V).dA \tag{2.17}$$

Consider figure 2.5, the circulation around a circular streamline at a radius r can be calculated using the above equation 2.16 as

$$\Gamma = - \oint (V).dS = - V_\theta.(2\pi r) \tag{2.18}$$

$$-V_\theta = \frac{\Gamma}{2\pi r} \tag{2.19}$$

Comparing equation 2.19 with equation 2.15 for tangential velocity we see that for a vortex flow $\frac{\Gamma}{2\pi}$ is constant.

The constant shows that the circulation taken about all streamlines is the same. The strength of a vortex is defined in terms of vorticity. This is mathematically defined as the curl of the velocity field [3]. This is a vector field which gives a microscopic view of the rotation of the fluid at any point.

$$\omega = \nabla \times V \tag{2.20}$$

Vorticity can be related to the circulation using equation 6.9 and 2.17 as.

$$\Gamma = \int \int \omega.dA \tag{2.21}$$

2.3.3 Tip/Root vortex generation in a wind turbine

Assuming a uniformly loaded (force distribution) two-dimensional actuator disk for this analysis. Consider the momentum equation apply curl on both sides for the equation [19].

$$\rho(V.\nabla)V = -\nabla p + f \tag{2.22}$$

$$\rho(\nabla \times (V.\nabla)V) = \nabla \times (-\nabla p + f) \tag{2.23}$$

Consider the left hand side of the above equation

$$\nabla \times (V.\nabla)V = V(\nabla \times (V.\nabla)) + (V.\nabla)(\nabla \times V) \tag{2.24}$$

$$\nabla \times (V.\nabla)V = V(\nabla\omega) + (V.\nabla)\omega \tag{2.25}$$

The pressure term on the right hand side becomes $\nabla \times \nabla p = 0$. Since the curl of a gradient is zero. Here we use the relation from equation 2.20, where ω is the vorticity. The equation becomes

$$\rho(V(\nabla.\omega) + (V.\nabla)\omega) = \nabla \times f \tag{2.26}$$

The right hand side of the equation becomes

$$\nabla \times f = \begin{vmatrix} \hat{i} & \hat{j} & \hat{k} \\ \frac{\partial}{dx} & \frac{\partial}{\partial y} & \frac{\partial}{\partial z} \\ f_x & f_y & f_z \end{vmatrix} = \hat{i}\left(\frac{\partial f_x}{dy} - \frac{\partial f_y}{dz}\right) - \hat{i}\left(\frac{\partial f_z}{dx} - \frac{\partial f_x}{dz}\right) + \hat{k}\left(\frac{\partial f_y}{dx} - \frac{\partial f_x}{dy}\right) \tag{2.27}$$

From the assumption of a 2-D actuator disk, most of the terms drop out and the final equation obtained is

$$\rho(V(\nabla\omega) + (V.\nabla)\omega) = \left(\frac{\partial f_x}{\partial z}\widehat{j} - \frac{\partial f_x}{\partial y}\widehat{k}\right) \tag{2.28}$$

At the edge of the actuator disk $\frac{\partial f_x}{\partial y} \neq 0$. Hence there is a generation of vorticity only at the tips for a uniform loading case. The first term on the left hand side of the equation 2.28 quantifies the vortex convection while the other term signifies the stretching and the turning of the vortex [12]. In case of a non-uniform loading of the actuator disk vortices are generated all along the span of the blade, while for a uniformly loaded blade (constant circulation along the span) only the tip and root vortices are generated.

2.4 Tip vortex path and breakdown

In the near wake region the wake expands and for this reason the tip vortex is also pushed outboard in the radial direction. The diameter of these vortices also tend to increase as it moves downstream owing to viscous effects.

The tip vortex core over a period of time has a slow side to side movement which may be self induced or because of the free stream. The amplitude of the fluctuations of the vortex cores increases downstream as seen from the spread of points downstream from the experiment performed by Dobrev et al. [15], this is shown in figure 2.7 . This is called as vortex wandering.

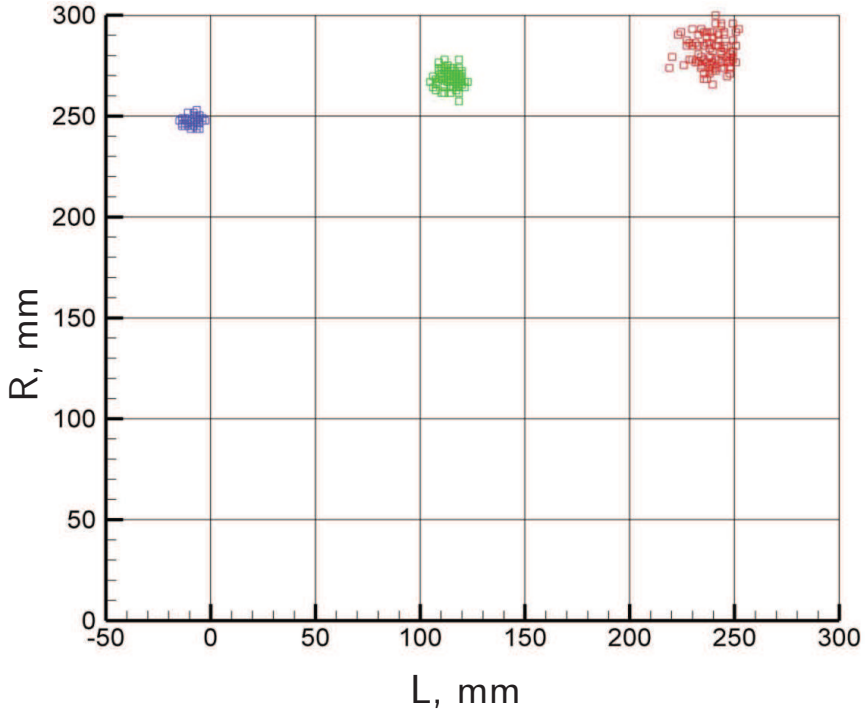

Figure 2.7: Vortex core wandering as a function of time [15]

Few other properties of tip vortices as pointed out by Ebert et al. [16] show that tip vortices have increasing amounts of angular momentum as the tip speed ratio increases. Also the tip vortices tend to show a decreased pitch as tip speed ratio increases.

A vortex breakdown or bursting refers to the phenomena in which the high tangential velocity, small vortex core radius flow transforms into a turbulent, low tangential velocity, large vortex core radius flow [27]. The strength of a vortex can be usually related with the diameter of these vortices. The diameter of the core of the tip vortices decreases due to vortex stretching near the blade; this is followed by an increase in the core diameter due to viscous effects [15]. This finally leads to a vortex breakdown.

2.5 Wake mixing and stability

Theoretically, if the velocity deficit distribution for a downstream position is drawn, a Gaussian profile is obtained in the wake. This velocity deficit profile is axisymmetric about the centre of the wake. Figure 2.8 shows a schematic of the velocity deficit profiles at different points in the downstream. It can be clearly seen that there is a recovery in the velocities in the far wake, where the Gaussian profile of the velocity deficit in the wake tends to become a straight line. This is due to turbulent mixing which causes a velocity recovery in the wake. At some point in the far wake the velocity inside the wake is equal to the free stream velocity. Though in reality, the velocity deficit in a wake does not follow a Gaussian profile, due to the proximity of ground where the velocity gradients are higher.

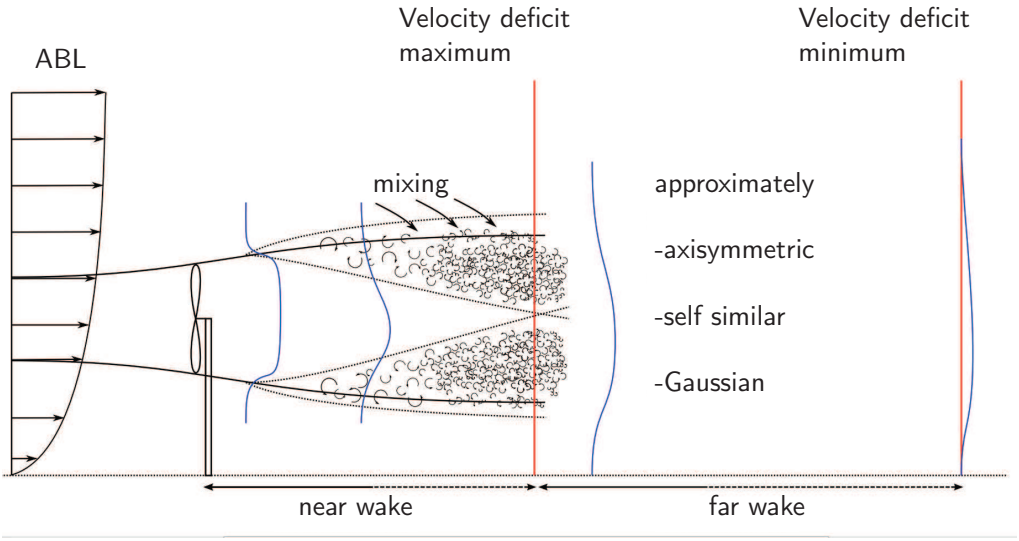

Figure 2.8: Velocity deficit profiles inside the wake of a wind turbine [39]

Wake mixing happens at two different levels: at the atmospheric turbulent flow level and at the wake-induced level. The latter of particular interest because it concerns the mixing process owing to the presence of the tip vortex helix, its instability and its breakdown, namely parameters which are directly depending on the turbine design and its operation. In the far wake, the pressure gradients play a less important role and the velocity recovery strongly depends upon the turbulence levels in the wake [39]. Hence in case of wind farms this aspect becomes quite important. Turbulence levels in the wake becomes even more important for off-shore wind farms; where the role of atmospheric turbulence is much lower than on-shore. This can be attributed to the surface roughness in an off-shore condition, which is lower resulting in lower turbulence intensity.

Turbulent mixing governs the re-energising process of the wake. The turbulence in the wake mixes the low velocity wake along with the higher velocity free stream. The main factors that affect the turbulence in the wake are parameters like turbulence levels in atmosphere, boundary layer roughness, wind shear effects, turbine structural effects, tip vortices and turbulent boundary layer. If the turbulence levels are low, the velocity recovery in the wake takes longer distances. Hence the recovery of wakes in case of off-

shore wind farms takes longer than that of the on-shore wind-farms [39]. At the same time, it is also noticeable that the velocity deficit decay is much faster than compared to turbulence intensity. For instance data from the Norrekaer windfarm, suggests that turbulence intensity in the wake can be seen up to 14.5 diameters downstream leading to higher loading on downstream wind turbine [24].

The transport of kinetic energy in the wake of a wind turbine takes place at all azimuthal positions for an individual wind turbine. In case of a large wind farm the case becomes slightly different. The analysis by Hamilton et al. [22] [11] shows the importance of vertical transport of kinetic energy to replenish the wakes and to enable the power extraction in the array. This is because of the wake interaction between the wakes of other wind turbines.

Tip vortex pairing also has a strong influence in turbulent mixing and growth of shear layer. Tip vortex pairing is the phenomena in which the tip vortices generated by the blades of the wind turbine interact with subsequent vortices, to form one vortex structure rotating about the other vortex and ultimately forming a single vortex over a period of time. This can be seen from figure 2.9. The sequence from left to right shows the vortices as it moves downstream, with two different velocities of U_1 and U_2 below and above it respectively.

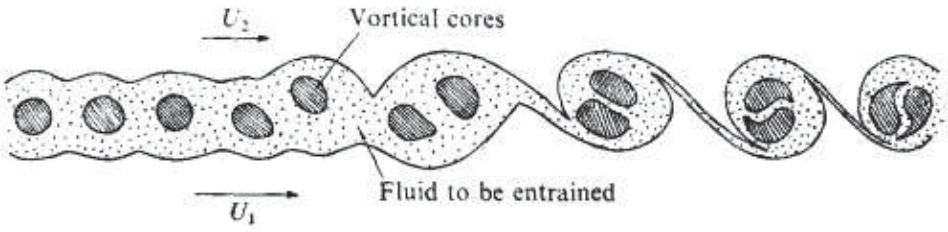

Figure 2.9: Vortex pairing [49]

Winant et al. [49] demonstrated using two streams of water moving at different velocities, that most of the entrainment in mixing layers takes place because of successive merging of the vortices. These merged vortices has approximately twice the spacing distance as that of the un-merged vortices. It was also found out by Browand et al. [9] that the vortex pairing promotes transport of transverse momentum and the mixing rate.

As seen above tip vortex pairing, which relates to the wake instability has quite a strong effect on turbulent mixing. Hence the understanding of the mechanisms of wake instability behind rotor systems becomes important. Experiments performed by Felli et al. [18] studies the mechanism of evolution of propeller tip and hub vortices in the transitional region and the far field. The results show the dependence of the wake instability transition on the inter-spiral distance and specically the streamwise displacement of the transition region (where the vortices start interacting) at the increasing inter-spiral distance. The transition region starts moving downstream when the spiral to spiral distance reduces. This spiral to spiral distance in turn depends on the blade number, loading conditions and tip speed ratio.

The numerical study by Ivanell et al. [25] tries to obtain a better understanding of stability properties of wakes generated by wind turbine rotors. The numerical model is

based on large eddy simulation of N-S equations using actuator line method to generate the wake and tip vortices. In order to determine the critical frequencies, the flow is disturbed by introducing harmonic perturbations. The results from the simulations show that instability usually disperses except for certain frequencies which grows over a period of time. Two types of modes are observed, one where oscillations of neighbouring vortices are in phase and out of phase of each other. The mode in which the spirals are out of phase of each other causes vortex pairing to occur. The study in the paper also shows a relationship between turbulence intensity and length of stable wake.

Chapter 3

Experimental Technique:Particle Image Velocimetry

3.1 Principle of particle image velocimetry

Particle Image Velocimetry (PIV) is a measurement technique which measures the displacements of small tracer particles, which move along with the flow. The measurements of the displacement are carried out by taking two sequential snapshot of the tracers separated by a known time delay.done continuously with a known time delay between each measurement. From the displacement of the particles in the separation time the velocity component can be obtained. The recording of these displacements require an illumination and a digital imaging device which is capable of capturing several different instants of flow [33].

3.1.1 Components of PIV system

Seeding

The main requirement for a seeding particle is that it must not affect the flow properties. A usual seeding concentration from 10^9 to 10^{12} particles/m^3 is demonstrated to have no affect on the flow. The main parameter that governs the ability to capture the flow is the ratio of mass of the fluid to the mass of the particles [17].

Another important property which is required for a seeding particle is its ability to scatter enough light for the cameras to detect the particles. This is dependent on the particle diameter and the refractivity index of the particle relative to the fluid medium.

Illumination

A light source is required for PIV in order to illuminate the plane of measurement at two instants separated by a short time. The light scattered by the particles gets captured by

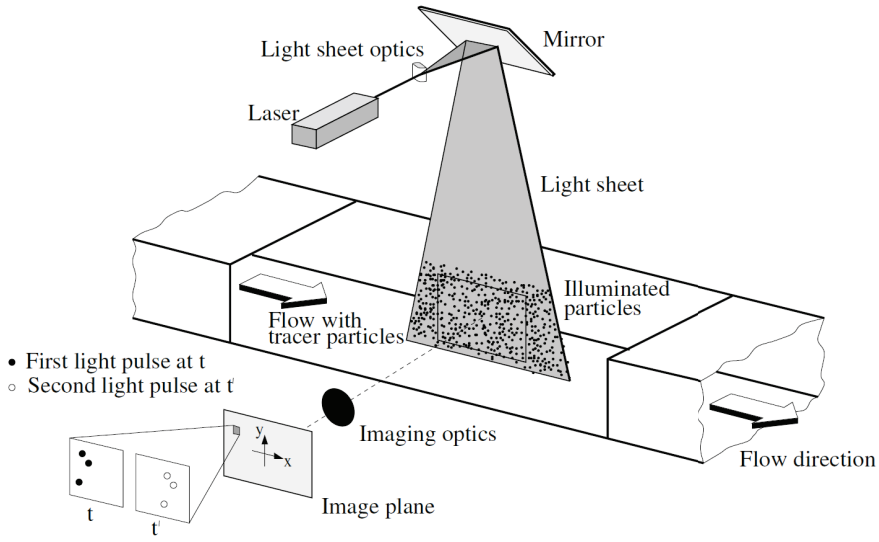

Figure 3.1: Schematic of a particle image velocimetry system [33]

the imaging device. It is also important to control the thickness of the laser sheet. This is done by using optics.

Lasers are a suitable choice as an illumination source since they satisfy all the requirements. It can be easily shaped into a thin light sheet by using different optical arrangements.

Imaging

The imaging system is usually defined by its focal length, f-stop or aperture number and image magnification. The magnification is dependent on the distances between the image and the object to the lens, which in this case is the field of view (FOV). In practice, this is done by using a camera attached to lenses, which help in changing the focal length at which the image is captured.

3.1.2 Image processing

In order to evaluate the recordings of PIV, the recorded image is divided into smaller interrogation windows. Cross correlation analysis is performed on these interrogation windows. Cross-correlation analysis is a measure of similarity in two different measurements. Using this analysis on the two instants a cross-correlation peak is obtained. The final velocity field is obtained by using the average displacement and separation time between the images (dt) using the formula shown in equation 3.1. This procedure is shown in figure 3.2

$$V = \frac{Avg.displacement}{dt} \tag{3.1}$$

If the interrogation window size is too small then it may give out lots of spurious and unphysical velocity vectors in the field. If this window is too big, it may be unable to capture the flow details due to low spatial resolution thus yielding poor results.

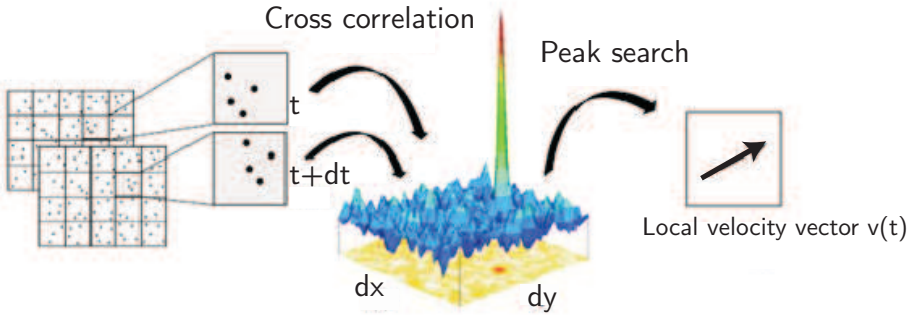

Figure 3.2: PIV image processing using cross correlation [29]

Overlap

Consider a particle near the edge of the interrogation window as shown in the red circles in figure 3.3. These particles from two consecutive frames are at different interrogation windows. In order to overcome this problem, overlapping of neighbouring windows are used. This can be seen from figure 3.3 where the particles which are lost near the edge are recaptured using overlap. A 50% overlap is commonly used in practice, in order to improve spatial resolution [48] [23].

Multipass

The multi-pass window deformation technique consists of multiple passes with decreasing window sizes. These windows are shifted by a distance of the average particle displacement during the subsequent passes. By doing this the particles are tracked effectively even for large displacements [33].

Median Filter

Median filter is a method useful in removing certain types of impulse noise in which individual pixels have extreme values. Consider the figure 3.4, it can been seen that the pixel at the centre has a value which is much higher than the surrounding pixels. Here the pixels with the grey background are taken into consideration. The values are written in an ascending order and the median (middle value) of these numbers is taken as a replacement value. This method is more robust since the final result doesn't depend upon the extreme values unlike using mean [33].

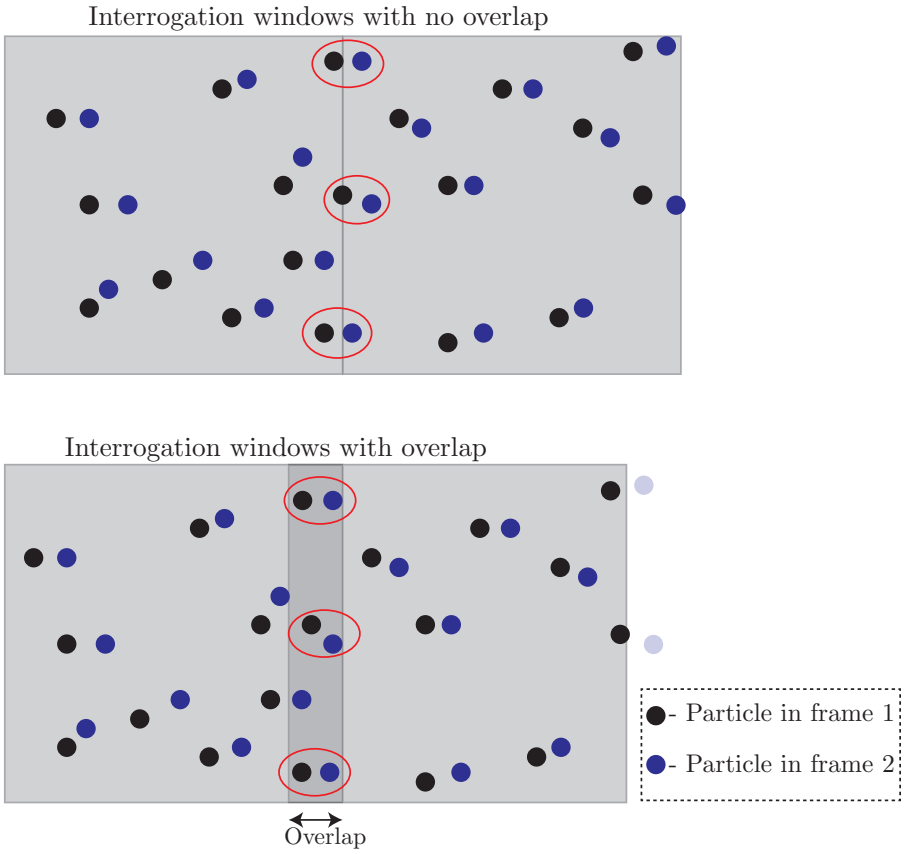

Figure 3.3: Overlap of interrogation windows

100	102	103	105	108
104	101	104	103	106
105	100	**200**	101	103
103	110	107	102	100
106	108	105	103	101

103

Values of the surrounding pixels
100,101,101,102,103,104,107,110,200
Median value
103

Figure 3.4: Median filtering

3.2 Stereo particle image velocimetry

A modified version of PIV like stereo PIV is required in order to capture the velocities in all 3 dimensions on a plane. The working principle remains the same as that of the convential 2D PIV, however by using stereo-particle image velocimetry the third velocity component perpendicular to the plane can be obtained by using an additional camera.

The method for obtaining the third perpendicular velocity component is similar to the functioning of the human eye. Using a single eye only the direction of motion can be understood, but not the depth. The human eye perceives depth with help of two eyes, each of which have a different field of view. The brain processes these two fields of view to give a single view with a perception of depth.

3.2.1 Working principle

As mentioned above stereo particle image velocimetry uses an additional camera for capturing the field from two different angles. Consider figure 3.5, which shows a 2-D schematic for SPIV, here U and V represent the velocities in x and y-directions respectively. α and β represent the camera viewing angles with respect to yz and xz planes [33].

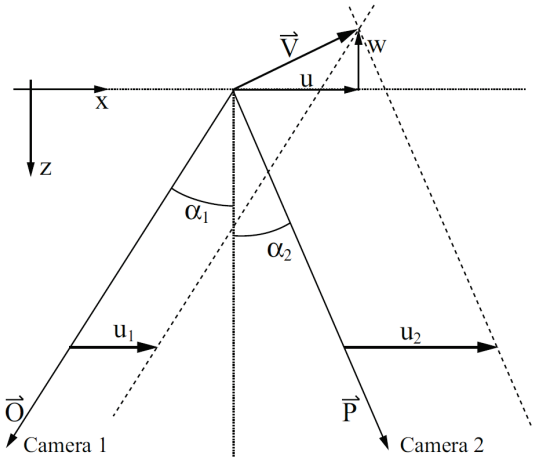

Figure 3.5: Velocity components in a stereo particle image velocimetry setup [33]

The velocities can be resolved using equations 3.2, 3.3 and 3.4. These equations are obtained using geometrical relations in the setup [33].

$$U = \frac{U_1 \tan\alpha_2 + U_2 \tan\alpha_1}{\tan\alpha_1 + \tan\alpha_2} \tag{3.2}$$

$$V = \frac{V_1 \tan\beta_2 + V_2 \tan\beta_1}{\tan\beta_1 + \tan\beta_2} \tag{3.3}$$

$$W = \frac{U_1 - U_2}{\tan\alpha_1 + \tan\alpha_2} = \frac{V_1 - V_2}{\tan\beta_1 + \tan\beta_2} \tag{3.4}$$

For avoiding singularity, which rises if α or β tends to zero equations 3.2 and 3.3 can be rewritten as

$$U = \frac{U_1 + U_2}{2} + \frac{W}{2}(\tan\alpha_1 - \tan\alpha_2) \tag{3.5}$$

$$V = \frac{V_1 + V_2}{2} + \frac{W}{2}(\tan\beta_1 - \tan\beta_2) \tag{3.6}$$

A stereo particle image velocimetry system has two basic setups namely the translation system or lateral displacement and the angular displacement or rotational system method [31]. The discussion in the following sections are limited to the systems used in the experiment.

3.2.2 Rotational system

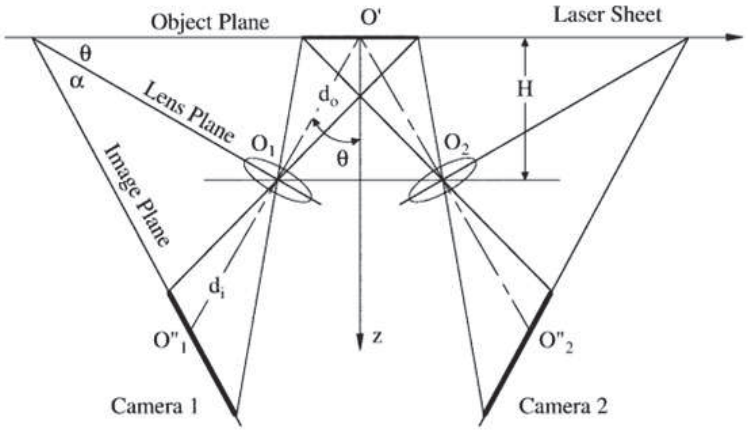

Figure 3.6: Rotational system for SPIV [31]

The rotational system as seen from figure 3.6 has two cameras which are non-parallel with their axis intersecting at the image plane. The rotated cameras form an angle θ with respect to the perpendicular from the image plane. An increase in the angle of rotation θ results in a greater accuracy in the out of the plane component. However the magnification obtained may no longer be uniform over the field of view.

Since the cameras are inclined, the object plane is no longer parallel to the lens plane, it is therefore required to rotate the image plane by a certain angle (here α, see figure 3.6) so that the object plane, lens plane and the image plane lie along the same line. This condition is called as the Scheimpflug condition [2].Figure 3.7 shows the the object at the blue circle on the object plane while the point of image on the image plane is shown by the red circle. This angle of inclination usually ranges from 30^0 to 50^0. Though a higher inclination gives a higher accuracy in the out of plane measurement, it also leads to image distortion which may be difficult to correct. This is achieved in practice by using a Scheimpflug adapter and its position along with its effect on the image is shown in figure 3.8

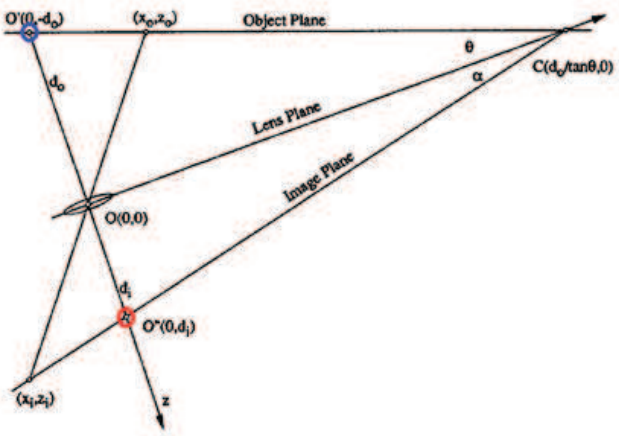

Figure 3.7: Principle of Scheimpflug [30]

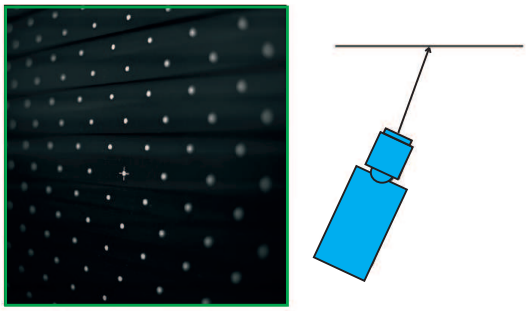

Image and arrangement of camera without Scheimpflug adpater in operation

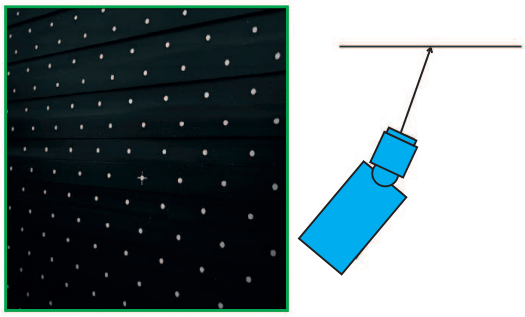

Image and arrangement of camera with Scheimpflug adpater in operation

Figure 3.8: Effect of Scheimpflug [1]

3.2.3 Image reconstruction based on calibration

A calibration based image reconstruction obtains a mapping function through a process called as calibration. The mapping function is polynomial function with unknown coefficients. These coefficients are obtained by calibration.

Calibration requires a target to be placed in the plane of the object. This target is usually a plate containing a matrices of white dots placed on a Cartesian grid.

The images of the plate are acquired using the two cameras. The image plane is mapped to the object plane by a mapping function. Higher the order of this function the more the accuracy of it. Since the higher order terms account for lens distortion or other image non-linearities.

The location of these white dots is matched with a known template, this helps in determining the unknown coefficients of the mapping function. Figure 3.9 shows the calibration procedure on two different cameras in the stereo setup.

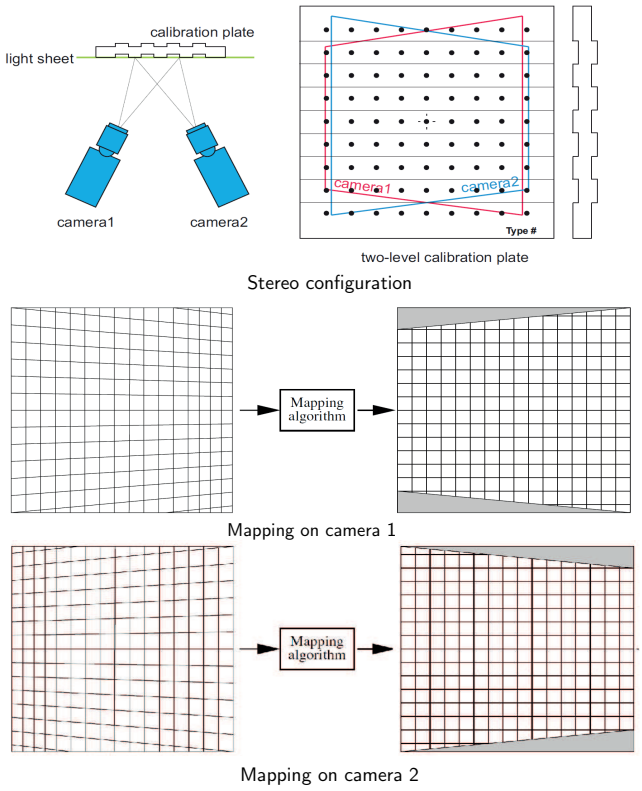

Figure 3.9: Calibration procedure on two cameras [1]

This type of calibration can be classified into two 2-D calibration and 3-D calibration. A 2-D calibration requires partial data of the geometry of the measurement setup, while a 3-D calibration does not depend on the geometry of the setup [32].

Chapter 4

Wind turbine model

4.1 Blade characteristics

The wind turbine used in the experiment is a 2-bladed wind turbine with a design tip speed ratio of 6. The rotor radius is 30cm, with a maximum twist of about 18 degrees at the root and a minimum twist of 4.4 degrees at the tip. The maximum chord of the blade is 7.4 cm which occurs at a distance of 5.5 cm from the axis. The twist and chord distribution are shown in figure 4.1.

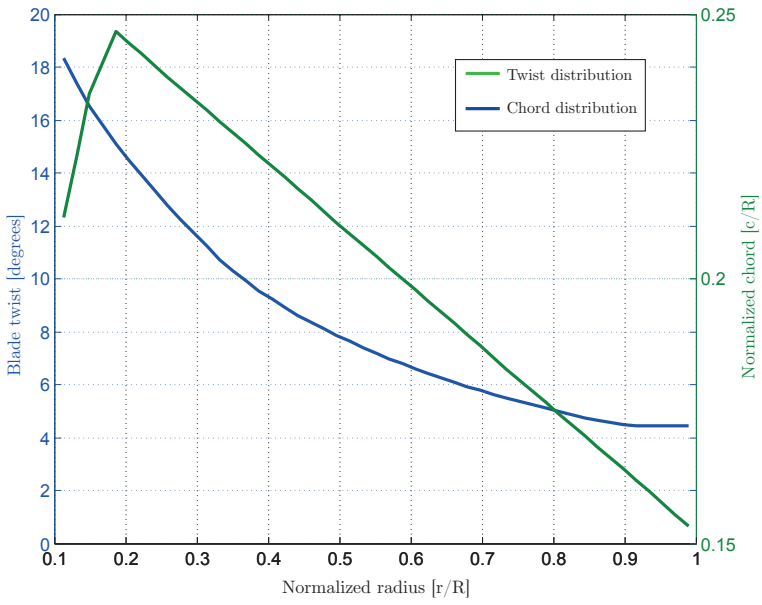

Figure 4.1: Twist and chord distribution of the blade

An Eppler E387 [41] air foil with a thickness to chord ratio of 9.06% is used along the blade span. The Reynolds number at the tip region is about 100,000 at tip speed ratio

(TSR) of 6. Figure 4.2 shows the C_l vs α curves for three different Reynolds numbers for the Eppler airfoil.

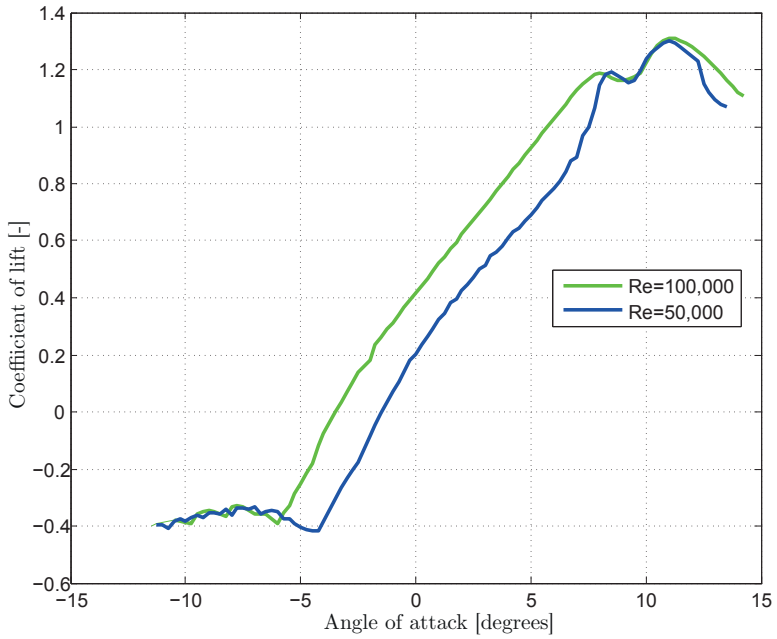

Figure 4.2: Coefficient of lift vs Angle of attack for E387 airfoil showing 3 different Reynolds numbers

The nacelle is designed in order to be compact, so that its effect on the flow is minimal. The nacelle which occupies about 6% of the total diameter, houses a DC brushless motor, a gearbox, a hall encoder and the optical trigger. The gearbox which is coupled to the brushless motor, has a gear ratio of 1:5. The whole set-up of the blades and the nacelle are mounted over a tower which is 3m tall. A drafting of the blade and nacelle assembly is shown in figure 4.3 (all dimensions on the drafting are in millimetres).

4.2 BEM results

Using the parameters such as blade twist distribution, chord distribution, airfoil polars and the thickness to chord ratio as input, a blade element method simulation is run using the software Bladed 10.1. The blade was designed by tailoring the circulation for a constant distribution over the span of the blade for the design tip speed ratio (TSR) of 6. Pradntl tip correction is taken into account during the simulation. The angle of attack as shown in figure 4.4 shows that blades reaches an angle of attack of close to 20^0, which is beyond the stall angle. This causes the blade to stall for a small section near the root.The figure 4.5 shows the root to tip distribution of Reynolds number which varies from about 20,000 at the root to about 100,000 at the tip of the blade. The circulation distribution along the span of the blade for this TSR is nearly constant as seen in figure 4.6. This is calculated using the lift coefficient (C_L) and relative wind speed (u_r) at each

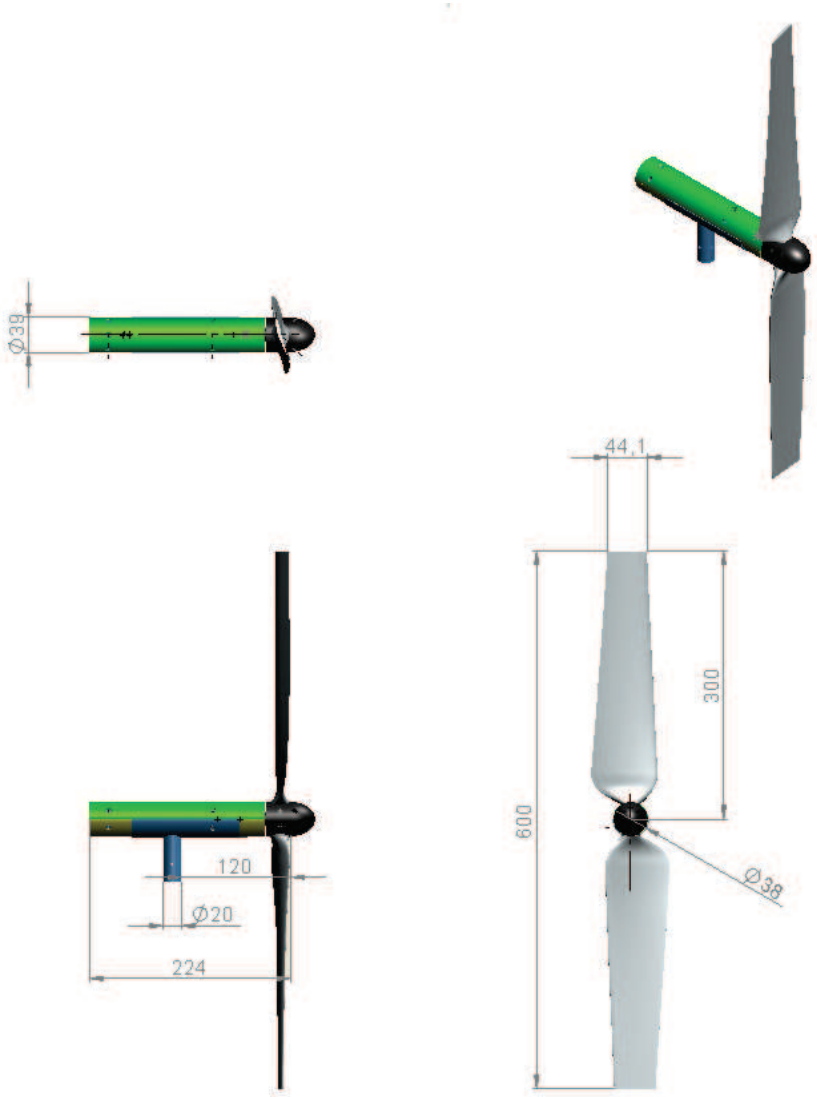

Figure 4.3: Drafting of the blade and nacelle

section as shown in equation 4.1. The chord of the blade section is denoted by c.

$$\Gamma = 0.5 \times c \times u_r \times C_l \tag{4.1}$$

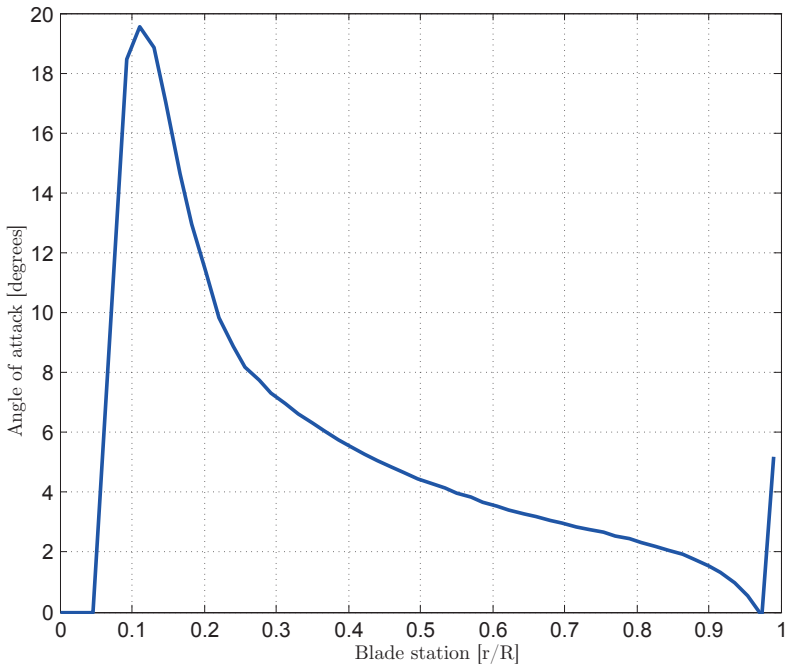

Figure 4.4: Angle of attack along the blade for TSR=6

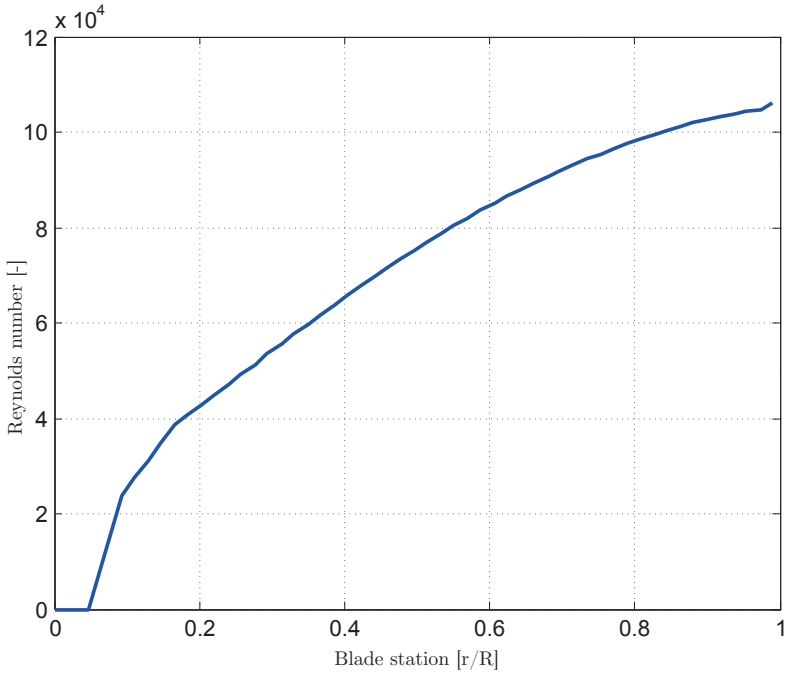

Figure 4.5: Reynolds number distribution for TSR=6

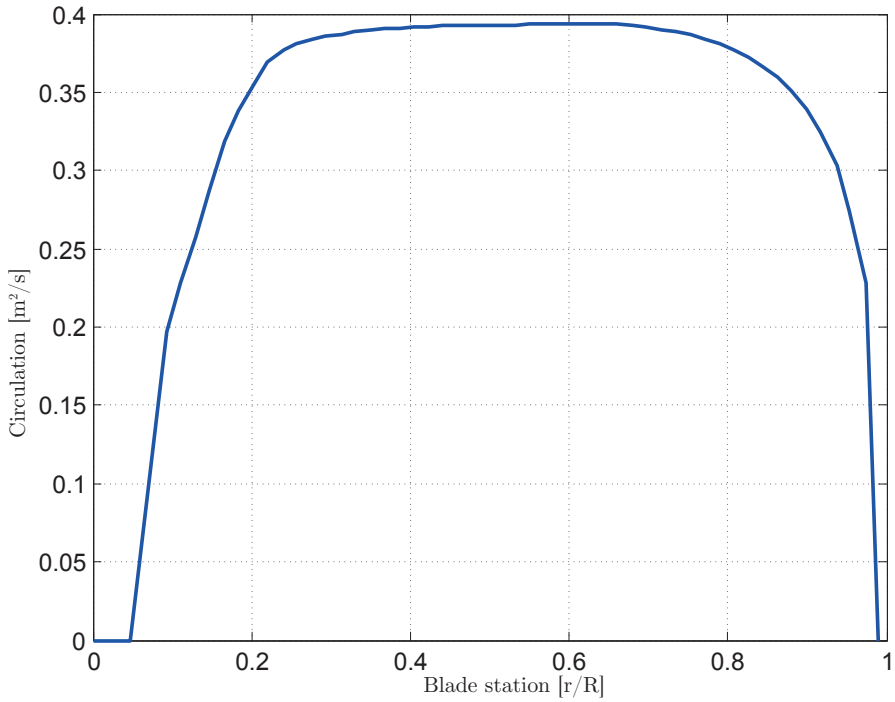

Figure 4.6: Circulation distribution along the blade for TSR=6

4.3 Force balance experiment

The Coefficient of thrust (C_T) vs Tip speed ratio (λ) characteristic of the turbine is shown in Figure 4.8. Each point in the curve has been obtained with measurement on an external 6-component balance, running the turbine at different TSR and measuring the streamwise component of the force acting the tower base. The balance contains six load cells or wheatstone bridges which give the output in terms of voltage, which can be converted into forces and moments in different directions. The load cells are sensitive only in one direction and decoupled from other directions using elastic hinges. The balance is capable of bearing upto 130% of the nominal load range of ±250 N in the axial direction, ±500 N in the y-direction and ±500 N in the vertical direction simultaneously. Figure 4.7 shows the axis convention for the force balance.

For this experiment only the axial direction of force is measured. The experiment is conducted in two stages. The first part consisted of calculating the coefficient of thrust of the whole setup mounted on the balance for a range of tip speed ratios. This is done by changing either the rotational speed of the motor or by changing the wind speed in the wind tunnel to obtain a particular tip speed ratio. Doing this ensured a spread of different tip speed ratio's from 2 to 8.

The next step involved dismantling of the blade from the nacelle and tower and calculating the thrust for the static setup. A constant value for the coefficient of thrust for the tower and nacelle for each wind tunnel setting used is computed. This accounts for the effect of tower and nacelle. This is subtracted to the results of the previous measurements on the structure with the blades. Figure 4.8 shows the even spread of data obtained from the

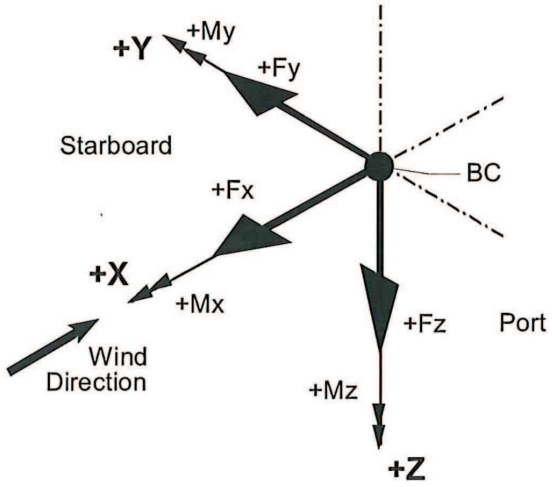

Figure 4.7: Axis convention for the force balance

experiment along with a curve fit for these points. The readings of the axial force from the experiment is tabulated and shown in the appendix.

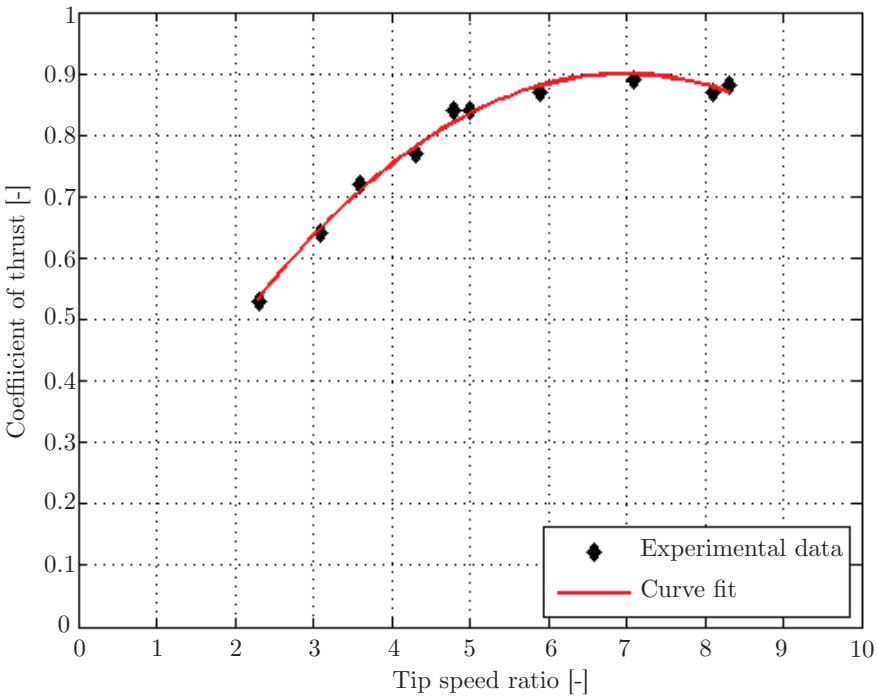

Figure 4.8: Coefficient of thrust vs Tip speed ratio

4.4 Blade assembly

In order to ensure that the blades are neutrally pitched, the blades are assembled to the nacelle by using a block. This block contains a negative impression of the blade at zero

pitch angle. For the sake of obtaining a zero pitch during assembly, the only requisite is the block being placed on a flat surface. Figure 4.9(a) and 4.9(b) show the pitching block and the assembly of the blade to the nacelle using the block respectively.

(a) Pitching block (b) Blade assembly

Figure 4.9: Assembly of blade using the pitching block

Chapter 5

Experimental Setup

The objective of the experiment was to capture a detailed measurement and analysis of the vortical structures in the wake of the horziontal axis wind turbine upto 5 diamters downstream using stereoscopic particle image velocimetry (SPIV). This is done in order to visualise the dependency between the wake re-energising process and the tip vortex helix development, in the near and far wake of the wind turbine.

The presence of periodic structures in the flow caused by the rotation of the blade, the transfer of kinetic energy from the mean flow field to the inner part of the wake is studied via a triple decomposition of the flow with mean, periodic and turbulent velocity contributions [38]. Using this procedure the periodic vortical structures can be separated from the mean flow. The following section details the procedure of triple decomposition.

5.1 Triple decomposition

Any instantaneous signal can be split into its constituent components using a triple decomposition analysis [38]. Assume a signal represented by f, the instantaneous signal can be decomposed as equation 5.1.

$$f = \overline{f} + \widetilde{f} + f' \tag{5.1}$$

In equation 5.1 $\overline{f}$ corresponds to the mean (time-averaged) contribution, $\widetilde{f}$ is the periodic single and $f^{'}$ represents the fluctuating component of the signal. Phase averaged signal i.e., average of an ensemble all at the same phase is given by equation 5.2

$$\langle f \rangle = \overline{f} + \widetilde{f} \tag{5.2}$$

In the current experiment the velocity field u_i and pressure field p_i can be written in terms of triple decomposition as equations

$$u_i = \overline{u_i} + \widetilde{u_i} + {u_i}' \tag{5.3}$$

$$p_i = \overline{p_i} + \widetilde{p_i} + {p_i}' \tag{5.4}$$

During the experiment, the mean flow contribution of the velocity field is obtained as ensemble average of a converged series of uncorrelated samples. The periodic component can be obtained using phase-locked sampling which involves collecting data at only one particular azimuthal position of the blade. Using equation 5.2 and the fluctuating component for one phase can be obtained from the phase averaged field as shown in equation 5.5.

$$\widetilde{u_i} = \langle u_i \rangle - \overline{u}_i \tag{5.5}$$

Hence it can be concluded that two different sets of readings are required in order to separate the periodical structures from the mean flow. The two sets are

1. Phase-locked sampled data
2. Unconditionally sampled data

The way kinetic energy is transported and dissipated by the vortical structures through the shear layer between the wake and the free stream defines the process of the momentum recovery of the wake, and eventually the length of the re energisation procedure. Therefore it was also decided to capture the shear layer by tracking the tip vortex, after which few specific inboard section velocity fields are to be captured.

5.2 Convergence analysis

The main objective of the present analysis is the study of turbulence in the wake of the rotor model. For this reason, the number of SPIV samplings which are acquired during the experiments must be large enough to ensure good convergence for both the statistical average value of velocity and the standard deviation of the velocity fluctuations. The acquisition of a long time series of data would not have constitute a problem in high frequency, point-wise measurement techniques, e.g. an hot wire, but when SPIV is used, the number of images which is possible to acquire is rather limited due to several reasons. The main one is that the LaVision Imager Pro LX 16 Mpix cameras have a maximum acquisition frequency of about 1Hz, which may be a tremendous limitation when large time series are to be captured in very many fields of view as in the present experiments. Hence, prior to start the acquisition, a convergence analysis has been performed by acquiring a very large amount of images in a selected location in the wake and by testing the convergence of the statistics.

Figures 5.1, 5.2 and Figures 5.3,5.4 show the evolution of the cumulative average of the three mean velocity components and the four components of the Reynolds stresses tensor as function of the number of samplings. With 400 acquisitions, convergence is guaranteed for all the phase-locked quantities and with 700 acquisition of the all the unconditionally averaged quantities. The values shown in the graphs are for a single location just after the breakdown of the wake (TSR=4.8). The plots show the velocities and Reynolds stresses are converged for both the unconditioned and phase locked data for the sample size taken.

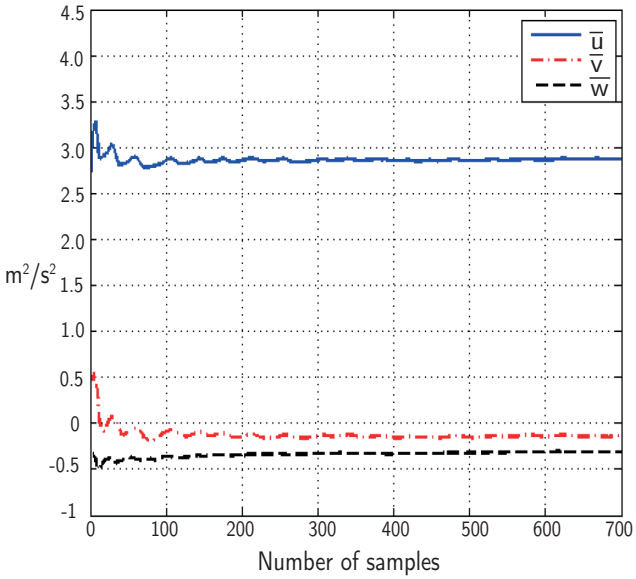

Figure 5.1: Evolution of statistical velocities for unconditional sampling

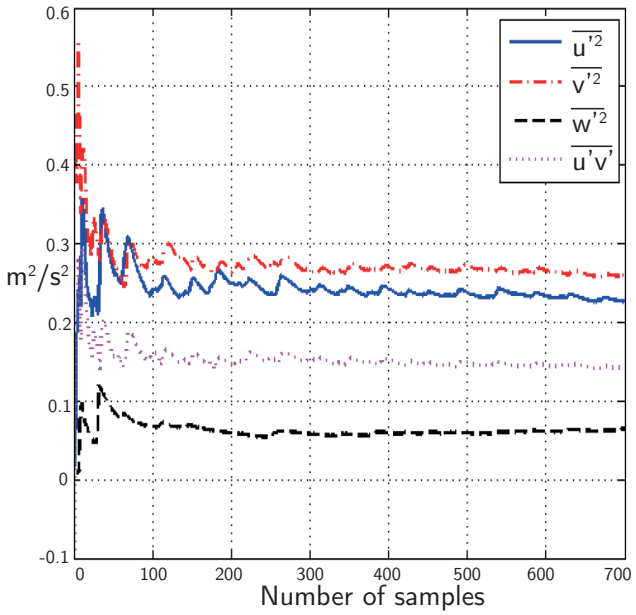

Figure 5.2: Evolution of Reynolds stresses for unconditional sampling

5.3 The experiment

The following section details the various components of the experiment starting with the wind tunnel, test conditions and the SPIV setup.

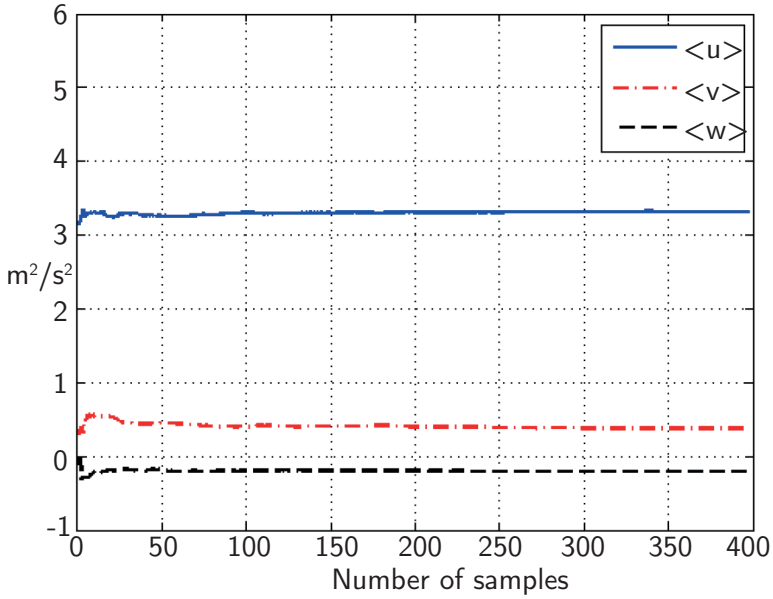

Figure 5.3: Evolution of statistical velocities for phase-locked fields

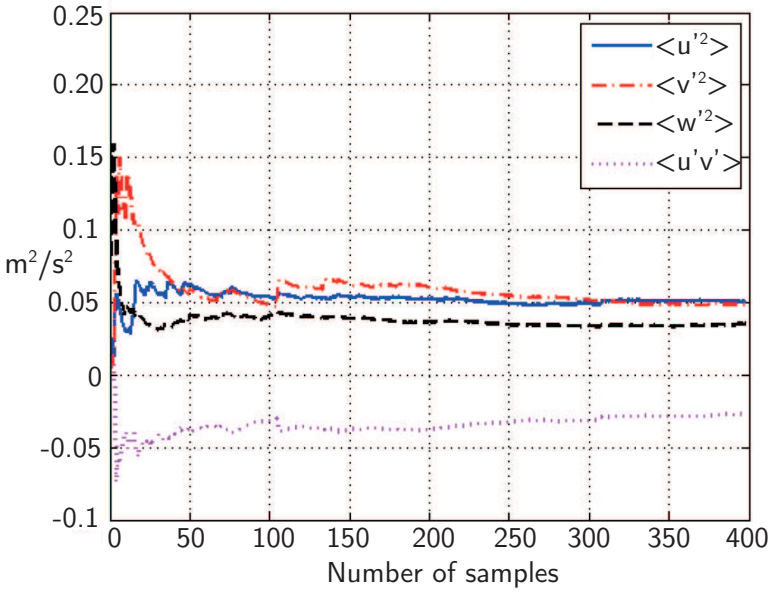

Figure 5.4: Evolution of Reynolds stresses for phase-locked fields

5.3.1 Wind tunnel

The experiments was conducted in the closed-loop open jet wind-tunnel of Delft University of Technology. The wind-tunnel has an octagonal nozzle with an equivalent diameter of 3 m and a contraction ratio of 4:1. Powered by a 500 kW motor, the wind tunnel can achieve a maximum velocity of 34m/s (120kmph). It provides a uniform flow with 0.5% turbulent intensity. The uniform velocity area contracts with a 4.75^o semi-angle, due to

the shear layer at the boundary of the jet. The flow temperature is kept constant through a heat exchanger which provides up to 350 kW of cooling power. The stable jet length has been calculated to be as long as 3m from the exit, corresponding to 5 turbine diameters in the current experiment. A schematic of the wind tunnel is shown in 5.5.

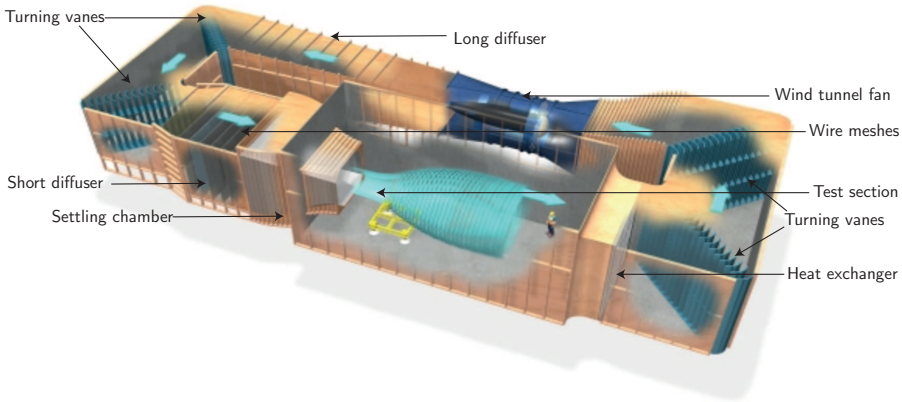

Figure 5.5: Schematic of the open jet wind tunnel (OJF)

5.3.2 Test conditions

Two different test conditions were tested during the experiment as shown in table 5.1. The tip speed ratio (TSR) of the wind turbine was varied by adjusting the wind speed of the wind tunnel which was altered by changing the fan speed of the wind tunnel and the by adjusting the frequency of the motor. The TSR of the wind turbine can be obtained from equation 5.6

$$\lambda(TSR) = \frac{\omega R}{U_\infty} \tag{5.6}$$

Where the frequency of the rotor (f in Hz) can be converted into rotor rotational speed in radians/second by using the formula in equation 5.7

$$\omega = 2\pi f \tag{5.7}$$

5.3.3 Stereo particle image velocimetry setup

The stereoscopic PIV setup is installed on a traversing system able to scan the flow field in the wake of the horizontal-axis wind-turbine model. The traversing system is capable

TSR[-]	Rotor frequency [Hz]	Free stream velocity [m/s]	Coefficient of thrust [-]
4.8	9.67	3.8	0.82
6	18.00	5.7	0.89

Table 5.1: Test conditions for the two cases

of moving in two directions. The traversing system has a maximum capability of moving 130 cm in the x-direction and 35 cm in the y-direction. The cameras and the laser are mounted on the same structure which in turn is mounted on this traversing system, thus guaranteeing the same setup while the traversing systems travels.

The required illumination is provided by a Quantel Evergreen Nd:YAG laser system with 200 mJ/pulse energy at a max frequency of 15 Hz (527 nm wavelength). The laser light is conveyed to form a 2 mm laser sheet of about 35 cm width at the field of view, by combination of a spherical lens of focal f=-50 mm and two cylindrical lenses of f=+80 mm and f=-40 mm.

Two LaVision Imager Pro LX 16 Mpix (4870x3246 px^2, 12 bits) with pixel pitch of 7.4 μm/px are used to image a field of view of 357x253 mm^2, obtained with two Nikon lenses of f = 180 mm and aperture f-stop = 2.8 - 4, at a magnification M of 0.10 The focusing plane has been slightly offset with respect to the laser plane (defocussing), to obtain an image of the particle of about 2-3 px, to mitigate the bias errors associated with peak locking. Two Scheimpflug adapters are attached to the cameras for satisfying the Scheimpflug prinicple and to obtain a uniformly focussed image. A daylight filter is attached to the lens in order to reduce the ambient light which is captured by the camera.

Seeding is provided in the test section by a SAFEX smoke generator with SAFEX MIX, able to produce liquid droplets of less than 1 μm. The SAFEX MIX is a Diethyl glycol-based mixture. The generator consists of an electrically heated hot plate over which the SAFEX MIX would drip and evaporate to form the required smoke.

The laser control, camera synchronization, and image acquisition are triggered by an opto-coupler TCST 2103, together with a disc perforated at a specific azimuthal position and rotating with the turbines shaft providing a one-pulse digital signal for each rotation.

Case 1: Wake experiment setup
The objective of the experiment is to capture the wake from the near wake to a downstream distance of about 4 rotor diameters. The cameras are mounted on either side of the tower with an inclination with respect to the horizontal plane. The same setup is continued beyond the point of maximum traverse by moving the whole traversing system downstream (x-direction). Figure 5.6 shows the schematic of the setup used for the experiment.

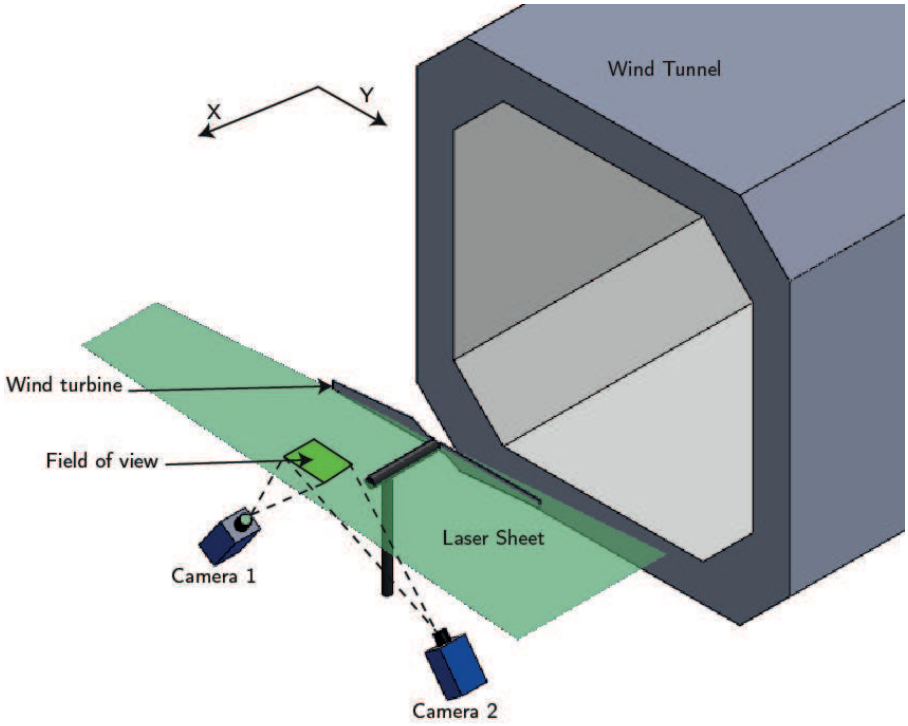

Figure 5.6: Schematic of the setup for wake experiment

Case 2: Blades experiment setup
The setup used for capturing the wake is not capable of obtaining data close to the blade because of the presence of the tower and nacelle. Hence camera 2's position is changed with respect to the previous experiment. This setup requires a separate calibration, since the position of the camera has been changed. The schematic of the setup is shown in the figure 5.7.

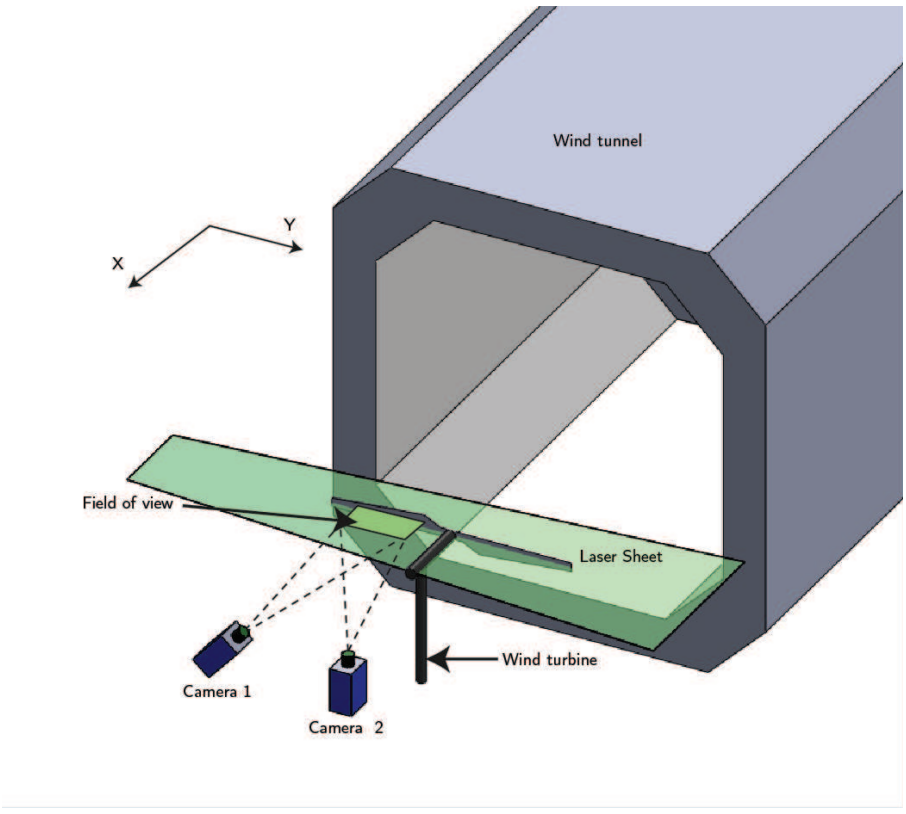

Figure 5.7: Schematic of the setup for blades experiment

Case 3: Loads experiment setup
The objective of the loads experiment is to obtain the velocity fields around the blades for different sections. Using these velocity fields the pressure distribution over the blade section can be obtained and hence the loads. The laser sheet is made vertical and the cameras placed perpendicular to it. The traversing system is moved in steps in the inboard direction (y-direction) from the tip to the root. Figure 5.8 shows the schematic of the setup for loads experiment.

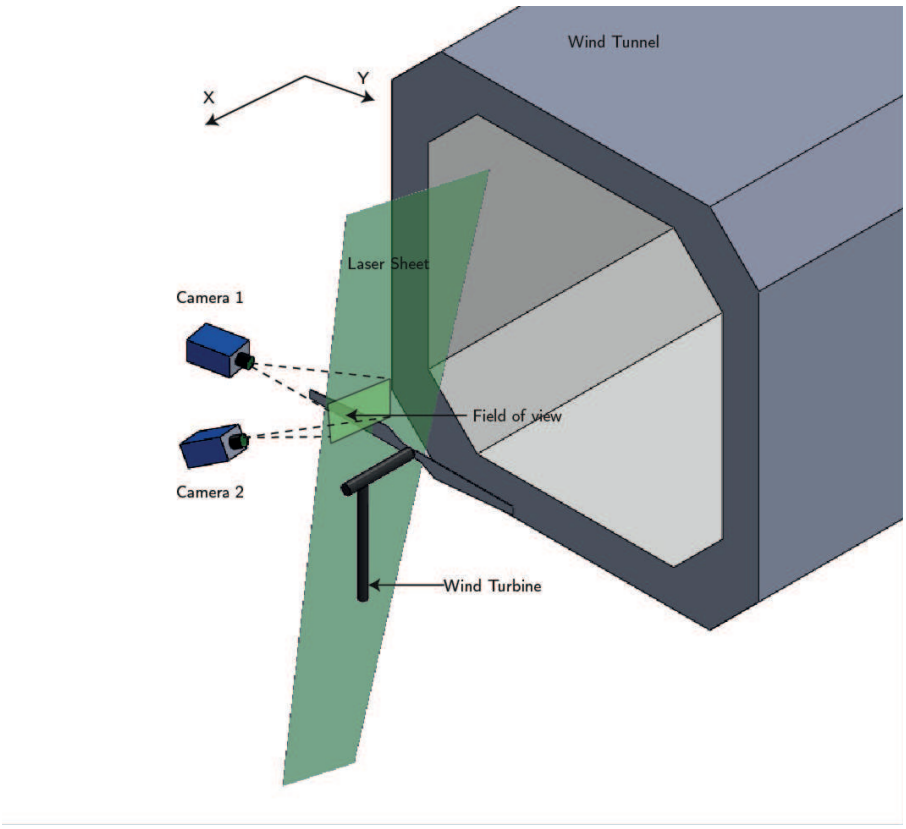

Figure 5.8: Schematic of the setup for the loads experiment

5.4 Measurement matrices

The measurements were performed on the wake of the wind turbine up to 4 rotor diameters downstream. Each window represents a field of view (FOV) in a plane parallel to the ground at the hub height; the darker shade between the windows shows the overlap between two adjacent FOV, which varies from 97 mm to 147 mm in the x-direction. The flow was also captured at two inboard positions with an overlap of 102 mm to 98 mm respectively. The measurements were performed in unconditioned sampling and in phase-locked sampling for different azimuthal positions of the blades (-5, 0 and 5 degrees), using an optical trigger positioned inside the nacelle.Figure 5.12 and 5.10 shows blank spaces around 2.5 diameters due to absence of data.

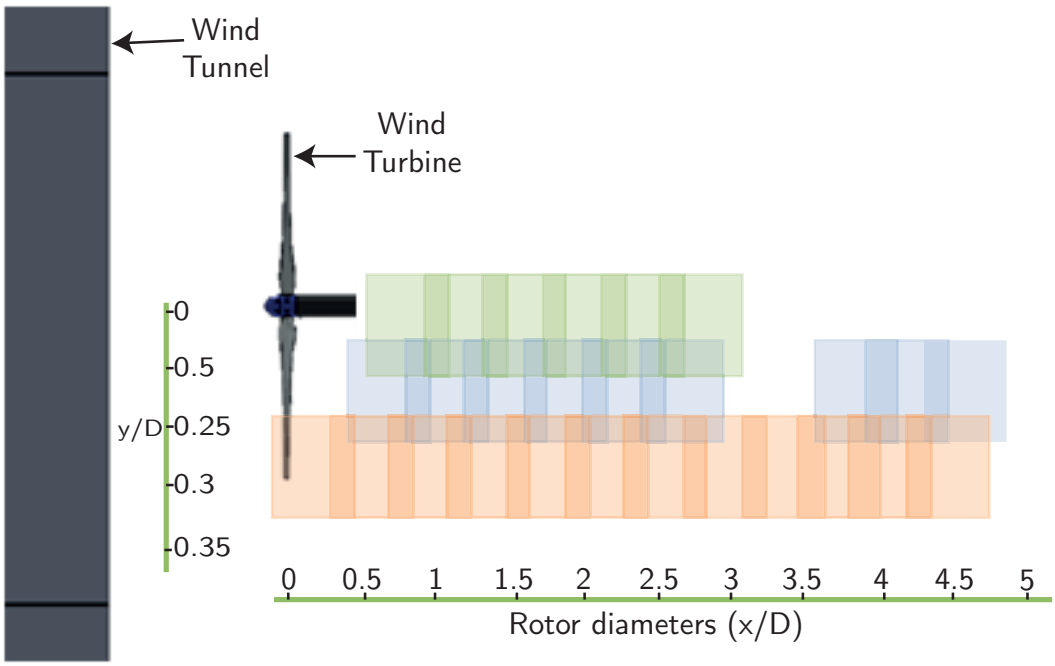

Figure 5.9: Measurement matrix for TSR = 6 phase locked measurements

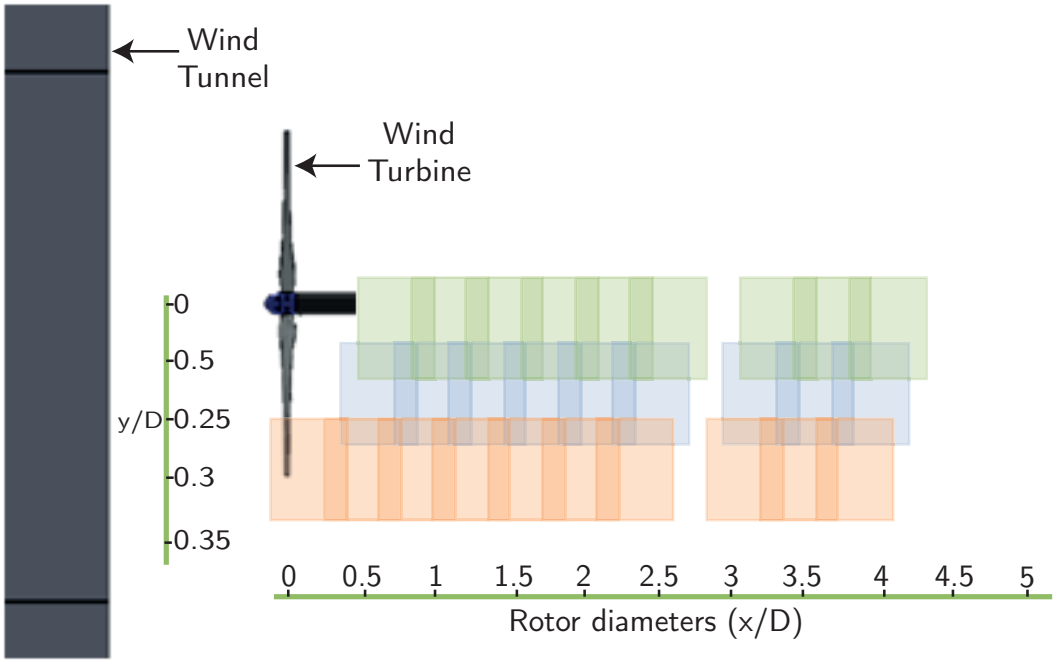

Figure 5.10: Measurement matrix for TSR = 4.8 phase locked measurements

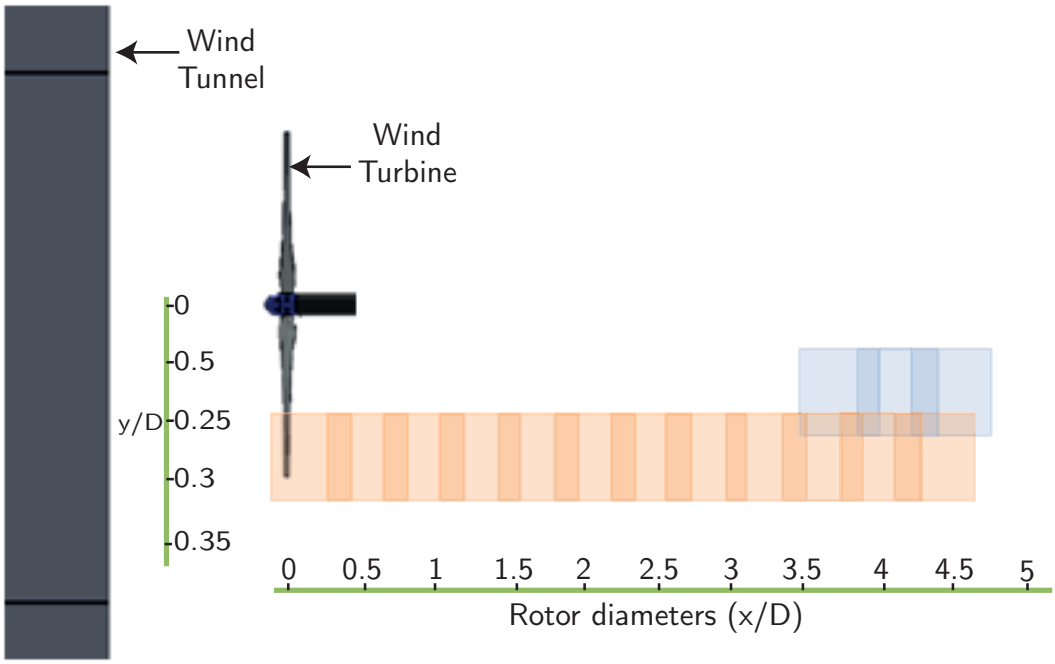

Figure 5.11: Measurement matrix for TSR = 6 uncorrelated sample measurements

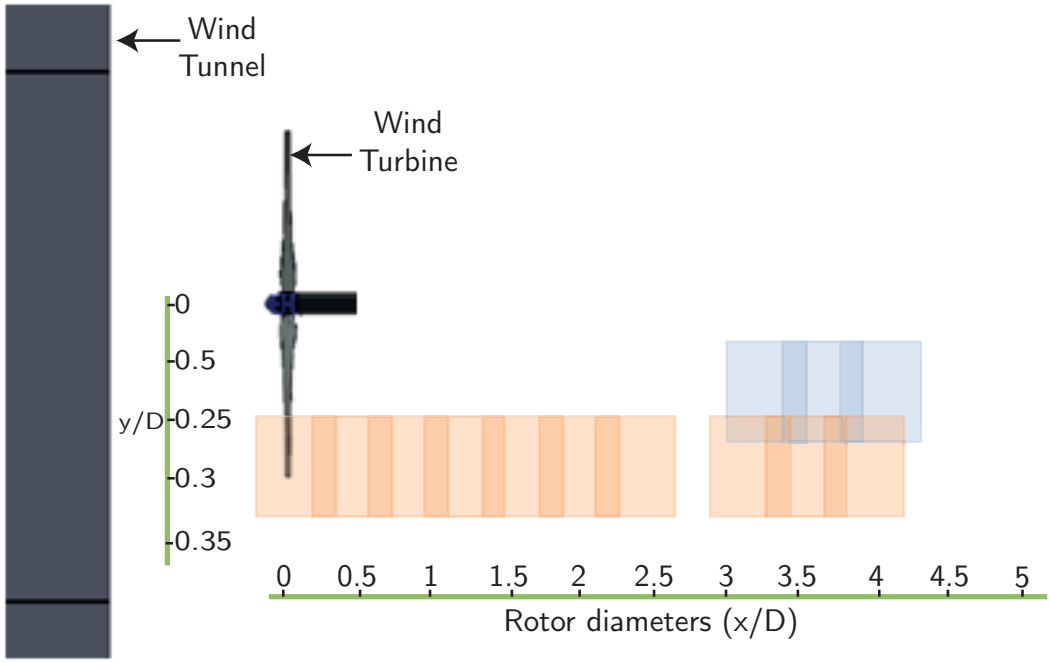

Figure 5.12: Measurement matrix for TSR = 4.8 uncorrelated sample measurements

5.5 Image processing

Post-processing of the images were done using DaVis 8.1.3. This is done in three steps namely

- Pre-processing
- Processing
- Post processing

The first step of post-processing involved computing the average minimum of the raw images. The background noise of the raw image is removed by subtracting this minimum. Figure 5.14 shows the effect of removing the background noise compared to the raw image shown in figure 5.13

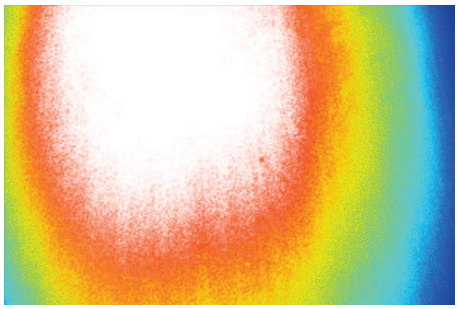

Figure 5.13: Raw image obtained from the measurements

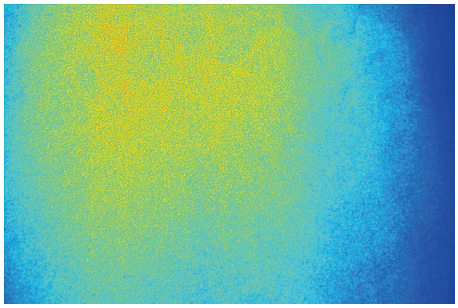

Figure 5.14: Image with minimum subtracted

The second step of pre-processing involved applying a 3x3 Gaussian filter onto the images obtained from the previous step. Applying a 3x3 Gaussian filter reduces the noise in the image, it also reduces the chances of peak locking to occur. Figure 5.15 shows the result of the image when a 3x3 Gaussian smoothing filter is applied on the image.

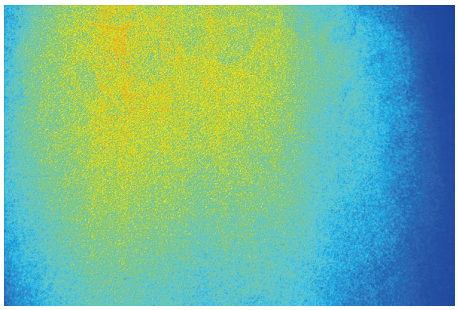

Figure 5.15: A 3x3 Gaussian filter applied to the image

The next stage involved the actual processing of the data using cross-correlation analysis method. The actual procedure for this stage is explained in chapter 3. The images were processed with a final interrogation size of 24x24 pixel^2, multipass correlation with a 50% overlap ratio. The separation time between two images was 200 μs. This yields a result for each image giving an instantaneous velocity field for each image. An example of such an

image is shown in figure 5.16. It can be seen from figure 5.16 that the shape of the image doesn't remain a rectangle anymore. This is because of the application of calibration on the images.

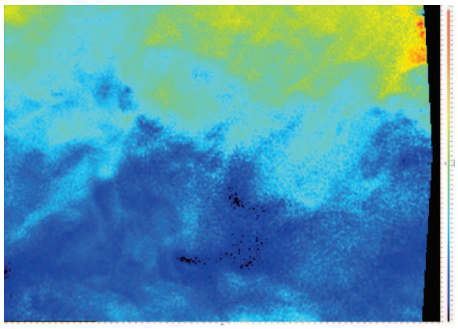

Figure 5.16: Instantaneous velocity field

The post-processing stage involved removing spurious vectors which would have crept up during the processing phase. This was done using a median filter. The results from the instantaneous were averaged to give the final results in terms of 3 component velocities (u,v and w) and its magnitude along with the Reynolds stresses in xx,yy,zz,xy,xz and yz directions. The following figures 5.17(a) ,5.17(b) shows the velocities in x and y direction respectively.

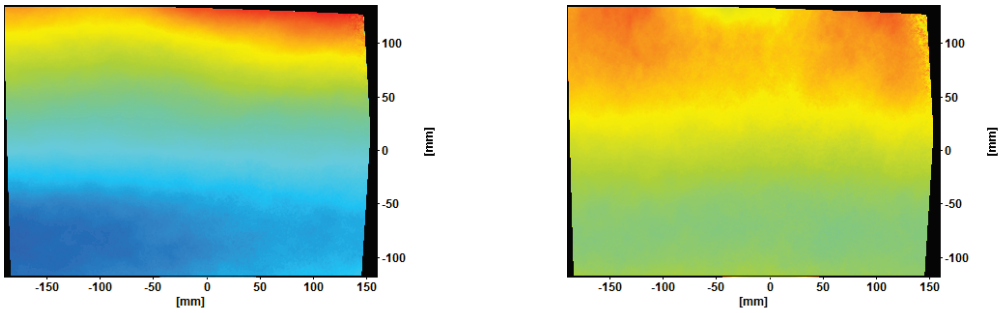

(a) Velocity field in x-direction

(b) Velocity field in y-direction

Figure 5.17: Velocity fields obtained from PIV

These individual images for different locations are stitched together to get the global view of the wake.

Table 5.2 shows the summary of PIV parameters and processing settings

Parameter	Value
Field of view (mm^2)	357x253
Optical magnification	0.10
Pulse delay (μs)	200
Ensemble size (images)	Phase locked: 400, Uncorrelated: 720
Type of image processing	Stereo cross-correlation
Overlap	50%
Final interrogation window size (pixel)	24x24
Vector resolution (mm)	1.76
Vector pitch (mm)	0.88

Table 5.2: PIV parameters and processing settings

Chapter 6

Experimental results

This chapter details the results obtained from the experiment for the two set of data sets namely the phase-locked fields and the unconditionally sampled fields. The field set consists of the axial velocity field, radial velocity field, azimuthal velocity field, velocity magnitude with velocity vectors, Reynolds stresses in x-y direction and turbulence intensity. This is followed by the analysis from the results containing information regarding the vortex field and circulation, vortex comparison with Lamb-Oseen model, velocity distribution in the wake and the calculation of static pressure and enthalpy in the field. The next section contains results from the blades experiment using which the circulation along the blade span is computed and compared with the results obtained from BEM model. The final part contains the preliminary results of loads calculated on two sections.

6.1 Phase locked fields

Three different azimuthal angles were recorded during the experiment. The three different angles that were recorded are -5, 0 and 5 degrees. The following sections present the results for a phase angle of zero degrees. The individual images taken at different locations with an overlap of fields of view are stitched together, by placing the images one over the other. This gives a global picture of the wake.

6.1.1 Case 1: TSR = 6

Figure 6.1(a) shows the phase-locked velocity field of the shear layer and the inboard region till the hub centreline for tip speed ratio of 6. The velocity fields are normalized with respect to the free-stream velocity. It can been seen that the region outside the wind turbine wake has a u/U_∞ =1, which is indicative of the fact that the flow has a velocity equal to that of the free-stream velocity. Inside the wake the normalized velocity is about 0.3 times of the free stream velocity, which satisfies the result from actuator disk theory. From the figure the tip vortices emanating from the blade tip are clearly visible along with

the pairwise interaction called leap-frogging of two vortices close to 1.5 rotor diameters downstream. The evolution of the tip vortex together with its pairwise interaction shows a predominant tip vortex diffusion after the leap frogging event. This would suggest a strong influence of the large scale wake instability on the tip vortex diffusion.

Figure 6.1(b) shows the velocity field on the radial direction normalized with respect to the free stream velocity. Positive direction in the velocity field implies the flow direction moving outboard towards the freestream, while negative denotes the direction towards the nacelle. The velocity field shows that rotation of the vortex filaments. The rest of the wake and freestream do not show any other specific regions of interest in the radial velocity field. Figure 6.1(c) shows the azimuthal velocity field normalized with respect to the free stream velocity. A positive velocity magnitude indicates the velocity component coming outside, from the plane of measurement. In the velocity field, a trail of the vortex roll-up from the span of the blade with regions of positive velocity mean flow rotating in the same direction of the blades are visible. This is due to the viscous drag (e.g. the tip-vortex cores and the wakes of the blades), whereas negative regions represent counter rotating flow in the wake.

The Reynolds stresses and turbulence intensity fields shown in this chapter are not normalized. Figure 6.2 shows the magnitude of velocity in the wake along with the vectors pointing the local direction of the flow. Figure 6.3(b) shows the turbulence intensity in the wake. Turbulence intensity is defined as the ratio of the RMS of velocity fluctuations to that of the free stream velocity. The phase-locked average turbulent kinetic energy is calculated using the equations 6.1, 6.2, 6.3

$$TI_{\phi} = \frac{\langle u_{RMS} \rangle_{\phi}}{U_{\infty}} \tag{6.1}$$

$$\langle u_{RMS} \rangle_{\phi} = \sqrt{\frac{1}{3}\left(\sum_{i=1}^{3} \overline{u_i' u_i'}\right)_{\phi}} \tag{6.2}$$

$$\left(\overline{u_i' u_i'}\right)_{\phi} = \sum_{k=1}^{N} \frac{\left(u_i(t_{k,\phi}) - (u_i)_{\phi}\right)^2}{N} \tag{6.3}$$

Where $t_{k,\phi}$ is the sampling time at a phase ϕ, N is the size of the sample. The random turbulent fluctuation on a specific phase are accounted for in the above equations. The turbulence intensity field shows high values close to the blade owing to the presence of strong concentrated vortices and this concentration disappears as it moves downstream.

Figure 6.3(a) shows the Reynolds stresses in the wake in x-y direction. The Reynolds stresses are calculated using equation 6.4. Where for the case of the x y component, i=1 and j=2.

$$\langle u_{s,i} u_{s,j} \rangle = \frac{\sum_{k=1}^{N} \left(u_{i,k} - \langle u_i \rangle\right)\left(u_{j,k} - \langle u_j \rangle\right)}{N} \tag{6.4}$$

The phase-lock average x-y component of the shearing stresses is an important quantity because, this is related to the vertical transport of momentum, with negative values of shear meaning entrainment into the wake of the free stream flow momentum and as such directly related to the re energising process. This has been demonstrated by Hamilton et al. [22].Two regions can be distinguished in the figure of Reynolds stresses. In the near-wake region the distribution of shearing stresses is strongly influenced by the evolution of the tip vortex structure, with a concentration of the shearing stresses near the vortices. In the region after the instability, a rapid breakdown can be observed. The shearing stresses become suddenly larger and with negative sign, suggesting a more violent mixing, characterised by a strong entrainment of free stream momentum. The separation from the nacelle and the root vortex also shows a region with high positive and negative values of Reynolds stresses which disappear at a downstream distance of less than 2D.

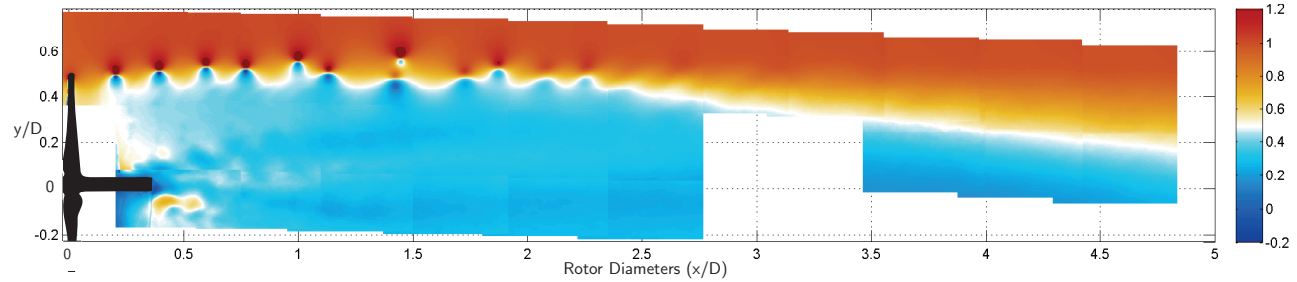

(a) Axial velocitiy field

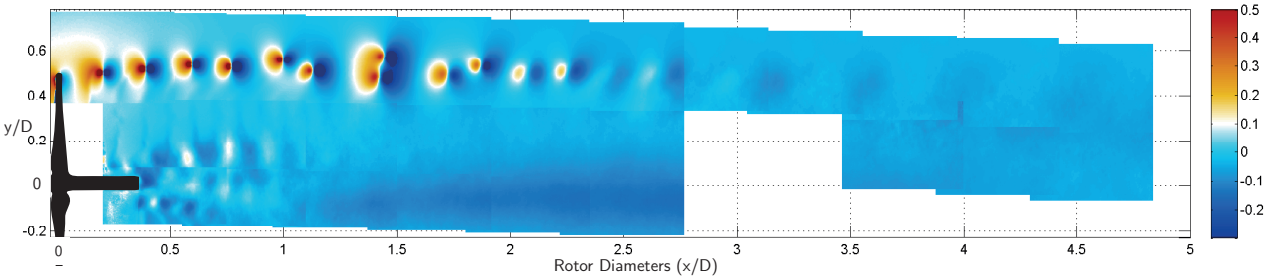

(b) Radial velocity field

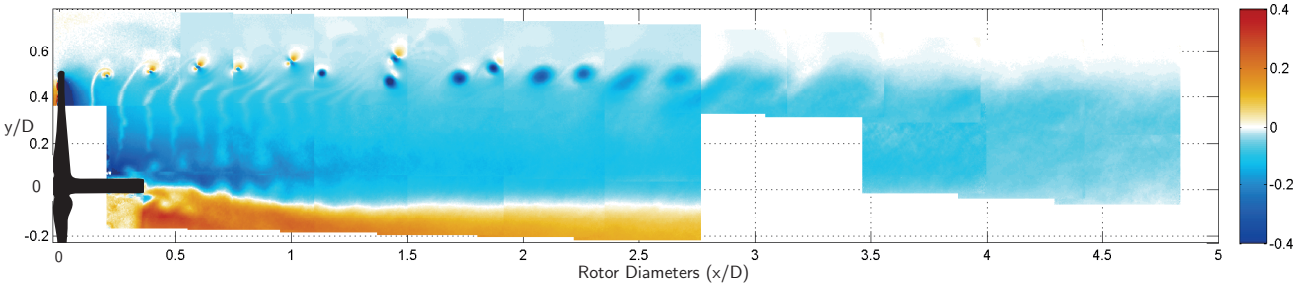

(c) Azimuthal velocity field

Figure 6.1: Averaged phase-locked velocity field (normalized with respect to free-stream velocity)for TSR=6

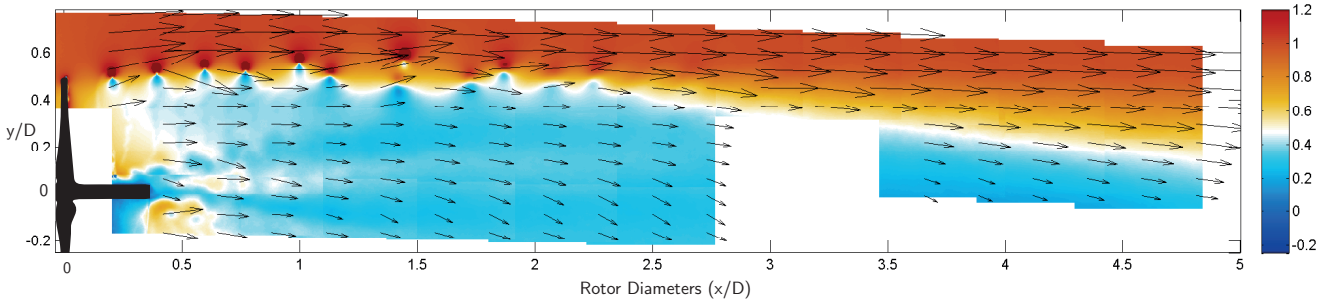

Figure 6.2: Averaged phase-locked velocity magnitude field (normalized with respect to free-stream velocity) for TSR=6

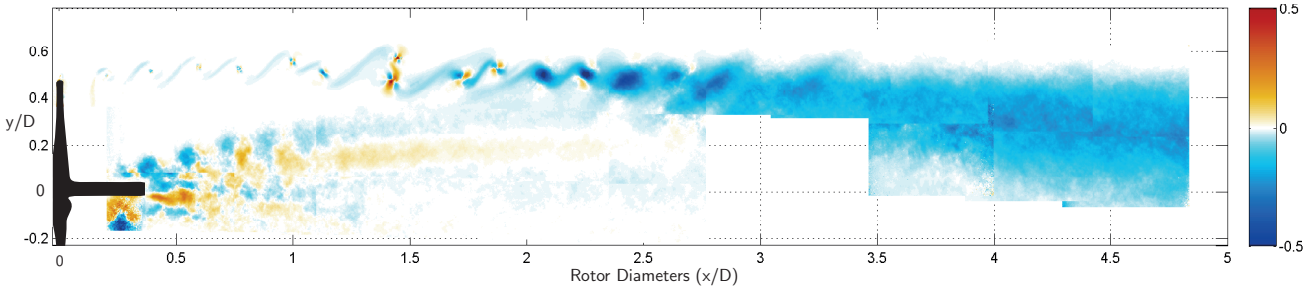

(a) Reynolds stresses in x-y direction

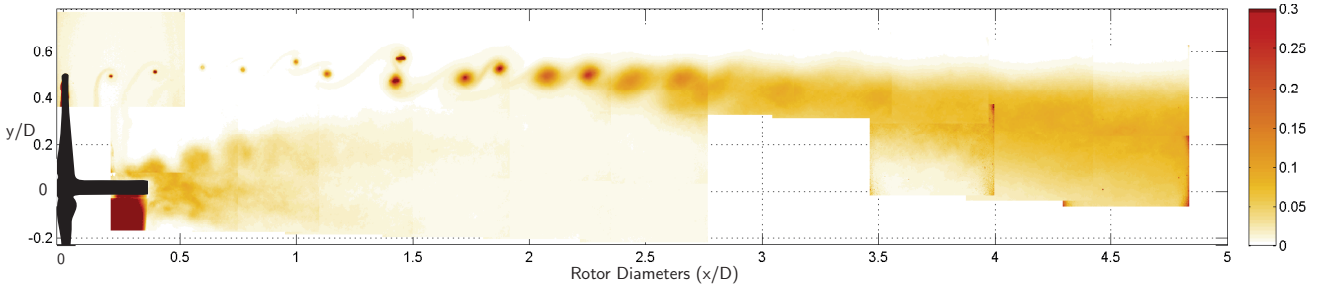

(b) Turbulence intensity

Figure 6.3: Averaged phase-locked Reynolds stresses and turbulence intensity for TSR=6

6.1.2 Case 2: TSR = 4.8

All the results for this case show the region between about 2.75D to 3.1D as blank space due to absence of data.

Figures 6.4 shows that the tip vortices interact and leapfrog just like in the case of the higher tip speed ratio in previous section. The interesting aspect of this is the distance at which the leapfrogging occurs compared to that in the case of a higher tip speed ratio. In this case the leapfrogging occurs at around 2 diameters downstream, farther downstream than the previous case. This can be explained in terms of the distance between the two different helices generated by each blade. As the tip speed ratio decreases the distance between each helix increases causing the leapfrogging to occur at a more downstream location. This clearly indicates that the distance at which leapfrogging occurs is a function of the distance between the helices emanating from the blade. This dependency on tip speed ratio is also demonstrated by Felli et al.[18].

Figure 6.10 shows the velocity vectors pointing inside towards the wake from the shear layer where the velocity is about half of the free stream velocity. This trend is also observed in the case of TSR=6. The Reynolds stresses in the x-y direction shown in 6.6(a), similar to the previous section two distinctions can be made in the wake depending on the magnitude of the stress. The first one in the near wake where the majority of the stresses are dominated by the root vortex and seperated flow from the nacelle, though they die out close to 1.5D. The region beyond this sees the effect of the vortex leapfrogging causing the the stresses to have a high negative magnitude in this region.

Figure 6.6(b) shows the turbulence intensity calculated behind the turbine in the wake. Compared to the turbulence intensity seen in the wake from TSR=6, it can be clearly seen that for the same distance downstream, TSR=4.8 has lesser turbulence intensity clearly showing the effect of leapfrogging on the increase in turbulence intensity.

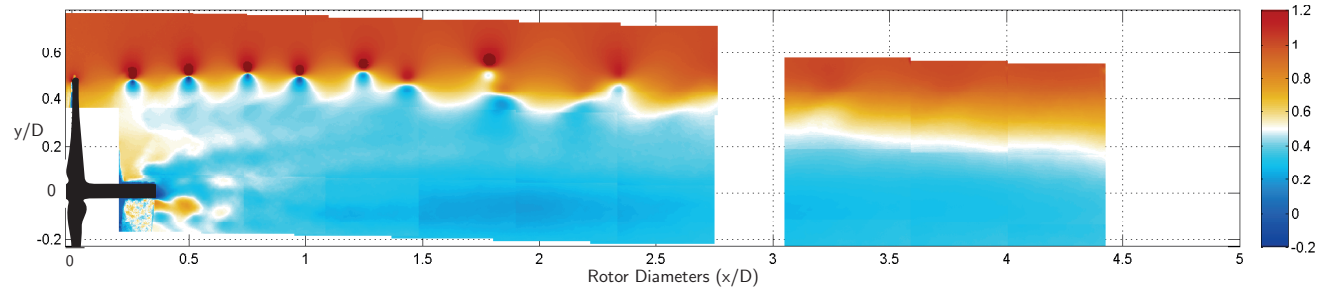

(a) Axial velocitiy field

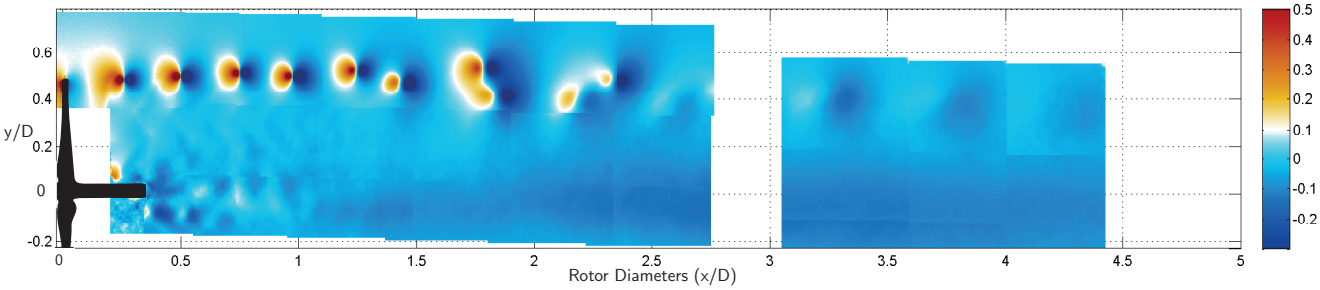

(b) Radial velocity field

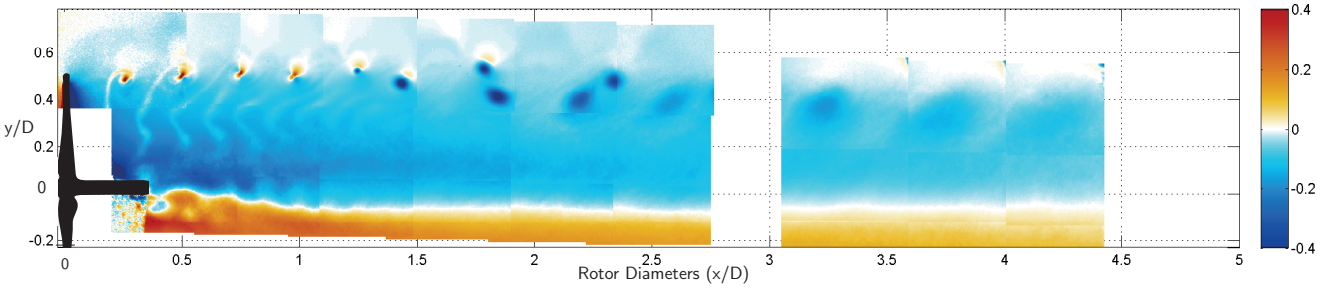

(c) Azimuthal velocity field

Figure 6.4: Averaged phase-locked velocity field (normalized with respect to free-stream velocity)for TSR=4.8

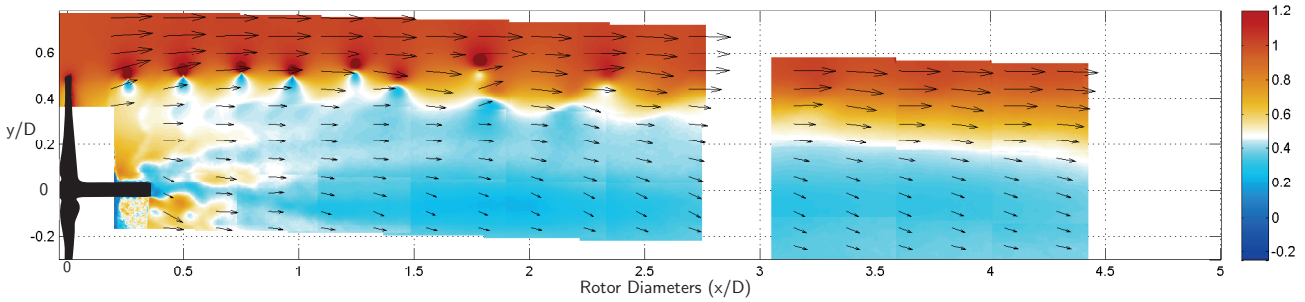

Figure 6.5: Averaged phase-locked velocity magnitude field (normalized with respect to free-stream velocity) for TSR=4.8

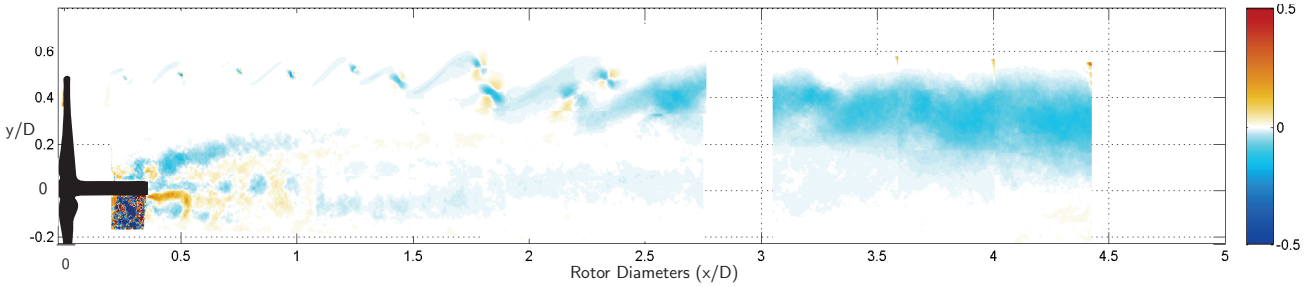

(a) Reynolds stresses in x-y direction

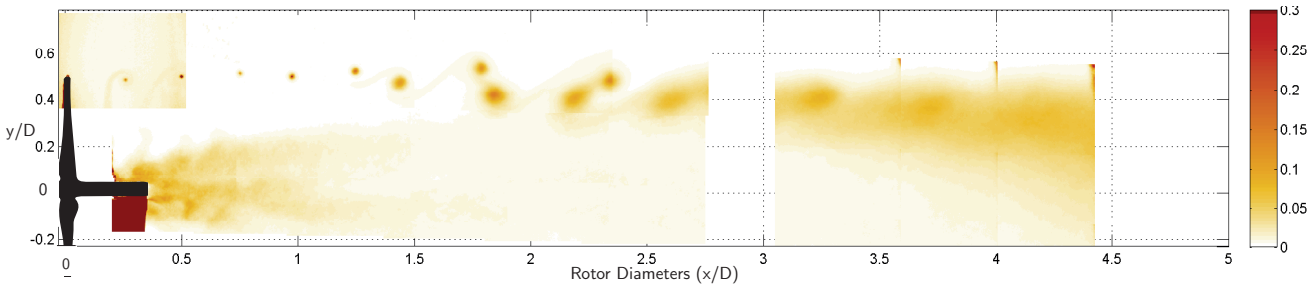

(b) Turbulence intensity

Figure 6.6: Averaged phase-locked Reynolds stresses and turbulence intensity for TSR=4.8

6.2 Unconditionally sampled fields

6.2.1 Case 1: TSR 6

The following section details the average velocity fields for an unconditional sampling. Figures 6.7(a) and 6.7(c) shows sudden enlargement of the shear layer for this tip speed ratio on account of leapfrogging of tip vortices. The expansion of the shear layer starts at about 1 rotor diameter downstream and reaches a maximum at about 1.4 diameters. The shear layer after the leapfrogging starts contracting towards the axis, reaching close to 0.1D radially at about 4.8 diameters. The velocity contour for radial velocity shows From figure 6.8 it can be seen that the velocity vectors show that the flow starts to move from the free-stream into the wake right from the first inboard location which is at about 3.5 diameters.

The Reynolds stresses calculated shown in 6.9(a) is calculated using the formula in equation 6.5. In the equation for calculation Reynolds stresses in x-y direction i=1, j=2.

$$\overline{u_i' u_j'} = \sqrt{\frac{\sum_{k=1}^{N} (u_{i,k} - \overline{u_i})(u_{j,k} - \overline{u_j})}{N}} \tag{6.5}$$

It can been seen that the Reynolds stresses are concentrated as a thin sheet along the path of the vortex. The shear stresses are negative in this region. The interesting aspect of this field can be seen at the point where the leapfrogging starts, it can be seen that thickness of the layer increases and after the point where one vortex is over each other a sudden change in the direction of the shear stress is observed. After the breakdown of the tip vortices, the Reynolds stresses become negatively concentrated showing a behaviour similar to the Reynolds stress field from the phase-locked fields.

The turbulence intensity is calculated using the equations 6.6, 6.7, 6.8

$$TI = \frac{u_{RMS}}{U_\infty} \tag{6.6}$$

$$u_{RMS} = \sqrt{\frac{1}{3}\left(\sum_{i=1}^{3} \overline{u_i' u_i'}\right)} \tag{6.7}$$

$$\overline{u_i' u_i'} = \sum_{k=1}^{N} \frac{\left(u_i(t_k) - \overline{u_l}^2\right)}{N} \tag{6.8}$$

Where t_k is the sampling time and N is the total number of samples. From figure 6.9(b) shows the turbulence intensity in the wake. It can be seen that higher values of TI are observed close to the blades are due to the presence of strong concentrated vortices which are released at the blade tip. It also worth noticing that the contribution of the coherent structures vanishes the further downstream it travels.

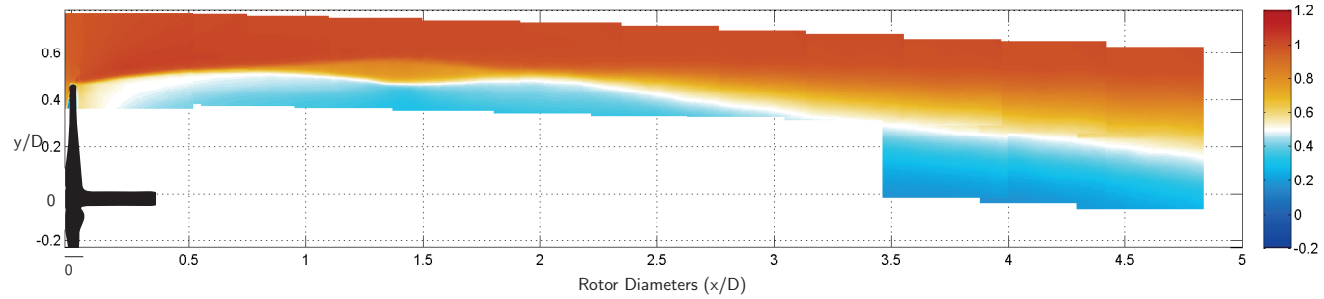

(a) Axial velocitiy field

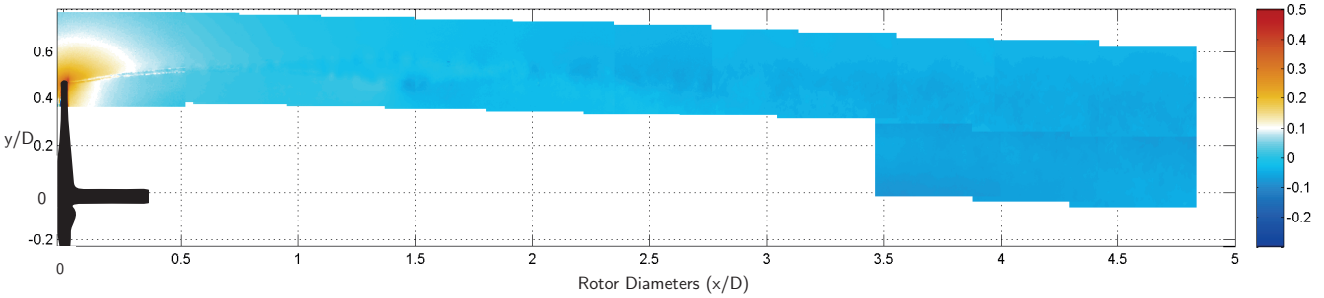

(b) Radial velocity field

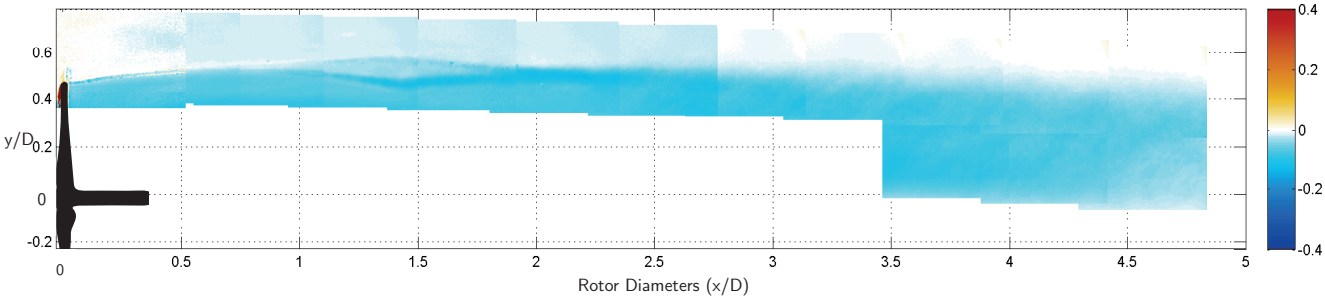

(c) Azimuthal velocity field

Figure 6.7: Unconditional averaged velocity field (normalized with respect to free-stream velocity)for TSR=6

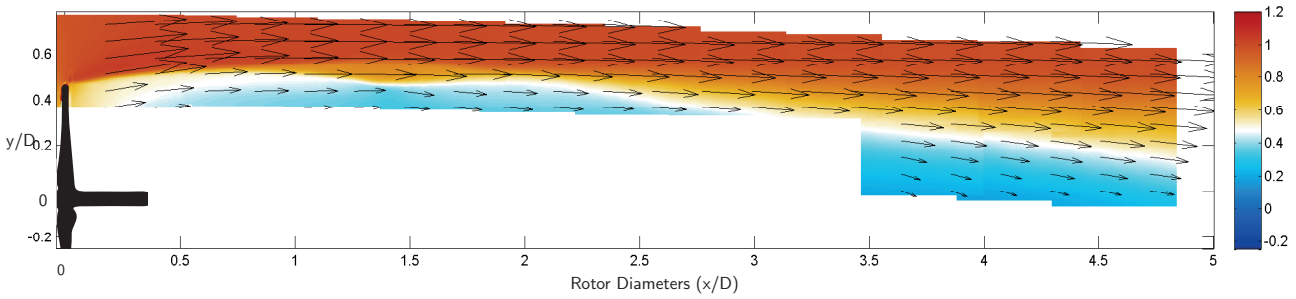

Figure 6.8: Unconditional averaged velocity magnitude field (normalized with respect to free-stream velocity) for TSR=6

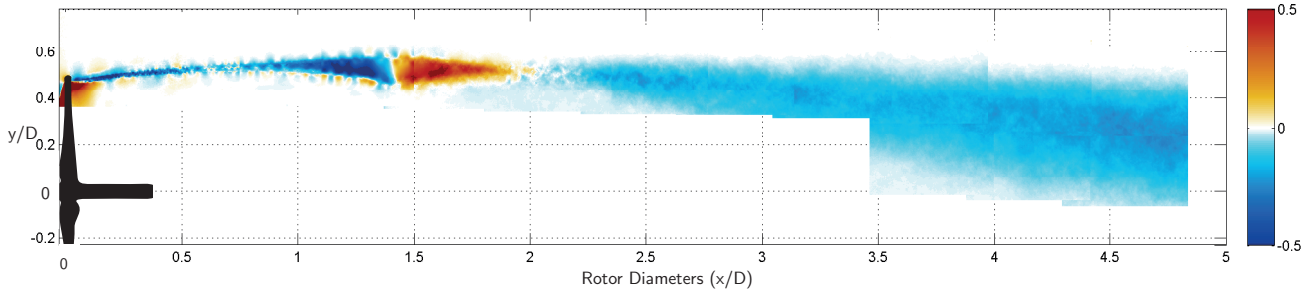

(a) Reynolds stresses in x-y direction

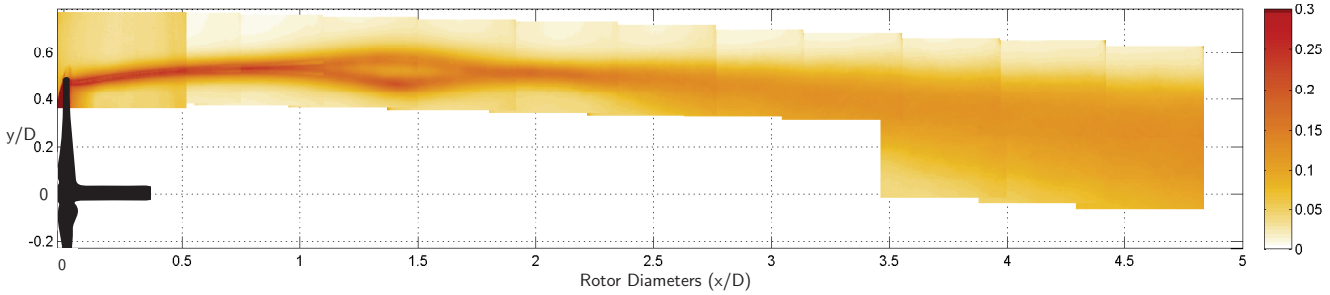

(b) Turbulence intensity

Figure 6.9: Unconditional averaged Reynolds stresses and turbulence intensity for TSR=6

6.2.2 Case 2: TSR 4.8

Figures 6.11(a) and 6.11(c) shows sudden enlargement of the shear layer for this tip speed ratio on account of leapfrogging of tip vortices just like in the previous section. The expansion of the shear layer starts at about 1.5 rotor diameter downstream and reaches a maximum at about 1.7 diameters. This is at a higher downstream distance that the case of tip speed ratio of 6. This clearly reflects the influence of tip speed ratio on the position of leap-frogging as also seen from the phase-locked readings. The shear layer after the leapfrogging starts contracting towards the axis, reaching close to 0.3D radially at about 4.4 diameters.

The velocity contour for radial velocity shows From figure 6.8 it can be seen that the velocity vectors show that the flow starts to move from the free-stream into the wake from the first inboard location shown close to 3 diameters.

The Reynolds stresses shown in 6.12(a) shows a similar behaviour to the previous cases, wherein a change in direction of the Reynolds stres6s is observed after the thickest point of the shear layer, which is the same point as maximum leapfrogging where one vortex is on top of each other.

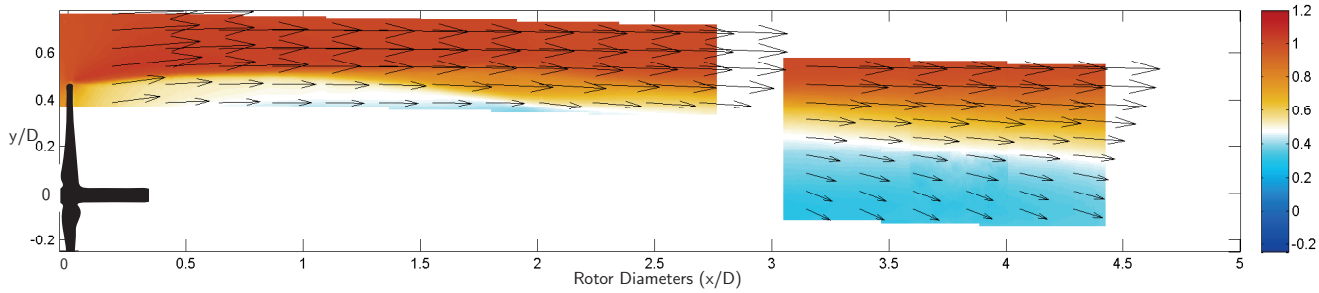

Figure 6.10: Unconditional averaged velocity magnitude field (normalized with respect to free-stream velocity) for TSR=4.8

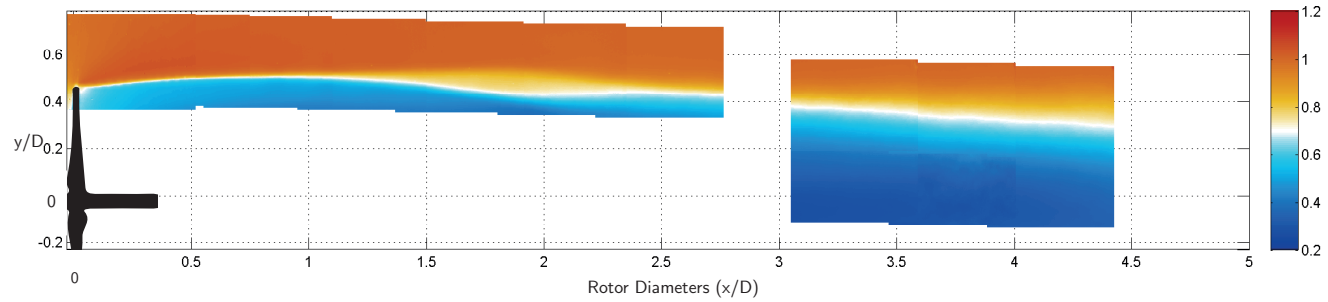

(a) Axial velocitiy field

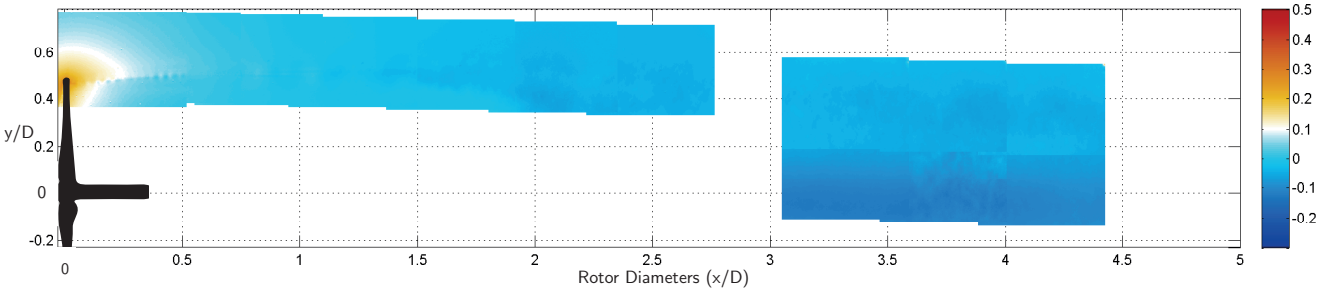

(b) Radial velocity field

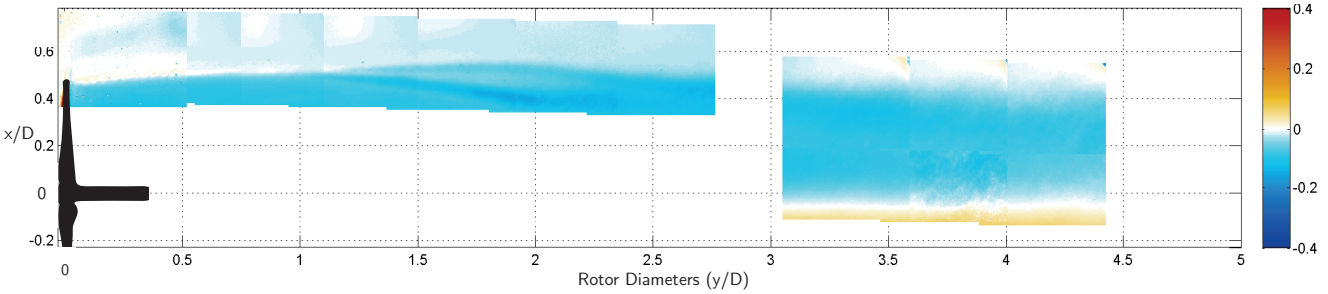

(c) Azimuthal velocity field

Figure 6.11: Unconditional averaged velocity field (normalized with respect to free-stream velocity)for TSR=4.8

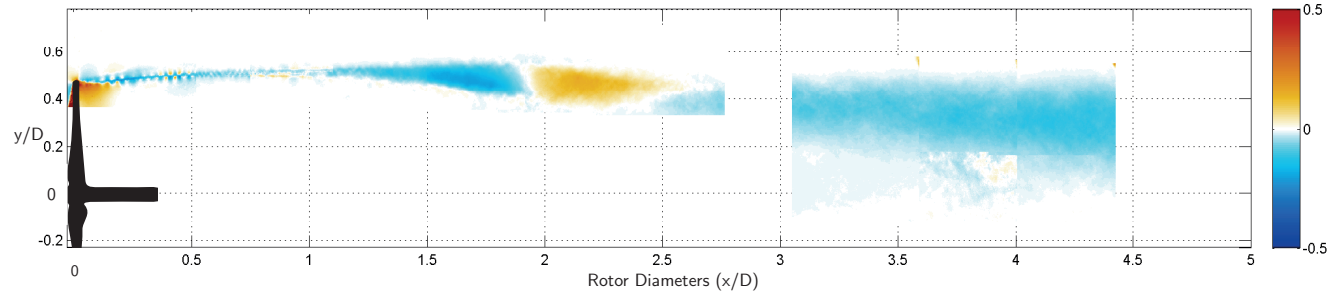

(a) Reynolds stresses in x-y direction

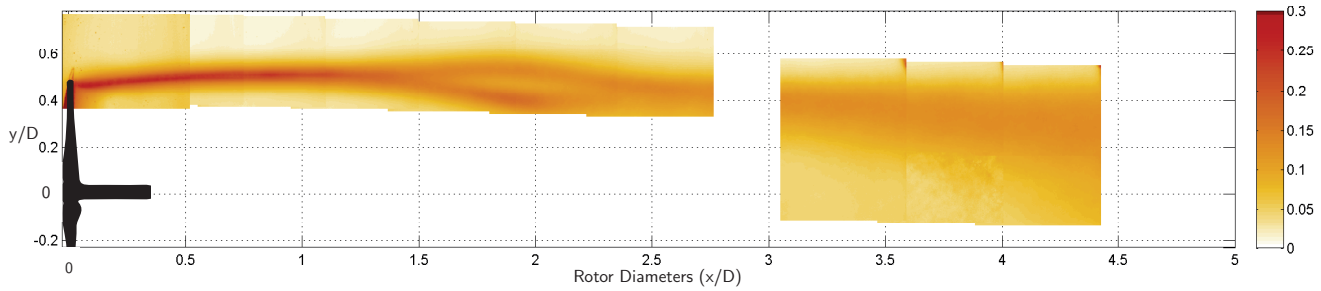

(b) Turbulence intensity

Figure 6.12: Unconditional averaged Reynolds stresses and turbulence intensity for TSR=4.8

6.3 Wake results analysis

This section uses the results from the previous section for a better understanding of the wind turbine wake.

6.3.1 Vortex field and Circulation

The vortex field in the z-direction is calculated for the phase locked velocity fields using equation 6.9

$$\langle \omega \rangle = \frac{\partial \langle u \rangle}{\partial x} - \frac{\partial \langle v \rangle}{\partial y} \tag{6.9}$$

Figure 6.13(a) and figure 6.13(b) show the phase locked vorticity fields calculated using equation 6.9. It can be seen from the results that the vorticity is strong and concentrated for the tip vortices close to the blade untill the leapfrogging motion. The result also shows that the region of vorticity expands as it travels downstream, which is due to viscosity. In the region beyond the leapfrogging the vorticity no longer remains concentrated, the vortex breaks down and diffuses quite rapidly. These vortex fields are not the values of vorticity which are not normalized.

The circulation is calculated by using equation 6.10. The procedure is illustrated in figure 6.14. Six closed contours, each around a vortex is used for calculating the circulation around each vortex. The plot of evolution of circulation and vorticity as a function of vortex age is shown in figure 6.15

$$\Gamma = \oint_c U.dl = \int_1 u.dx + \int_2 v.dy - \int_3 u.dx - \int_4 v.dy \tag{6.10}$$

From figure 6.15 it can be noticed that the alternating vortices have the same ranges of circulation for both tip speed ratios. This means that the vortex released from one blade is stronger than the other vortex released from the second blade. The same behaviour is observed for both the tip speed ratios. The difference in circulation from one blade to the other is estimated to be about 6%. This difference in circulation may have acted as the trigger for the instability in the wake which caused the leapfrogging of the tip vortices. There may be two specific reasons which can explain this behaviour

- The manufacturing or electroplating for each of the blades was different
- There was difference in the pitching of the blades with respect to each other

The first reason is the most likely explanation, since a neutral pitch block was used for assembling both the blades (as explained in the previous chapter).

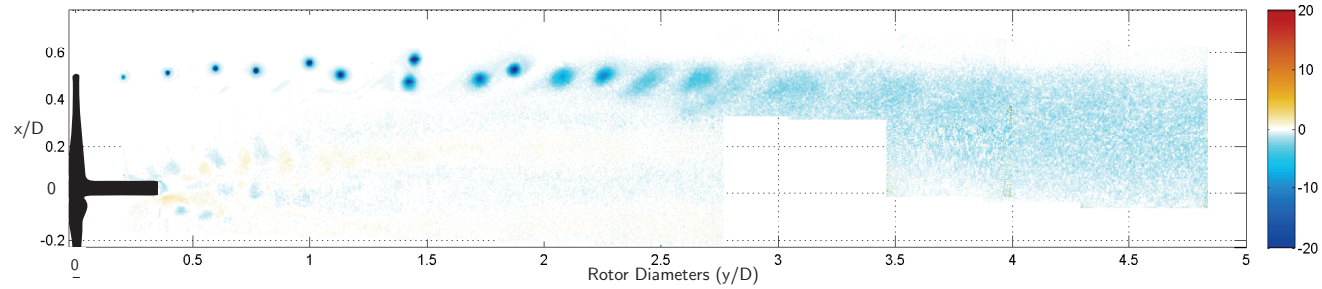

(a) Phase-locked average vorticity field for TSR=6

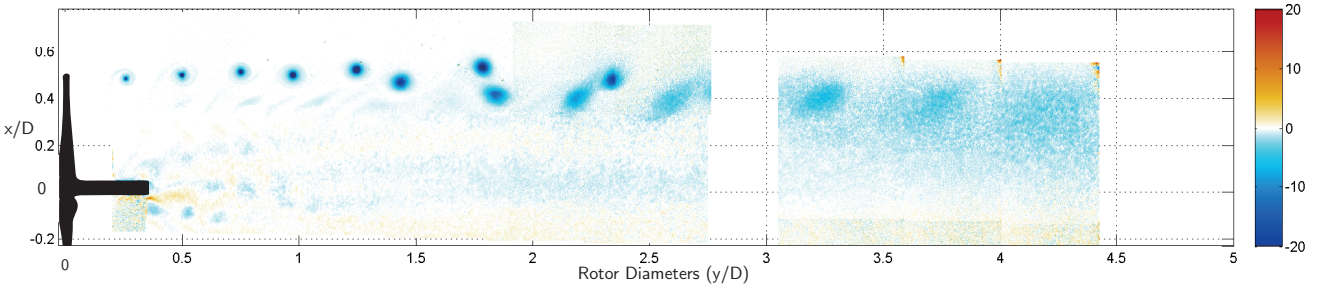

(b) Phase-locked average vorticity field for TSR=4.8

Figure 6.13: Phase-locked average vorticity field

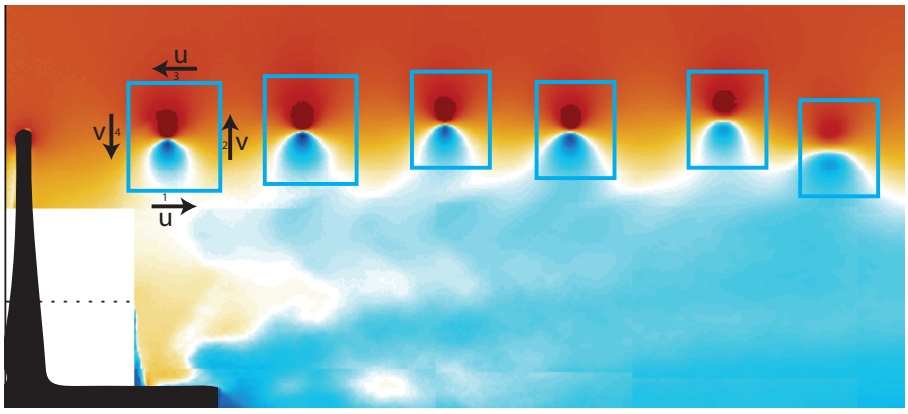

Figure 6.14: Calculation of circulation around a vortex

6.3.2 Vortex breakdown comparison

The vortex breakdown in the experiment is compared to the Lamb-Oseen vortex model in order to compare the rate of vortex breakdown. The Lamb-Oseen vortex model is modelled using the equation 6.11 for vorticity. The model isn't expected to match the data from the experiment since, this model fits well only for purely laminar flows (i.e.,

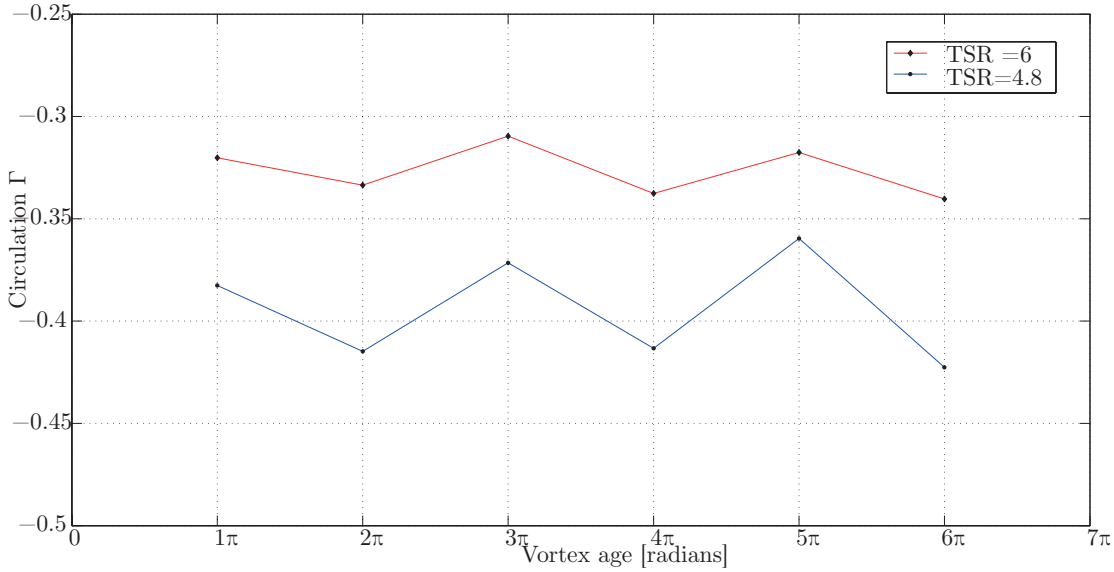

Figure 6.15: Evolution of circulation as a function of vortex age

where viscous diffusion of vorticity takes place only on a molecular level [8]) and the vortices in the experiment don't behave like laminar vortices.

$$\omega(r,t) = \frac{\Gamma}{4\pi\nu t}.e^{\left\{\frac{-r^2}{r_c^2(t)}\right\}} \tag{6.11}$$

where Γ is the circulation, ν is the kinematic viscosity and t is the time.

$$r_c^2(t) = 4\nu t \tag{6.12}$$

This model accounts for viscosity, which plays a critical role in breakdown of a vortex. The time is taken as the vortex age, which can be calculated using the frequency at which the rotor rotates. Figure 6.16 shows the comparison of the vorticity distribution across a vortex from the Lamb-Oseen model and the experiment. The result is plotted for the 2nd, 3rd and 4th vortex from the blade for the case of TSR=4.8. It can be clearly seen that the vorticity is much lower than what is predicted by the model. Another interesting aspect is that the width of the curve is larger for the experimental data than the curves predicted by the model. This is because the vortex diameter is higher than the prediction, meaning that the vortex is diffusing faster than expected. This affirms the fact that the vortex does not behave like a laminar vortex and some other mechanism like turbulence is causing the vortex to decay faster.

Figure 6.17 shows the plot for comparison of normalized vorticity for both the experiment and Lamb-Oseen model. The value of vorticity is taken 3mm away from the centre of the vortex, in order to avoid any errors which may have arisen due to the presence of lesser number of seeding particles at the centre of the vortex. The comparison shows that for TSR=6, the vorticity predicted by the model is about 15% higher than the vorticity obtained. It also shows an agreement with the trend obtained from the Lamb-Oseen model.

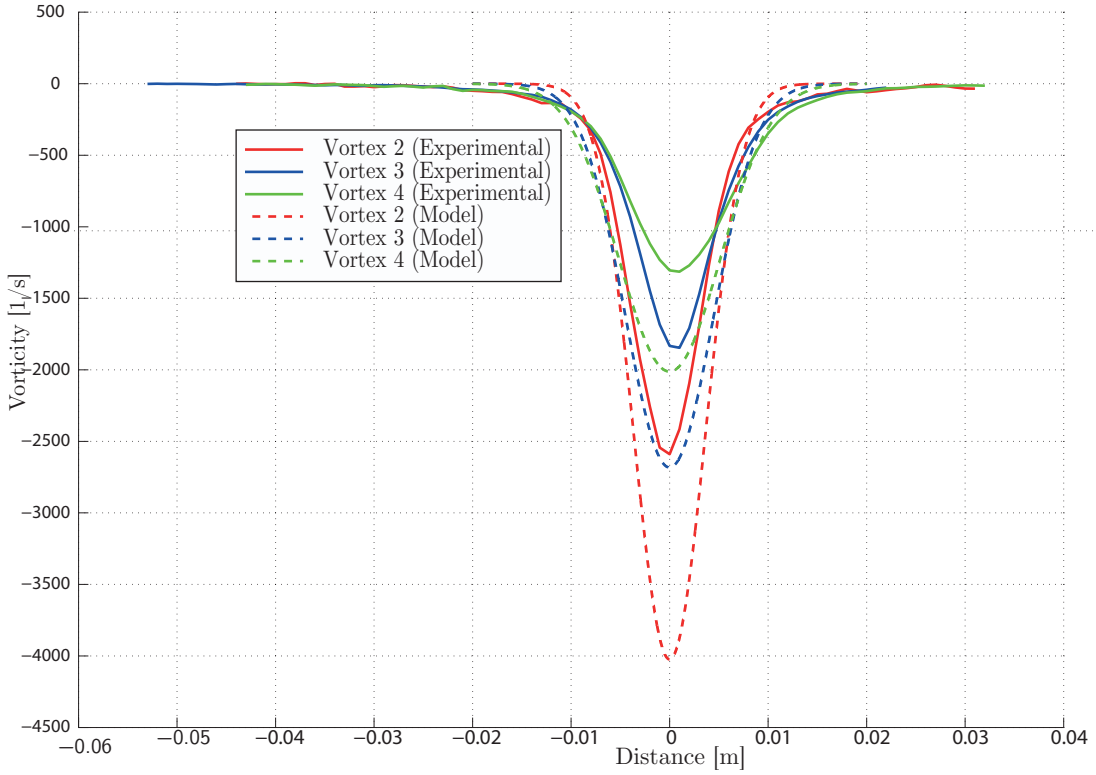

Figure 6.16: Comparison of vorticity from Lamb-Oseen model with experimental data for TSR=4.8

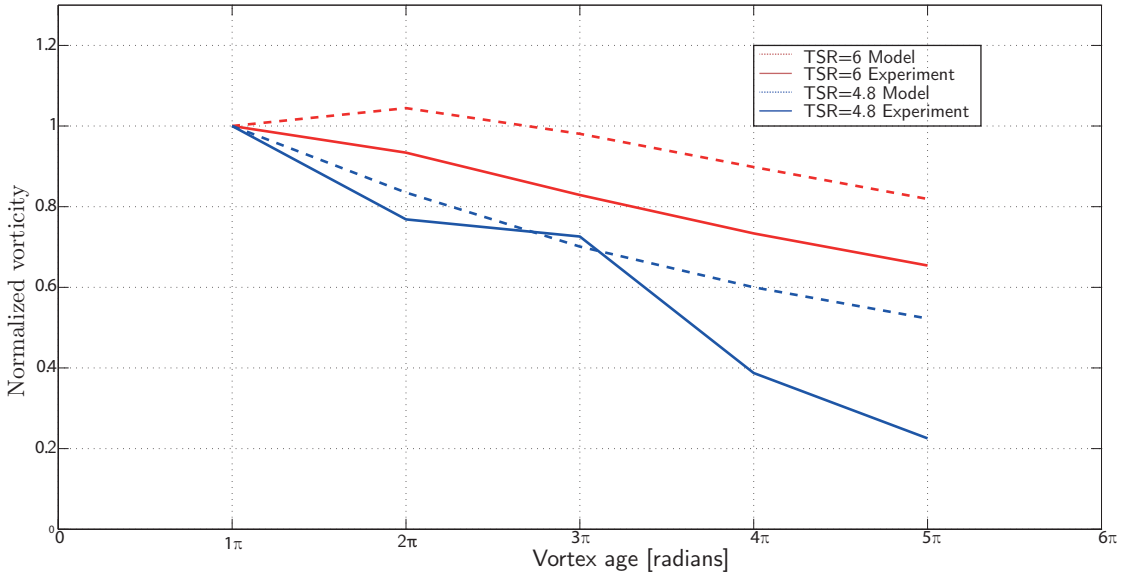

Figure 6.17: Comparison of normalized vorticity 3mm away from the vortex centre

6.3.3 Velocity distribution in the wake

Figures 6.18 and 6.19 show the streamwise velocity profiles, normalized phase-locked axial velocity fields for TSR=6 and TSR=4.8 respectively. The point on the plots represents the point at which maximum leapfrogging occurs which is about 1.4 diameters for TSR=6 and about 1.7 for TSR=4.8. A feature of this plot is that the axial velocity starts to increase gradually towards the value of free stream velocity nearly at the point of maximum leapfrogging. This indicates that after reaching a minimum at the maximum wake expansion, the axial velocity intakes a process of re-energising, starting from the outer regions where the turbulent mixing with the external flows happens. Figures 6.20 and 6.21 shows the spanwise velocity profiles, in a normalized phase-locked axial velocty field for the two TSRs. The red dashed lines represents the value of maximum wake expansion predicted by momentum theory (horizontal line) and the value of minimum wake velocity (vertical line). The theory predictions are in rather good agreement with the experimental results as far as the minimum wake velocity estimation is concerned, although the measured wake expansion seems lower than the theoretical one.

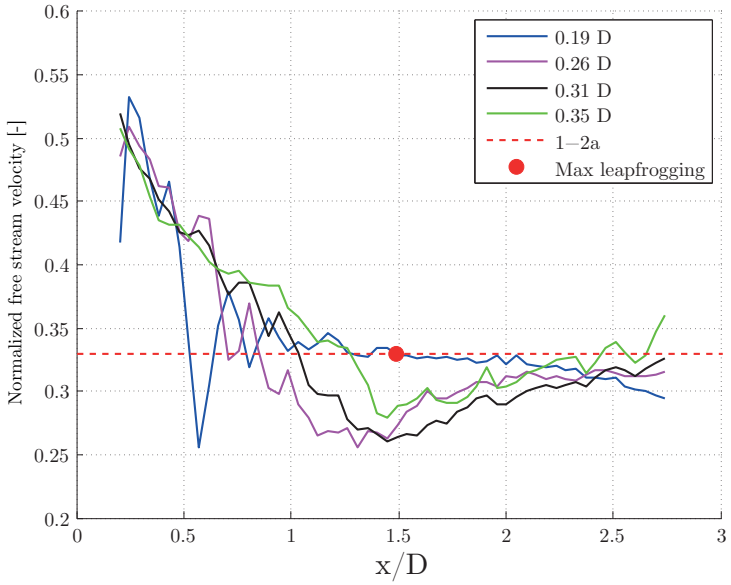

Figure 6.18: Streamwise vertical profiles of normalized phase locked axial velocity field for TSR=6

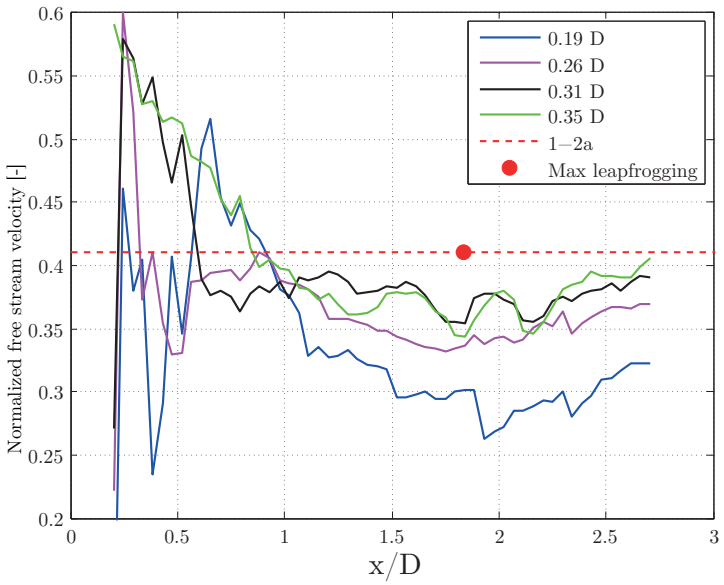

Figure 6.19: Streamwise vertical profiles of normalized phase locked axial velocity field for TSR=4.8

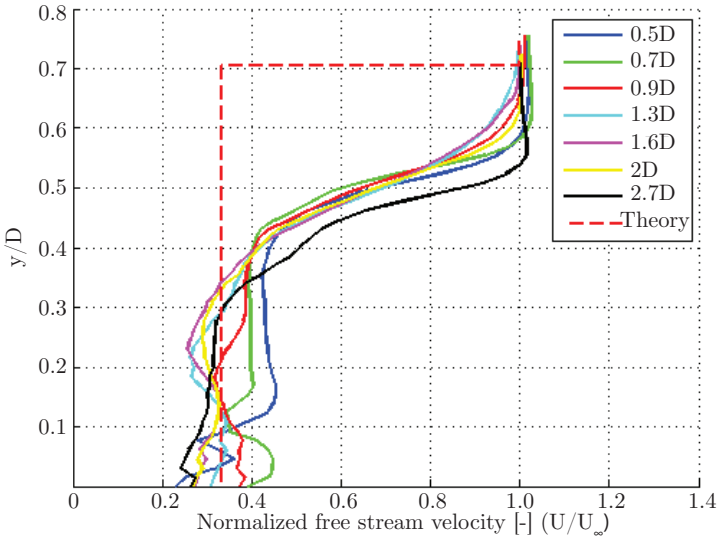

Figure 6.20: Spanwise profiles of normalized phase locked axial velocity field for TSR=6

6.3.4 Static pressure and enthalpy

The static pressure is obtained from the velocity field by using the method of Ragni et al. [34]. In regions of irrotational flow if the density is constant in the flow field, the Bernoulli pressure can be computed as only function of the flow velocity. But in rotational flow regions, the pressure gradient can still be evaluated from the Navier Stokes momentum

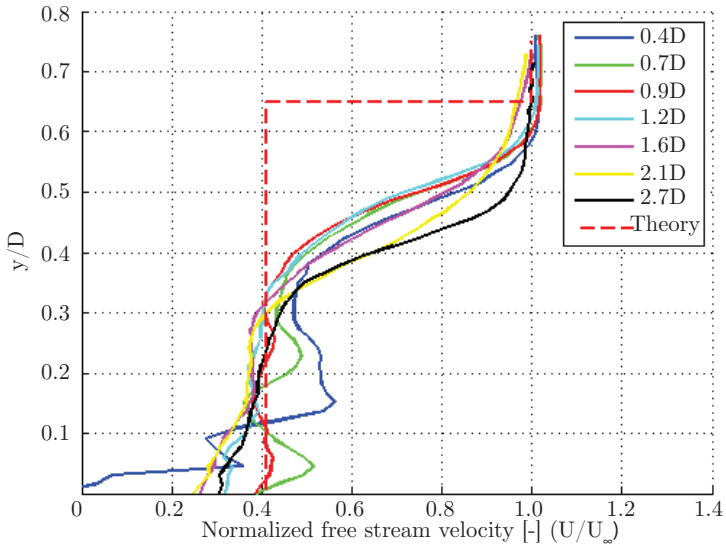

Figure 6.21: Spanwise profiles of normalized phase locked axial velocity field for TSR=4.8

equations, and in presence of viscosity as shown in equation 6.13.

$$\frac{1}{\rho}\frac{\partial p}{\partial x_i} = -\frac{\partial u_i}{\partial t} - u_j\frac{\partial u_i}{\partial x_j} + \frac{\mu}{\rho}\frac{\partial^2 u_i}{\partial x_j \partial x_j} \tag{6.13}$$

In the above equation ρ is the density of fluid in kg/m^3 and μ is the dynamic viscosity of air in m^2/s both of which are considered as constants. The time derivative of the velocity is obtained by differentiating the velocity fields at three different phases. The code written by Ragni et al. [34] is used in computing the pressure.

Dirichlet boundary condition (Bernoulli pressure) is applied to the upper boundary which is bound by free stream velocity while the Neumann boundary conditions is applied for the other three sides. Figures 6.22(a) and 6.22(b) shows the plots of average pressure fields of phase-locked velocity fields for TSR 6 and 4.8 respectively. The pressure field shown is shown in terms of static pressure co-efficient as shown in equation 6.14. The term p_∞ is the free-stream static pressure, U_∞ is the free-stream velocity.

The tip vortices clearly appear as low pressure zones, whereas in the rest of the wake the pressure is almost constant, apart from the area close to the rotor where a slight negative jump of pressure occurs due to both the wake of the nacelle and the power extraction of the blades.

$$C_p = \frac{p - p_\infty}{\frac{1}{2}\rho {U_\infty}^2} \tag{6.14}$$

Enthalpy in the wake can be taken as a measure for checking re-energization of the wake. Enthalpy ensures that apart from changes in velocity, changes in pressure in the wake are also accounted for. Enthalpy is given by the equation 6.15

$$H = T\nabla S + u \times \omega \tag{6.15}$$

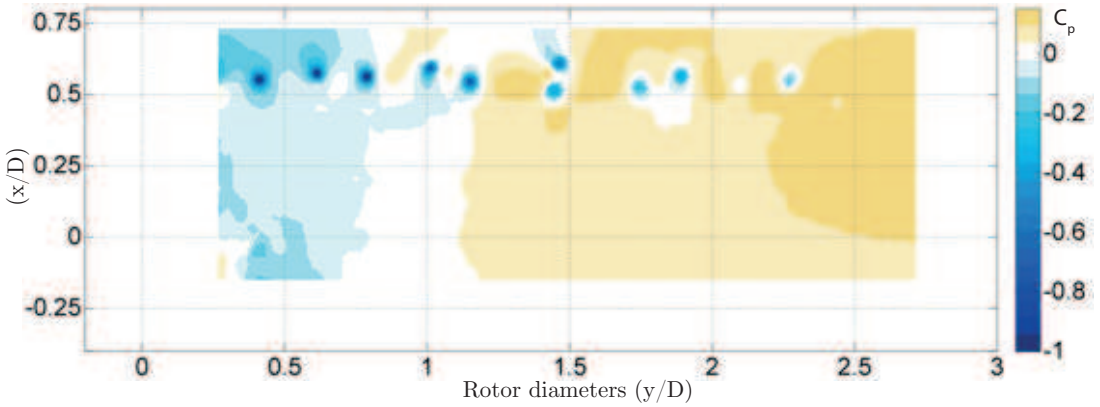

(a) TSR=6

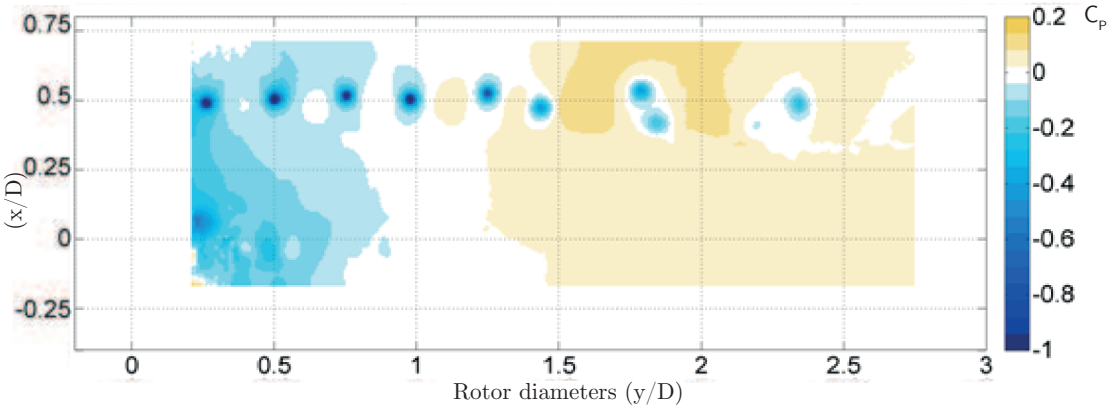

(b) TSR=4.8

Figure 6.22: Normalized phase-locked average pressure field

Where T is the temperature, S is the entropy, ω is the vorticity. Considering a homentropic flow, where S is uniform over the fluid, the equation can be re-written in a simplified form as equation 6.16

$$H = \frac{p}{\rho} + \frac{1}{2}\left(u^2 + v^2 + w^2\right) \tag{6.16}$$

Though the effect of temperature on enthalpy is ignored, it would be interesting to see the effect of temperature on change in enthalpy. Enthalpy can also be expressed in terms of change in enthalpy by considering the initial and final state and at a constant pressure the heat flow is equal to change in enthalpy.

$$\Delta H = q \tag{6.17}$$

The state where re-energization in the wake starts to occur, the enthalpy starts recovering meaning Δ H is negative, which can be made possible if heat is given off to the surroundings, which here is the wake.

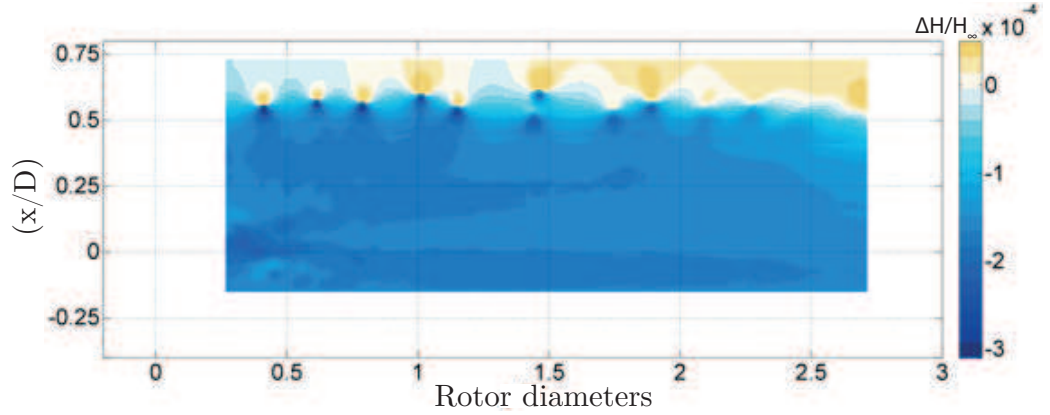

(a) TSR=6

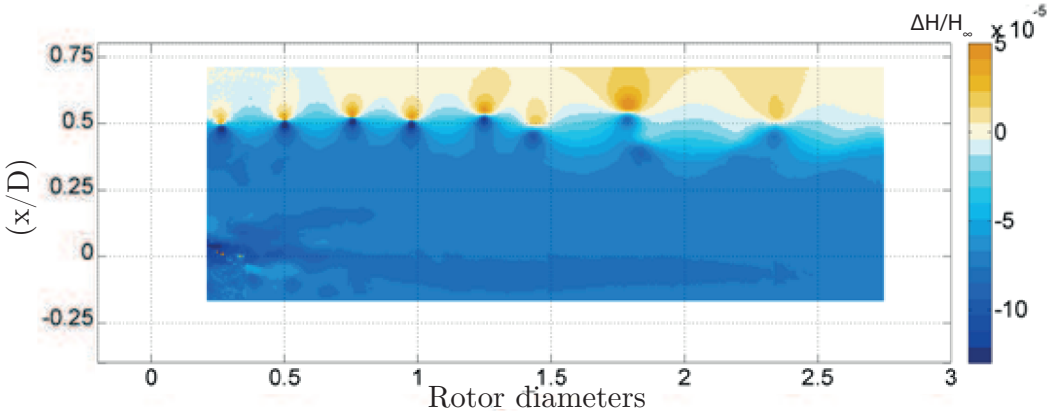

(b) TSR=4.8

Figure 6.23: Phase-locked stagnation enthalpy

Figure 6.23 shows the normalized enthalpy field in the wake for both the tip speed ratios. It can been seen that unlike the pressure field that a distinct differentiation of the wake and free-stream can be seen. The enthalpy shown in the field is normalized with respect to enthalpy of the incoming flow. The total enthalpy shows has a completely different behaviour, exhibiting a sudden jump across the shear layer location and a constant value inside the wake region where the wake expansion occurs. In this area in fact the decrease of flow kinetic energy is compensated by an increase of pressure, keeping the value of total enthalpy constant. After the wake expansion and the complete recovery of pressure, the value of H is not constant any longer due to the mixing with the outer flow characterised by a higher kinetic energy.

6.4 Loads experiment

The results from the blades experiment consisted of velocity fields for different sections of the blade starting from a location of about 20% to 102% span distance. The data were captured for TSR = 4.8. The velocity fields were captured from two different camera positions for each location, so as to capture the velocity fields on both the suction and pressure side of the airfoil and limit the shadow regions formed by the laser and the blade. The result obtained from the processing of each image is stitched together to form a single velocity field for the blade. A sample of the one of the stitched velocity field is shown in figure 6.24. The black region denotes the position of the airfoil, it is also noticeable that few data points close to the airfoil are lost due to the process of masking during post processing. The dashed red line indicates the point at which the pressure and suction side of the blade are stitched together.

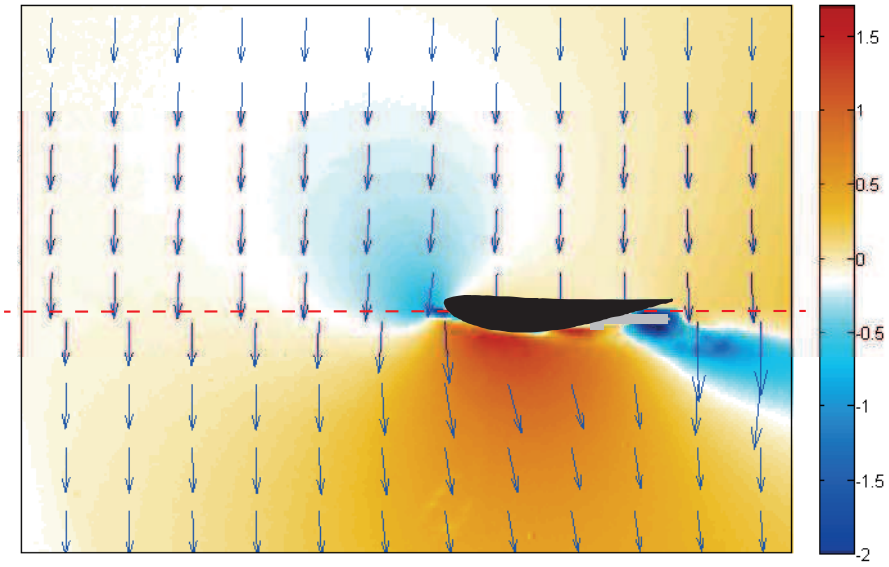

Figure 6.24: Stitched velocity field from the loads experiment

6.4.1 Circulation around the blades

The circulation is calculated around the blade using equation 6.10. The procedure is similar to the method which was used in calculation of circulation around a vortex in one of the previous section. The circulation for each location is calculated and compared with the circulation obtained from a BEM simulation for TSR = 4.8.

The value of circulation obtained is dependent on the dimension of the contour on which the integration takes place. Different window sizes whose boundaries do not cross-over the mask are iteratively tried until a near constant value of circulation is obtained. Figure 6.25 shows the variation of circulation for different window widths. It can be seen that the circulation starts increasing with an increase in the window width but tends to have a near constant value for higher window widths. The value of circulation is determined using a window size which falls in this region of near constant circulation.

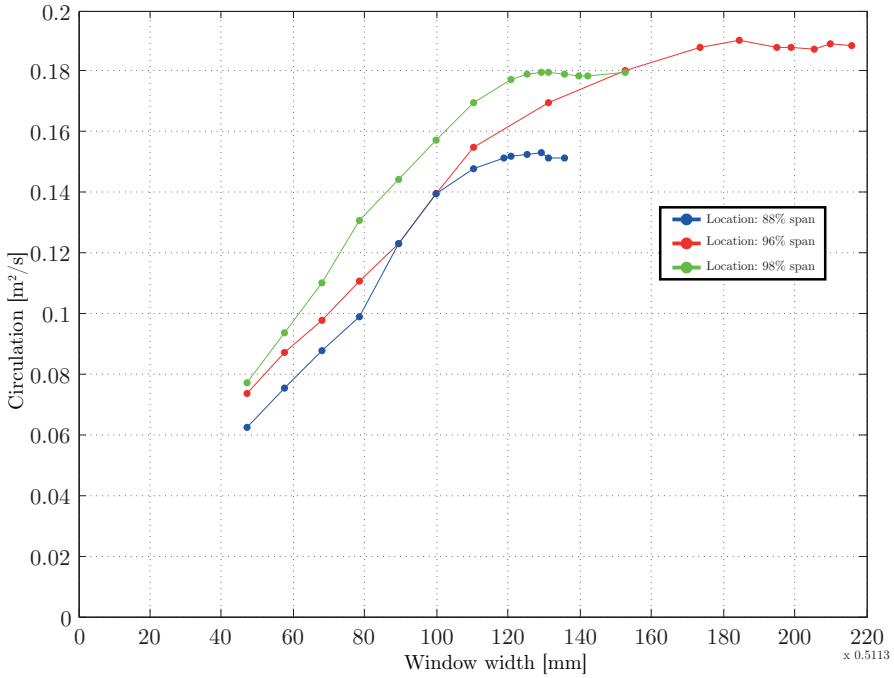

Figure 6.25: Circulation values for different window widths

Figure 6.26 shows the comparison between the circulations obtained from the experiment and the BEM theory for TSR = 4.8. It can been seen that the data obtained from the experiment is quite coarse (due to spatial resolution of PIV) and isn't upto the root section of the blade. This was because the twist angles at the root, which made capturing the velocities at these sections difficult. With the available data it can be seen that general trend of circulation along the span of the blade matches with the BEM model.

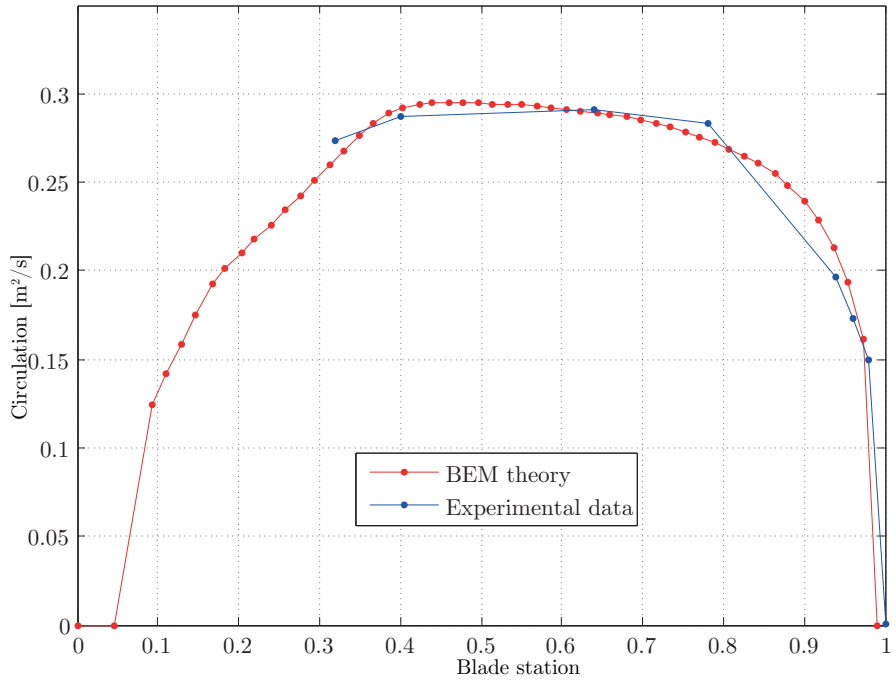

Figure 6.26: Comparison of circulation along the span for TSR=4.8 from the experiment and BEM theory

6.4.2 Loads on blade

This section contains partial results, showing the forces acting on two sections of the blade. The following section shows the preliminary results for blade positions of 100% span and 98%. Since the locations are quite close to the tip of the blade, the values obtained aren't expected to match values from the BEM simulation. The results shown are for 2-D sections but it is intended to calculate the loading along the blade span.

Forces exerted on the blade element, which is immersed in a fluid can be mainly attributed to the viscous shear stresses and surface pressure distribution over the airfoil. Consider a blade element as shown in figure 6.28, the instantaneous value of force which is exerted on the object by the fluid is given by equation 6.18. It can been seen that equation 6.18 has a time derivative term. Calculating this term requires an evaluation of the time dependent velocity components in the whole field. Since this is a difficult proposition experimentally, an approach used by Ragni et al., Oudheusden et al. [36] [35] [45] is applied in this context.

By this approach the control volume, which is the field of view is moved along with the same speed as that of the airfoil in that particular section. This implies that in the moving-frame formulation where the relative velocities are considered, according to the quasi-steady assumption, the time derivative is omitted, so no volume integration needs to be performed. Changing the frame of reference also leads to addition of Coriolis force to the equation. This is shown in equation 6.19, where the velocity terms are with respect to the moving frame of reference. Figure 6.27(a) shows the absolute velocity field with the airfoil in a fixed frame of reference. Figure 6.27(b) shows the relative velocity field

which shows a higher magnitude because of taking the rotation of turbine into account. A program is written taking into account each of the contributions separately. It is noticed that the major contributions to the forces comes from the pressure and the convective acceleration terms which have an order of magnitude of 0, while the Coriolis, Reynolds stresses and viscous terms have an order of magnitude of about -8, -4 and -4 respectively. Since their contribution is much smaller compared to the other terms, these terms are ignored for the preliminary analysis. Hence the equation is simplified further and shown in equation 6.20

$$\overrightarrow{F} = -\iiint_s \frac{\partial}{\partial t}\left(\rho \overrightarrow{V}\right) dV - \oiint_s \rho(\overrightarrow{V}.\overrightarrow{n}).\overrightarrow{V}\, ds + \oiint_s (-p\overrightarrow{n} + \overline{\overline{\tau}}'\vec{n} ds) \tag{6.18}$$

$$\overrightarrow{F} = -\oiint_s \rho(\overrightarrow{V}_R.\overrightarrow{n})\overrightarrow{V}_R ds + \oiint_s (-p\overrightarrow{n} + \Phi_{Corriolis} + \overline{\overline{\tau}}.\overrightarrow{n}) ds \tag{6.19}$$

$$\begin{bmatrix} F_x \\ F_y \end{bmatrix} = -\int_{abcd} \rho \begin{pmatrix} uu & uv \\ uv & vv \end{pmatrix} . \begin{pmatrix} n_x \\ n_y \end{pmatrix} ds - \int_{abcd} \begin{pmatrix} p & 0 \\ 0 & p \end{pmatrix} . n_x n_y \tag{6.20}$$

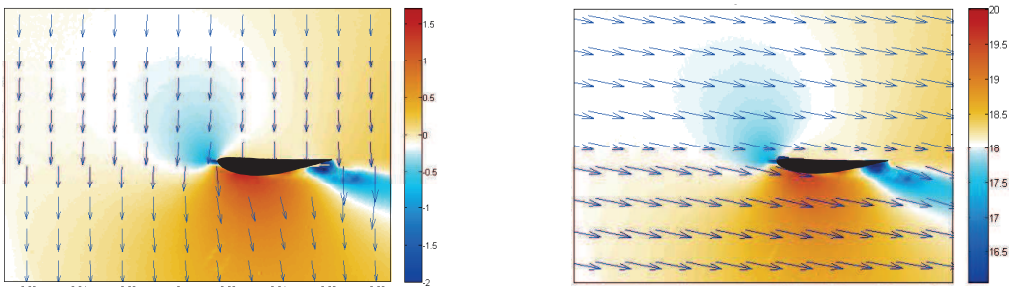

(a) Fixed frame of reference

(b) Moving frame

Figure 6.27: The frames of reference

For solving equation 6.20 the velocities can be directly obtained using PIV. The first term denotes the contribution to the forces by that of convective acceleration terms. The second term relates to the contribution of forces due to the pressure term. The pressure term alone needs to be computed. The following paragraphs explain the procedure which was used in computing the pressure term. The same algorithm with different boundary conditions are used for computing pressure in the wake which has been shown previously.

The first step involves calculation of pressure gradients from the momentum equation. The equation for calculating pressure gradients using relative velocities and considering the terms of Reynolds stresses and inertial forces as given by White[47] is shown in equation 6.21.

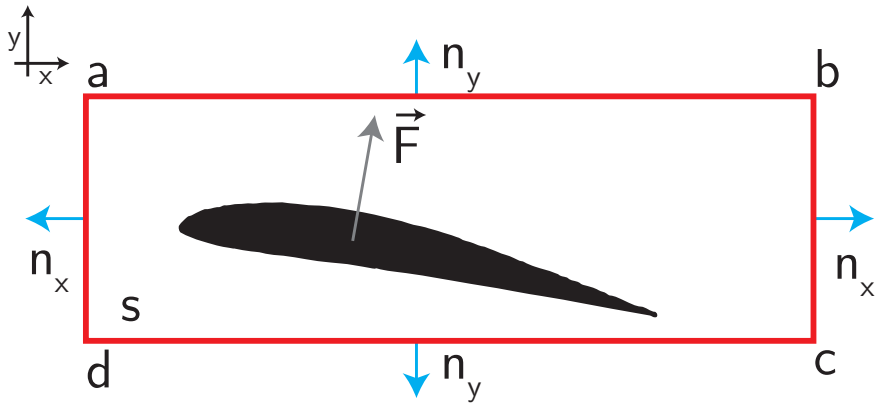

Figure 6.28: Contour for load calculation

Section [y/r]	Normal force [N/m]	Tangential force [N/m]
1.00	2.2068	1.2537
0.98	2.1208	1.4269

Table 6.1: Preliminary results of forces on blade sections

$$\begin{pmatrix} \frac{\partial p}{\partial x} \\ \frac{\partial p}{\partial y} \end{pmatrix} = -\rho \begin{pmatrix} u\frac{\partial u}{\partial x} + v\frac{\partial u}{\partial y} + w\frac{\partial u}{\partial z} \\ u\frac{\partial v}{\partial x} + v\frac{\partial v}{\partial y} + w\frac{\partial v}{\partial z} \end{pmatrix} - \rho \begin{pmatrix} \frac{\partial \overline{u'u'}}{\partial x} + \frac{\partial \overline{u'v'}}{\partial y} + \frac{\partial \overline{u'w'}}{\partial z} \\ \frac{\partial \overline{v'u'}}{\partial x} + \frac{\partial \overline{v'v'}}{\partial y} + \frac{\partial \overline{v'w'}}{\partial z} \end{pmatrix} \\ -2\rho \begin{pmatrix} \Omega w \\ 0 \end{pmatrix} + \mu \begin{pmatrix} \frac{\partial^2 u}{\partial x^2} + \frac{\partial^2 u}{\partial y^2} + \frac{\partial^2 u}{\partial z^2} \\ \frac{\partial^2 v}{\partial x^2} + \frac{\partial^2 v}{\partial y^2} + \frac{\partial^2 v}{\partial z^2} \end{pmatrix} \tag{6.21}$$

These pressure gradients calculated from the moving frame of reference. The pressure is calculated on every point on the field using equation 6.22. In the equation g(u,v) is the forcing function, which is derived from equation 6.21. Discretization of the Laplace operator is calculated using finite difference method. This along with the forcing function is shown in equation 6.23

$$\nabla^2 p \approx Dp = g(u,v) \Rightarrow p = D^{-1} g(u,v) \tag{6.22}$$

$$\left\{ \begin{array}{l} \left(\frac{p_{i+1,j} - 2p_{i,j} + p_{i-1,j}}{\Delta x^2} + \frac{p_{i,j+1} - 2p_{i,j} + p_{i,j-1}}{\Delta y^2} \right) = Dp \\ \frac{\left(\frac{\partial p}{\partial x}\right)_{i+1,j} - \left(\frac{\partial p}{\partial x}\right)_{i-1,j}}{2\Delta x} + \frac{\left(\frac{\partial p}{\partial x}\right)_{i,j+1} - \left(\frac{\partial p}{\partial y}\right)_{i,j-1}}{2\Delta y} = g(u,v)_{i,j} \end{array} \right\} \begin{array}{l} i = 1,2,3...n \\ j = 1.2,3...m \end{array} \tag{6.23}$$

In order to calculate the pressure in the field, a Dirichlet boundary condition is used in the upper, lower and left regions of the contour by considering the flow as irrotational. The pressure applied as Dirichlet boundary condition is calculated using Bernoulli theorem. For the region to the right side of the contour, a Neumann boundary condition calculated (pressure gradient) from equation 6.21.

The results calculated for two sections using equation 6.20 is shown in terms of normal and tangential forces in table 6.1. The major contribution for these terms comes from the convective and pressure terms.

The results obtained can be refined even further. Two specific problems which are yet to be addressed completely, relates to the mask and spurious velocity vectors removed by DaVis. Since the calculation of pressure gradients requires velocity gradients, the presence of spurious vectors ultimately leads to an erroneous pressure field. The mask of airfoil is bigger than the actual size of the airfoil owing to reflections and twist of the blade. For a few sections along the blade this mask stretches upto a boundary leading to errors in calculation of loads.

Chapter 7

Uncertainties

The results from the previous chapter are affected by experimental errors, which are both of systematical and stochastic nature. Quantification of these errors on the current experiment is quite difficult because of the complexity in the setup. But the sources of these errors can be identified and a rough estimation of the uncertainties can be made. This chapter contains a discussion about the possible sources of experimental error and a quantification of the uncertainties in the results. These sources are classified into three types namely

- Flow uncertainties
- Model and setup uncertainties
- PIV uncertainties

7.1 Flow uncertainties

The flow in a wind tunnel can be affected by a number of factors like model blockage, flow temperature, tunnel shear layer and turbulence in the flow. The wind turbine rotor occupies about 4% area of the area of the wind tunnel nozzle. Hence the blockage effect of the model on the flow can be ignored, the effect being negligible.

The experiments on the wind turbine were started every morning and continued into late evening. The changing ambient temperature in the wind tunnel over the period the day affects the flow properties. Also on a day-to-day basis the change in temperature has an influence on the flow inside the wind tunnel. In order to minimize the effects from change in temperature, the heater in the wind tunnel was used continuously throughout the experiment. The temperature was noted for each of the reading and an average variation for a single set of readings (over a period of 3-4 days) was found to be between 18^0C to

23^0C. For quantifying this variation, assuming air to be an ideal fluid and it satisfying equation 7.1, the ideal gas law

$$p_\infty = \rho RT \tag{7.1}$$

In the ideal gas equation p_∞ represents the static gas pressure in Pascal, ρ is the gas density in kg/m^3, R being the specific gas constant (R = 287.1 J/(Kg.K)). T is the temperature in Kelvin scale. At the average of the upper and lower limit of temperature (20.5^0C) the density of air is 1.202 kg/m^3. Using this equation the density at the upper limit, lower limit and at the average temperature can be calculated as follows

$$\rho = \frac{p_\infty}{RT} \tag{7.2}$$

$$\rho_{18} = \frac{101325}{287.1 * (273 + 18)} = 1.213 kg/m^3 \tag{7.3}$$

$$\rho_{23} = \frac{101325}{287.1 * (273 + 23)} = 1.192 kg/m^3 \tag{7.4}$$

$$\rho_{avg} = \frac{101325}{287.1 * (273 + 20)} = 1.204 kg/m^3 \tag{7.5}$$

The upper limit and lower limit of velocity can be found out using the conservation of mass relation.

$$\rho_{avg} u_{avg} = 1.204 * 5.7 = 6.826 = \rho_{upper} u_{upper} = \rho_{lower} u_{lower} \tag{7.6}$$

Using the values of density for upper and lower limit from equations 7.3 and 7.4, the limits for free stream velocity for the case of TSR of 6 varies from 5.657 m/s to 5.726 m/s. The variation is compared with respect to a set value of 5.7 m/s

For every meter downstream travelled, the diameter of the jet is reduced by 16.7 cm. At 6m from the nozzle only a portion of the jet having a diameter equal to 2m can be used. The experiments were performed within a region, which extends 3m streamwise (from the nozzle location) and 0.5m radially (from the jet centreline). This is sufficiently within the region where the jet shear layer and the flow oscillations are negligible. In this region the turbulence intensity is lower than 0.5% and the flow inhomogeneity is lower than 1%.

7.2 Model and setup uncertainties

The sources of error associated with the model and setup are the timer circuit, frequency oscillation of the model, blade manufacturing, blade pitching, the traversing system, alignment of calibration plate.

The timer circuit which is controls the phase locking mechanism in the experiment is quite accurate. The error level in the experiment due to the timer circuit is in the range

of a few pico seconds. Since this is relatively smaller when compared in the time scale of the experiment, the uncertainty in the experiment due to this can be ignored.

The rotor's rotational frequency was maintained by a motor and a speed controller. Though the speed controller was able to keep a tab on the rotor frequency, there was always an oscillation of frequency. For instance, in the case of TSR 6 the frequency kept varying between 9.63 Hz to 9.7 Hz for a set frequency of 9.67 Hz. The variation in tip speed ratio for the variation in this frequency can be calculated as follows

$$\lambda = \frac{\omega r}{U_\infty} = \frac{2\pi f r}{U_\infty} \tag{7.7}$$

$$\lambda_{lower} = \frac{2\pi * 9.63 * 0.3}{3.8} = \frac{18.15}{3.8} = 4.776 \tag{7.8}$$

$$\lambda_{upper} = \frac{2\pi * 9.7 * 0.3}{3.8} = \frac{18.28}{3.8} = 4.811 \tag{7.9}$$

This shows a variation of -0.0240 and +0.0110 with respect to the set tip speed ratio of 4.8. By plugging this into the equation from curve-fit of coefficient of thrust vs tip speed ratio, the variation in C_T can be obtained.

$$C_T = -0.0168\lambda^2 + 0.2341\lambda + 0.0841 \tag{7.10}$$

From curvefit the lower limit of coefficient of thrust can be obtained as 0.8190, while the upper limit is calculated at 0.8215.

The blades were manufactured on CNC machine with the design of the blade given as input in form of a CAD drawing and hand finished in the end. These blades were then electroplated with black paint in order to reduce the reflections during the experiment. CNC machines are quite accurate but the finishing process may have introduced some imperfections on each blade. Similarly the electroplating process also may have contributed to the imperfections on the blade. They may have caused the leap frogging of the vortices as seen from the results. For instance, if there are differences in the length of two blades, then the point of release of the tip vortex is different for each blade. This changes the behaviour of the vortices released.

The traversing system held the PIV setup in place for scanning the wake of the wind turbine. This system was aligned in place with respect to the wind turbine and the wind tunnel using a co-ordinate laser alignment kit. The laser emitted from the kit had a laser thickness of about 3 mm, which was used as a guide line in adjusting the position of the traversing system. Therefore there is an inherent unpredictability in the position of the traversing system of about ±3mm. This misalignment was reflected in the stitched images, but was corrected by incorporating appropriate shifts to the individual images.

The misalignment of the calibration plate can occur in two different ways namely

1. Measuring plane and calibration plate misalignment
2. Misalignment between the calibration plate and flow

The measuring plane was illuminated by the laser sheet, the calibration plate's position was manually adjusted using a screw jack to the illuminated plane. Similarly the plate was aligned manually with respect to the flow using the tripod of the screw jack as a reference. If these error existed, it was corrected by the self-calibration method on DaVis 8.1.3.

7.3 PIV uncertainties

Random components of error are mainly due to cross-correlation uncertainty and results from flow variability and turbulence. As a result of statistical convergence, the effect of these random uncertainty components decreases with the square root of the number of samples. Hence larger the number of samples, the smaller is the uncertainty. The statistical convergence for the sample size of 400 for phase locked and 720 for uncorrelated samples is shown in chapter 5.

Seeding plays a critical role in determining the quality of the results. Consider an example of a vortex flow, the number of particles inside the vortex core is much lesser than outside the flow. This can be attributed to the centrifugal force inside a vortex which pushes the outside the core. Hence the data obtained inside a vortex is not always accurate and is always subject to an uncertainty.

PIV post processing parameters like interrogation window size, overlap, number of passes, etc have an impact on the final result obtained from the cross-correlation analysis. In addition to the uncertainties introduced by cross-correlation, pre and post-processing (difference, smoothing, interpolation, filtering, etc) also introduce uncertainties into the results.

Three unique calibrations were used during the experiment. A single calibration is used for the region upto 2 diameters for both tip speed ratios of 6 and 4.8. Two separate calibrations are used for the rest of the region for the two tip speed ratios. The calibration was performed by fitting a camera pinhole model using multiple. Using the parameters obtained from these calibrations a displacement uncertainty for each calibration is calculated. This is tabulated and shown in table 7.1

Calibration	**Pixel fit** [px]	**Camera scale** [px/mm]	**Displacement** [mm]
TSR 6 and 4.6 upto 2 diameters	0.9155	13.8647	0.066
TSR 6 beyond 2 diameters	0.94155	13.8647	0.068
TSR 4.8 beyond 2 diameters	0.64427	13.717	0.047

Table 7.1: Uncertainties from image calibration

Chapter 8

Conclusions and recommendations

The wake of a horizontal axis turbine is captured using a Stereo Particle Image Velocimetry setup (SPIV) with measurements upto 5 diameters for two different tip speed ratios. Phase-locked as well unconditioned samples are captured during the experiment.

This chapter summarises the key observations and also provides recommendations for future work.

8.1 Conclusions

- Instability in the wake has an effect on the location of re-energization of the wake. It is noticed that re-energization starts at about 1.5D downstream for TSR = 6 and 1.8D downstream for TSR = 4.8 both of which coincides with the point of maximum leapfrogging.
- Leapfrogging's has an effect on development of wake turbulence. It can be seen from the turbulence intensity fields that its magnitude which is concentrated within the tip vortices in the near wake, scatters in the far wake after the event of leapfrogging.
- The location of the instability is dependent on the tip-speed ratio. For TSR = 6 a sudden enlargement of the shear layer for this tip speed ratio on account of leapfrogging of tip vortices. The expansion of the shear layer starts at about 1.5 rotor diameter downstream and reaches a maximum at about 1.7 diameters. While for TSR = 4.8, the expansion of the shear layer starts at about 1 rotor diameter downstream and reaches a maximum at about 1.4 diameters.
- The circulation obtained from consecutive vortices shows a fluctuations in values of upto 6% indicating that one blade releases a stronger vortex than the other, which ultimately causes the leapfrogging to occur.
- Leapfrogging of tip vortices are most probably due to manufacturing differences between the two blades, which ultimately may be the trigger of the leapfrogging.

- Comparison of circulation from BEM model and experiment show a good agreement in terms of behaviour, though the data from the experiment is quite coarse and incomplete in terms of blade span covered.

8.2 Recommendations

The experiment performed on the wind turbine wake was done upto 4.5 to 5 diameters downstream. In order to have a better understanding of re-energization in the far wake, it favoured to capture the data not only in the downwind direction but also in the inboard direction. The study conducted shows that the tip vortices from the wind turbine undergo leapfrogging and breakdown rapidly close to 2 diameters downstream. The exact cause of this is speculated to be a manufacturing difference between the two blades. To study the effect of leapfrogging on the power output of the turbine downstream in the wake would also be an interesting topic. The loads of the blade has been partially computed, further analysis of these results can be done and compared to the results from BEM theory simulation.

References

[1] *DaVis 7.2 manual*.

[2] RE Altenhofen. Manual of photogrammetry. *American Society of Photogrammetry, Washington DC*, 1952.

[3] John David Anderson. *Fundamentals of aerodynamics*, volume 2. McGraw-Hill New York, 2001.

[4] Rebecca Barthelmie, W Schlez, J Phillips, A Neubert Garrad Hassan, K Hansen, K Rados, O Rathmann, and JG Schepers. Wp8: Flow deliverable d8. 2 comparing existing wake models with cfd offshore.

[5] Rebecca Jane Barthelmie, SC Pryor, Sten Tronæs Frandsen, Kurt Schaldemose Hansen, JG Schepers, K Rados, W Schlez, A Neubert, LE Jensen, and S Neckelmann. Quantifying the impact of wind turbine wakes on power output at offshore wind farms. *Journal of Atmospheric and Oceanic Technology*, 27(8):1302–1317, 2010.

[6] Rebecca Jane Barthelmie, Ole Rathmann, Sten Tronæs Frandsen, KS Hansen, E Politis, J Prospathopoulos, K Rados, D Cabezon, W Schlez, J Phillips, et al. Modelling and measurements of wakes in large wind farms. In *Journal of Physics: Conference Series*, volume 75, page 012049. IOP Publishing, 2007.

[7] RJ Barthelmie, ST Frandsen, K Hansen, JG Schepers, K Rados, W Schlez, A Neubert, LE Jensen, and S Neckelmann. Modelling the impact of wakes on power output at nysted and horns rev. In *European Wind Energy Conference*, 2009.

[8] Mahendra J Bhagwat and J Gordon Leishman. Generalized viscous vortex model for application to free-vortex wake and aeroacoustic calculations. In *ANNUAL FORUM PROCEEDINGS-AMERICAN HELICOPTER SOCIETY*, volume 58, pages 2042–2057. AMERICAN HELICOPTER SOCIETY, INC, 2002.

[9] FK Browand and J Laufer. The role of large scale structures in the initial development of circular jets. In *Turbulence in Liquids*, volume 1, pages 333–342, 1977.

[10] Tony Burton, Nick Jenkins, David Sharpe, and Ervin Bossanyi. *Wind energy handbook*. Wiley, 2011.

[11] Raul Bayoan Cal, Nicholas Hamilton, Hyung-Suk Kang, and Charles Meneveau. Statistical analysis of kinetic energy entrainment in a model wind turbine array boundary layer. *Bulletin of the American Physical Society*, 57, 2012.

[12] Georges-Henri Cottet and Petros D Koumoutsakos. *Vortex methods: theory and practice*. Cambridge university press, 2000.

[13] A Crespo, J Hernandez, and S Frandsen. Survey of modelling methods for wind turbine wakes and wind farms. *Wind energy*, 2(1):1–24, 1999.

[14] JÅ Dahlberg and SE Thor. Power performance and wake effects in the closely spaced lillgrund offshore wind farm. In *European Offshore Conference*, 2009.

[15] Ivan Dobrev, Bassem Maalouf, Niels Troldborg, and Fawaz Massouh. Investigation of the wind turbine vortex structure. In *14th international symposium on applications of laser techniques to fluid mechanics, Lisbon, Portugal*, pages 07–10, 2008.

[16] PR Ebert and DH Wood. The near wake of a model horizontal-axis wind turbine: Part 3: properties of the tip and hub vortices. *Renewable Energy*, 22(4):461–472, 2001.

[17] Scarano. F. Course: Flow measurement techniques (ae 4180). 2012. University Lecture notes.

[18] M Felli, R Camussi, and F Di Felice. Mechanisms of evolution of the propeller wake in the transition and far fields. *Journal of Fluid Mechanics*, 682(1):5–53, 2011.

[19] C.J. Simao Ferreira. Course: Ae4w12 rotor aerodynamics. 2012. University Lecture notes.

[20] Wind Energy Foundation. Faqs, 2012.

[21] H Glauert. Airplane propellers, aerodynamic theory, edited by wf durand, 1963.

[22] Nicholas Hamilton, Hyung Suk Kang, Charles Meneveau, and Raúl Bayoán Cal. Statistical analysis of kinetic energy entrainment in a model wind turbine array boundary layer. *Journal of Renewable and Sustainable Energy*, 4(6):063105–063105, 2012.

[23] Douglas P Hart. Piv error correction. *Experiments in fluids*, 29(1):13–22, 2000.

[24] Jørgen Højstrup. Spectral coherence in wind turbine wakes. *Journal of Wind Engineering and Industrial Aerodynamics*, 80(1):137–146, 1999.

[25] Stefan Ivanell, Robert Mikkelsen, Jens N Sørensen, and Dan Henningson. Stability analysis of the tip vortices of a wind turbine. *Wind Energy*, 13(8):705–715, 2010.

[26] Stefan Ivanell, Jens N Sørensen, and Dan Henningson. *Numerical computations of wind turbine wakes*. Springer, 2007.

[27] M Kloosterman. Development of the near wake behind a horizontal axis wind turbine. *Masters of science*, 2009.

[28] Gunner Chr Larsen. *A simple wake calculation procedure*. 1988.

[29] LaVision. Product manual. 2005. DaVis 7.4.

[30] Ajay K Prasad and Kirk Jensen. Scheimpflug stereocamera for particle image velocimetry in liquid flows. *Applied optics*, 34(30):7092–7099, 1995.

[31] AK Prasad and RJ Adrian. Stereoscopic particle image velocimetry applied to liquid flows. *Experiments in Fluids*, 15(1):49–60, 1993.

[32] Arun K Prasad. Stereoscopic particle image velocimetry. *Experiments in fluids*, 29(2):103–116, 2000.

[33] Markus Raffel, Christian E Willert, Steven T Wereley, and Jürgen Kompenhans. *Particle image velocimetry: a practical guide*. Springer, 2007.

[34] D Ragni, BW Van Oudheusden, and F Scarano. Non-intrusive aerodynamic loads analysis of an aircraft propeller blade. *Experiments in fluids*, 51(2):361–371, 2011.

[35] D Ragni, BW Van Oudheusden, and F Scarano. 3d pressure imaging of an aircraft propeller blade-tip flow by phase-locked stereoscopic piv. *Experiments in fluids*, 52(2):463–477, 2012.

[36] Daniele Ragni. *PIV-based load determination in aircraft propellers*. 2012.

[37] Douwe J Renkema. *Validation of wind turbine wake models*. PhD thesis, Master Thesis in Delft University of Technology, 2007.

[38] WC Reynolds and AKMF Hussain. The mechanics of an organized wave in turbulent shear flow. part 3. theoretical models and comparisons with experiments. *Journal of Fluid Mechanics*, 54(02):263–288, 1972.

[39] B Sanderse. Aerodynamics of wind turbine wakes. *Energy Research Center of the Netherlands (ECN), ECN-E–09-016, Petten, The Netherlands, Tech. Rep*, 2009.

[40] Jan Gerhard SCHEPERS and Ingenieur Luchtvaart en Ruimtevaarttechniek. Engineering models in wind energy aerodynamics.

[41] Michael S Selig, Christopher Alan Lyon, P Giguere, C Ninham, and JJ Guglielmo. *Summary of low-speed airfoil data*, volume 1. SoarTech Publications Virginia Beach, VA, 1995.

[42] David A Simms, S Schreck, M Hand, and LJ Fingersh. *NREL unsteady aerodynamics experiment in the NASA-Ames wind tunnel: A comparison of predictions to measurements*. National Renewable Energy Laboratory Colorado, USA, 2001.

[43] Jens Nørkær Sørensen and Carsten Weber Kock. A model for unsteady rotor aerodynamics. *Journal of wind engineering and industrial aerodynamics*, 58(3):259–275, 1995.

[44] P Sorensen and T Nielsen. Recalibrating wind turbine wake model parameters-validating the wake model performance for large offshore wind farms. In *European Wind Energy Conference and Exhibition*, pages 145–149, 2006.

[45] Bas W van Oudheusden, Fulvio Scarano, Eric WM Roosenboom, Eric WF Casimiri, and Louis J Souverein. Evaluation of integral forces and pressure fields from planar velocimetry data for incompressible and compressible flows. *Experiments in Fluids*, 43(2-3):153–162, 2007.

[46] LJ Vermeer, Jens Nørkær Sørensen, and A Crespo. Wind turbine wake aerodynamics. *Progress in aerospace sciences*, 39(6):467–510, 2003.

[47] Frank M White. *Viscous Fluid Flow 3e*. Tata McGraw-Hill Education, 1974.

[48] CE Willert and M Gharib. Digital particle image velocimetry. *Experiments in fluids*, 10(4):181–193, 1991.

[49] CD Winant and FK Browand. Vortex pairing- the mechanism of turbulent mixing-layer growth at moderate reynolds number. *Journal of Fluid Mechanics*, 63(2):237–255, 1974.

Appendix A

Force balance experiment

A.1 Readings from the experiment

The following section tabulates the readings from obtained from the force balance experiment. Table A.1 shows the readings from the experiment with the blades attached to the wind turbine. The second step involved dismantling of the blade and recording the force applied by the tower for different wind speeds. The readings for this is shown in table A.2. The final readings of the forces on the blade is calculated by subtracting the forces for different wind speeds are shown in table A.3

A.2 Force balance

The wind turbine is fastened to the balance on the aluminium model plate by means of bolts. The balance consists of six load cells which makes it capable of measure the forces and moments in x, y and z directions. The balance uses four mechanical end stops to limit the maximum displacement of the metric frame. These stops allow a maximum load of 130% of the nominal load range.

TSR [-]	Wind speed [m/s]	Force [N]
2.3	4.1	2.288
3.1	4.1	2.599
3.6	3.6	2.203
4.3	4.1	2.984
4.8	3.6	2.451
5	3.6	2.446
5.3	5	4.66
5.8	4.1	3.158
5.9	3.6	2.514
6.4	5	4.797
7.1	3.6	2.568
8.1	4.1	3.265
8.3	4.1	3.285

Table A.1: Readings for the force balance experiment with the blades on the wind turbines

Wind speed [m/s]	Tower drag [N]
3.6	0.61
4.1	0.777
5	1.2

Table A.2: Readings for the force balance experiment without the blades on the wind turbines

TSR	Force [N]	C_T
2.3	1.511	0.51
3.1	1.822	0.61
3.6	1.593	0.70
4.3	2.207	0.74
4.8	1.841	0.80
5	1.836	0.80
5.3	3.46	0.78
5.8	2.381	0.80
5.9	1.904	0.83
6.4	3.597	0.81
7.1	1.958	0.85
8.1	2.488	0.84
8.3	2.508	0.84

Table A.3: Readings after taking tower drag into account